# NUMERICAL ANALYSIS OF ARC PLASMA BEHAVIOR IN A PLASMA SPRAY TORCH

**Renzhong Huang**

March 2012

**Doctoral thesis**

# NUMERICAL ANALYSIS OF ARC PLASMA BEHAVIOR IN A PLASMA SPRAY TORCH

A Dissertation submitted to the

Graduate School of Natural Science and Technology of Kanazawa University

in partial fulfillment of the requirement for the degree of

**Doctor of Philosophy**


Student Number **0723112103**

Author **Renzhong Huang**

Supervisor **Prof. Yoshihiko Uesugi**

Division of Electrical Engineering and Computer Science

Kanazawa University


March 2012

# Acknowledgements

I would like to express my sincere gratitude to my advisor, **Prof. Yoshihiko Uesugi**, for his continuous guidance and support throughout my doctoral studies. His deep insight, patience, and open-mindedness encouraged me to complete this research. I am also very thankful to **Prof. Yasunori Tanaka** who helped me overcome several difficulties during this research. This work could not have been done without his insight, experience, and continual support. I would like to thank the members of my dissertation committee, **Prof. Manabu Tanaka, Takahiro Kiwata**, and **Sotoshi Yamada**, for their valuable input, encouragement, and assistance.

I wish to express my heartfelt gratitude to my highly respected boss at Plasma Giken Co., Ltd, **Dr. Hirotaka Hukanuma**, for providing me with the opportunity to study. I will always remember his kindness, support, and help. My sincere thanks also go to all of my colleagues at Plasma Giken Co. for their assistance. I am especially thankful to **Mr. Naoyuki Ohno** for his assistance with the arc voltage measurements.

I would like to thank my parents, daughter, siblings, and relatives for their constant support throughout my student life. I dedicate this thesis to Wenhua, my greatest friend and loving wife.

# Abstract

The coating quality produced by plasma spraying is greatly influenced by jet instability in the plasma spray process, which is caused by arc root fluctuations. This instability reduces the reproducibility of plasma spraying, thereby limiting its further application. Major factors that contribute to this limited reproducibility are inadequate control of the dynamic behavior of the arc in the plasma spray torch and the effect of anode erosion on the plasma jet behavior. The present study is motivated by the demand for fundamental knowledge about the dynamic behavior of the arc in a plasma torch induced by its interaction with the processing gas flow. Most previous simulations of plasma torches are based on the assumption of local thermodynamic equilibrium (LTE). This assumption generates a thin layer with low electrical conductivity near the electrodes due to a low gas temperature, making it difficult for an electrical current to flow between the electrodes. Therefore, an important research topic for models based on the LTE assumption is to solve the problem of the low electrical conductivity near the electrodes.

Some previous studies have sought to overcome this problem with conventional LTE models. One representative LTE model (model 1) artificially sets a high electric conductivity near the electrode interface while another (model 2) artificially adjusts the electrical conductivity in an electric current channel by employing a criterion based on a preset breakdown electric field. However, both these models inevitably generate calculation errors (e.g., overestimates of the arc voltage and the arc length) due to the LTE assumption. The non-equilibrium (NLTE) model has been demonstrated to reduce the calculation error, but it is extremely difficult to solve the NLTE model. Therefore, the present study develops a new model (model 3) that is based on the LTE assumption that the electrical conductivity of the plasma gas is determined by the nominal electron temperature rather than the gas temperature.

To evaluate the validity of the new LTE model, three models (including the two

conventional LTE models) were utilized to describe the dynamic arc behavior in a plasma torch. Argon gas was employed as the plasma gas. The gas temperature, gas velocity, voltage drop, and the location of the arc attachment were calculated for each of the three models.

The results indicate that the two conventional LTE models can effectively mimic the fluctuations in a plasma torch. These results are consistent with experimental results for plasma jets in that they gave a non-axisymmetric plasma arc in an axisymmetric torch. The plasma arc calculated using the new LTE model was almost axisymmetric, although arc fluctuations were observed in the axial direction. Although the LTE model developed in the present study does not completely explain the fluctuations of the plasma jet, especially those in the radial direction, the calculated arc voltage and the location of the arc attachment were closer to those observed in experiments than the results obtained using the two conventional LTE models. This is because the new model corrects the underestimate of the electrical conductivity of the gas caused by the LTE assumption since it determines the plasma gas electrical conductivity by the nominal electron temperature rather than the gas temperature. Moreover, the two conventional LTE models gave much higher thermal energies of the plasma arc than those observed experimentally, whereas the thermal energies obtained using the newly developed LTE model strongly agreed with those observed in experiments. Thus, the two conventional LTE models are more suitable for modeling plasma arc fluctuations in a torch, whereas the new LTE model predicts the parameters of a plasma arc in a plasma torch more accurately.

The temperature and velocity of particles in the plasma jet directly determine the properties of prepared coatings. To estimate the in-flight particle temperature and velocity, the new LTE model was used to calculate the gas flow of the plasma jet from the gas temperature and velocity distributions at the torch exit. The particle trajectory, temperature, and velocity in the plasma jet are also discussed. The calculated particle temperature and velocity were almost identical to those measured experimentally.

# Table of Contents

# Chapter 1
# Introduction

## 1.1. Plasmas

### 1.1.1 Preliminary definition of plasma

Plasmas are partially or fully ionized gases that consist of many electrons, ions, neutral atoms, and possibly molecules. They are usually considered to be the fourth state of matter in the sequence: solid, liquid, gas, and plasma. This classification of plasma as a state of matter is justified by the fact that plasmas make up more than 99% of the known universe (for example, the sun is a plasma).

One of the most fundamental properties of plasmas is quasi-neutral which is a state exhibiting electrical neutral macroscopically due to the balance of negatively and positively charged particles each other in plasmas. Unlike ordinary gases, plasmas are electrically conducting due to the existence of free charge carriers, especially the high temperature plasma. Plasmas have much higher energy densities than solids, liquids, and ordinary gases, which makes them suitable for several important applications [1].

Just as for any gaseous medium, the kinetic temperature of a plasma is defined in terms of the average kinetic energy of its constituent particles (i.e., molecules, atoms, ions, and electrons). The energy exchange should be existence between electron and heavy species (include the molecule, atom and ion) with the collision each other. Since electrons have a much lower mass than heavy species, many collisions are required to eliminate the energy (or temperature) difference between electrons and heavy species. Plasmas that are far from kinetic equilibrium [$T_e$ (Electron temperature)>> $T_h$ (Heavy particle temperature)] are classified as non-thermal plasmas. Non-thermal plasmas are frequently referred to as

cold plasmas because their heavy species have low temperatures, such as low pressure glow discharge plasmas, Corona discharge and etc [2]. Non-thermal plasmas are typically produced at pressures below 10 kPa, as shown in Figure 1-1. In contrast, plasmas that are in kinetic equilibrium and that are simultaneously in local thermodynamic equilibrium (LTE) are classified as thermal plasmas (e.g., arc plasmas and atmospheric radio-frequency (RF) discharge). There are so many collisions between electrons and heavy species that the heavy species and electrons have similar temperatures. Thermal plasmas are usually operated in a high pressure (i.e., $p$>10 kPa) to insure the sufficient number of particles for the enough collision between electron and heavy particles as shown in figure 1-1. Thermal plasmas typically have a temperature of about $10^4$ K with an electron density in the range $10^{21}$ to $10^{26}$ $m^{-3}$. The details of thermal plasma will be given in the next section.

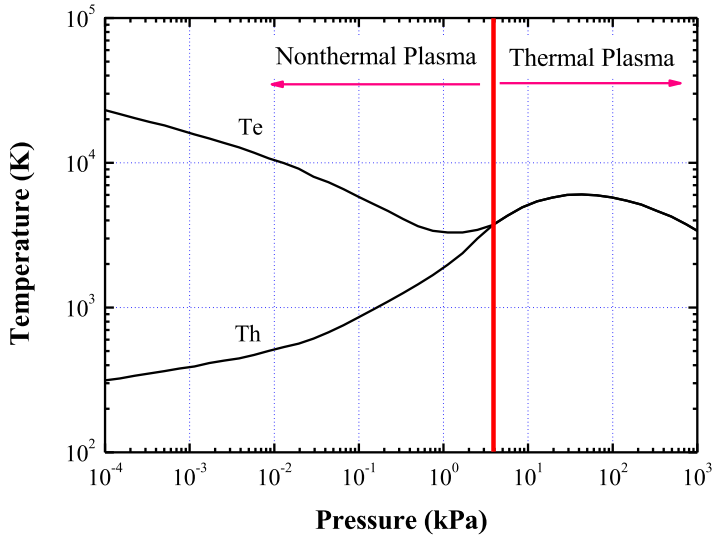


Figure 1-1. Dependence of electron temperature ($T_e$) and heavy particle temperature ($T_h$) in an arc plasma on the gas pressure for a constant discharge electric current [Reprint from Ref. 1]

### 1.1.2 Thermal plasma technology

Thermal plasmas, which are classified as “hot” plasmas, are in the state of LTE or close to it. In addition, they satisfy the following requirements:

- The various species that make up the plasma (i.e., atoms, ions, electrons, and molecules) share a single Maxwell distribution that is characterized by a single temperature.
- The ratio of the electric field to pressure is sufficiently small and the temperature is sufficiently high that the energy imparted to the charge carriers by the electric field is equilibrated by collisions.
- Collisions (not radiation) are the dominant mechanisms for ionization (Saha equilibrium) and excitation (Boltzmann distribution), and the collisions are microreversible.
- Spatial variations of the plasma properties are sufficiently small, so a given particle that diffuses from one location to another has sufficient time to equilibrate.

Since the early 1970s, thermal plasma processes have been used in many industrial applications including plasma spraying, thermal plasma chemical (or physical) vapor deposition, cutting, welding, remelting purification, smelting reduction, extractive metallurgy, ultrafine particle synthesis, powder spheroidization, waste treatment, circuit breakers, and lighting [1, 3–4]. The following characteristics make thermal plasmas attractive for materials processing [5–6]:

- They have high energy densities (~$10^6$–$10^7$ J/$m^3$) due to high heat flux energy densities (~$10^7$–$10^9$ W/$m^3$), which is mainly due to the release of ionization energy from the gas. This allows them to be used to melt and modify hard, high-melting point materials.
- They have a high luminosity due to the presence of excited states, which makes them useful for lighting applications.

- They have high electrical and thermal conductivities due to the high density of free electrons. This permits them to be generated from electrical discharges.
- They have very high quenching rates (～$10^6$ - $10^8$ K/s)
- They can be generated in pure and controlled atmospheres that produce minimal contamination. Furthermore, the reactor atmosphere can be adjusted to be inert, oxidizing, or reacting.

Thermal plasma can be generated by passing an electric current through a gas. Since gases at room temperature are excellent insulators, a sufficient number of charge carriers must be generated to make the gas electrically conducting. This process is known as electrical breakdown.

Thermal plasmas can be generated by passing an electric current through a gas. Gases are excellent insulators at room temperature; to make a gas electrically conducting, a high density of charge carriers must be generated. This process is known as electrical breakdown. There are many possible ways to realize breakdown. It is common to establish a conducting path between a pair of electrodes in an initially non-conducting gas atmosphere. The passage of electrical current through an ionized gas leads to an array of phenomena known as gaseous discharge. Depending on its applications, plasmas are produces by electrodeless RF (radio frequency) discharges, microwaves, shock waves, heating in a furnace, and laser or high-energy particle beams [1].

## 1.2. Arc Plasma Torch

Plasma torches are usually the main components that convert the electrical energy into thermal energy. Plasma torches can be classified into three types (RF, AC, and DC torches) based on the power source used to generate a plasma and the mode of thermal energy transfer to the job. Figure 1-2 schematically depicts the three types of plasma torches [4, 7–8].

RF plasma torches transfer electromagnetic energy from the RF source to the plasma

gas by inductive or capacitive coupling. They prevent the plasma being contaminated by metallic vapors because the plasma gas is not in direct contact with the electrodes. They are commonly used at powers in the range 30–100 kW. As the gas velocity is approximately inversely proportional to the square of the torch, it means that plasmas gas velocity is below 100 m/s [7].

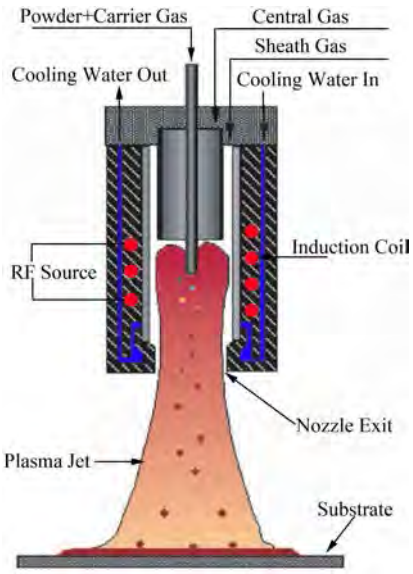


(a) RF plasma torch

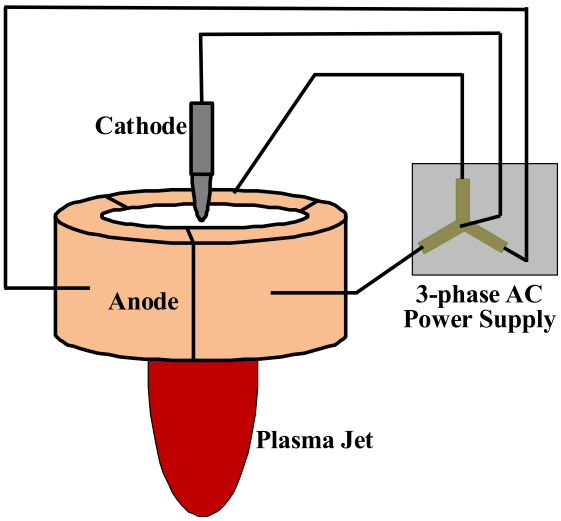


(b) AC plasma torch

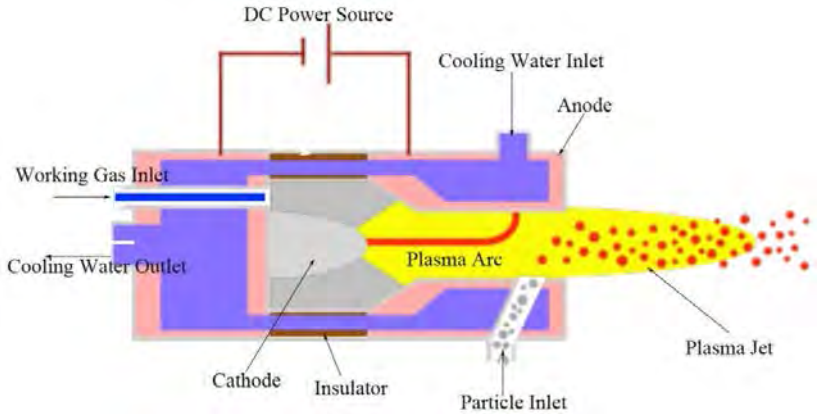


(c) DC plasma torch (Non-transferred type)

Figure 1-2. Schematics depicting the three different types of plasma torches.

AC plasma torches have been used more and more extensively based on the application of high-power plasma generators [9]. In these generators, the gas is heated by the energy of alternating current of industrial frequency. Since the polarity of the electrodes in the AC plasma torch (cathode-anode) changes with the phase of electrical mains, the wear of the electrodes is uniform resulting in long lifetimes. However, AC plasma torches are not currently used widely since the application of an AC causes various difficulties associated with time-dependent electrical parameters. AC plasma torches are classified single-phase and three-phase AC plasma torches based on the phase of the power supply.

DC arc plasma torches convert DC electrical energy to heat energy by ionization of the working gas. They are more extensively employed in many industrial applications than AC arc plasma torches because they generate less flicker and noise, operate more stably, are more controllable, and have lower power consumptions [10]. DC arc plasma torches are generally the primary component of processes such as plasma spraying, ultrafine particle synthesis, metal welding and cutting, extractive metallurgy, waste treatment, and biogas production [6]. Most DC arc torches have three main components: the cathode, the plasma-forming gas injection stage, and the anode. DC arc plasma generators can be categorized as transferred and non-transferred arc plasma torches based on their electrode configuration and current transfer mode as shown in figure 1-3. The electrode configuration is the biggest difference between these two types of torches. In transferred arc plasma torches, one of the electrodes is located outside the torch (it is generally the workpiece to be heated) and the arc is transferred directly from the cathode to the workpiece. In non-transferred arc plasma torches, both the cathode and anode are located inside the torch. The arc is generated between these electrodes and the plasma plume is ejected from the torch.

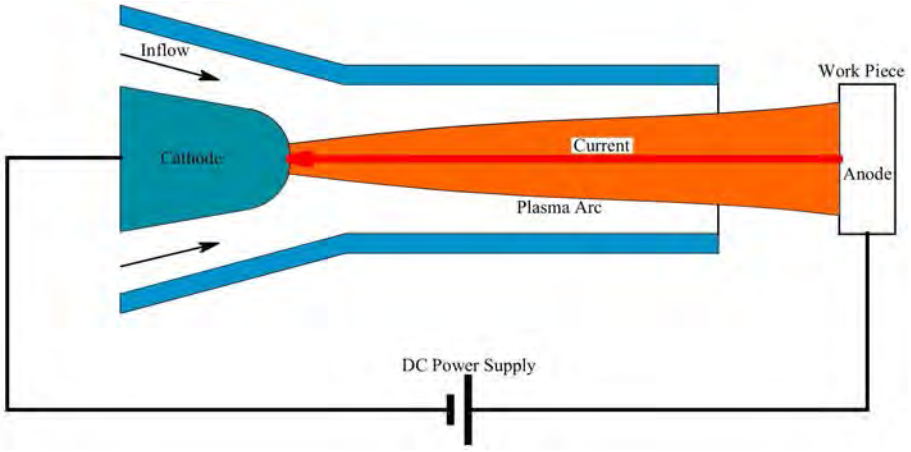


(a) Transferred arc plasma torch

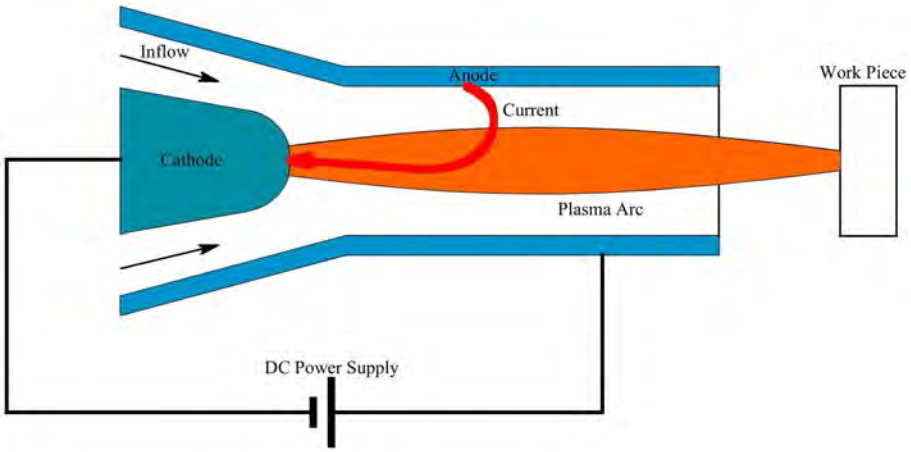


(b) Non-transferred arc plasma torch

Figure 1-3. Schematics depicting transferred and non-transferred arc plasma torches.

## 1.3. Plasma Spray Technology

Plasma spraying is an important example of an application that employs arc plasma torches [6]. Plasma spraying is a thermal spraying technique in which finely divided metallic and non-metallic materials are deposited in a molten or semi-molten state on a prepared substrate. The thermal plasma heat sources used (DC arc or RF discharge) can

generate temperatures of over 8000 K at atmospheric pressure, which is sufficiently high to melt most materials [7]. Figure 1-4 shows a typical plasma spray system that consists of a plasma gun, a power supply, a powder feeder, an arc starter, a control console, a gas supply, and a cooling water supply.

Plasma spraying is usually employed to deposit coatings that protect materials against wear, erosion, corrosion, and thermal loads [7]. Some of the main advantages of plasma spraying are: its flexibility, as its large number of parameters permits adaptation to different conditions, and the control of the plasma gas, power input, and torch configuration, allowing the spraying of a wide variety of materials in a wide variety of environments. Paradoxically, its flexibility can also be a disadvantage as the large number of independent variables makes it difficult to control the process. Other disadvantages are the reduced coating reproducibility due to the unsteady nature of the plasma jet, and the relatively low utilization of electrical energy into the working material (i.e. only ~ 3% of the input power is used for particle heating). Ideally, plasma spraying would produce uniform, reproducible coatings that are independent of uncontrolled factors (including uncontrollable factors). This may require careful and robust design of the spraying system that has an active control strategy.

The main torches employed by plasma spray are DC arc plasma torch in the industrial field. A conventional DC plasma spray torch (more than 90% of industrial torches) with a stick type cathode is shown schematically in figure 1-5. The cathode and the anode nozzle are made of thoriated (2 wt.%) tungsten and high-purity oxygen-free copper, respectively. Inside the torch, the working gas flows around the cathode and through the anode, which is shaped as a constricting nozzle. The plasma is initiated by a high voltage pulse, which produces localized ionization, generating a conductive path for an electric arc between the cathode and the anode. The electric heating produced by the arc heats the gas to very high temperatures (15,000–25,000 K), which causes the gas to dissociate and ionize, forming a plasma. Since the cold gas around the surface of the water-cooled anode nozzle is

electrically non-conductive, it constricts the plasma, increasing its temperature and velocity [1]. The plasma gases ejected from the torch form a plasma jet. Materials injected into the plasma jet are accelerated and completely or partially melted before they flatten and solidify onto the substrate (forming lamellae or splats), the coatings being built by the layering of splats as shown in figure 1-5.

Most commercial plasma spray torches operate at atmospheric pressure with electric powers between 10 and 100 kW, arc currents between 250 and 1000 A, arc voltages between 30 and 100 V, and flow rates between 20 and 150 standard liters per minute SLM. Common gases used in thermal plasma processing are Ar, He, $H_2$, $N_2$, $O_2$, and mixtures of these [7, 11–12].

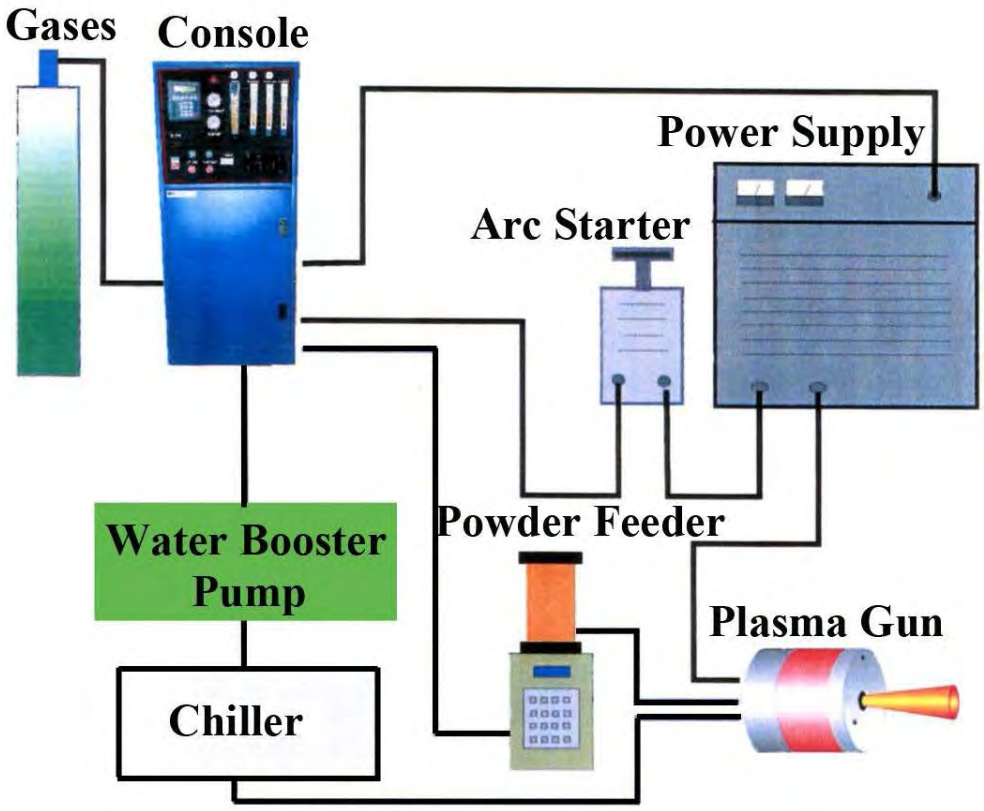


Figure 1-4. Schematic of the plasma spray system.

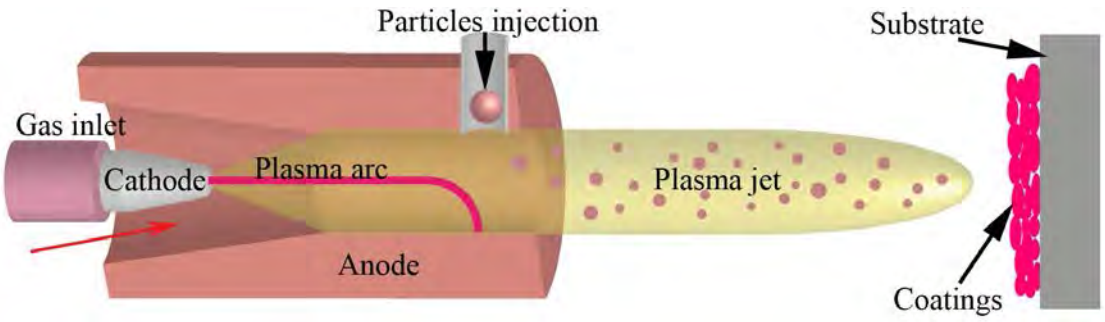


Figure 1-5. Schematic of a conventional DC arc plasma torch for thermal spraying.

### 1.3.1 Plasma arc

In plasma spraying, arc behavior is the key factor that determines the plasma jet outside the plasma torch and the coating properties. The electric arc in the torch can be divided into three regions: the cathode region, the arc column, and the anode region. The cathode arc root of a thermionic cathode is generally stable, whereas the anodic arc root usually moves along the anode surface as shown in figure 1-6. Although the mechanism responsible for the arc instability has not been completely determined, the arc dynamics in a DC arc plasma torch are known to be mostly due to an imbalance between the electromagnetic (or Lorentz) force, which is produced by local curvature of the current path and the self-induced magnetic field, and the flow drag generated by the interaction between the incoming cold gas and the hot, low-density plasma arc [13]. If the Lorentz force equals the drag force, then a steady attachment is obtained, which is characterized by negligible movement of the arc. However, in most cases, the plasma arc in an arc plasma torch is unsteady because of gas flow turbulence and the highly nonlinear electromagnetic properties of the plasma gas. If the drag force is greater than the electromagnetic force, the flow will drive the arc downstream. As the arc moves downstream, it lengthens and the total voltage drop and the magnitude of the electric field around the arc both increase. If the voltage (or local electric field) across the arc exceeds a critical value, a new arc root will form upstream of the original arc root by breakdown, as schematically depicted in

figure 1-6. Remarkably, the flow is inherently three-dimensional and time dependent despite the geometry and boundary conditions both being axial symmetric and steady [6, 14–18].

Three operational modes are distinguished based on the symptomatic behavior of the arc: steady, takeover, and restrike modes [15, 19]. Because the total voltage drop across the torch (torch voltage) varies approximately linearly with the arc length, the variation of the total voltage drop over time gives an indication of the arc dynamics in the torch. The characteristics of the voltage drop signal over time for given operating conditions have led to the identification of the above-mentioned three distinct operation modes of the torch [13, 19]. The voltage drop signals for the three different modes of operation are schematically shown in figure 1-7.

- Steady mode

  In this mode, the drag and Lorentz forces acting on the plasma arc (see figure 1-6) are balanced. Consequently, the arc root fixes on one position without movement or transfer. Therefore, fluctuations in the arc voltage are negligible and the position of the arc attachment on the anode remains almost constant. This mode is obtained at relatively large currents and/or relatively small flow rates. This mode is not desirable due to the rapid erosion of the anode.

- Takeover mode

  In this mode, a new attachment gradually takes over from an old attachment resulting in (quasi-)periodic fluctuations in the voltage drop and a corresponding (quasi-)periodic movement of the arc. This is the most desirable operating mode for plasma spray torches because it allows an adequate distribution of the heat load to the anode and the well-defined fluctuations of the arc result in a reproducible spraying process. This operating mode is obtained at moderate currents and working gas flow rates.

- Restrike mode

  In this mode, the arc is considerably unstable and has relatively unpredictable movement resulting in large voltage fluctuations. This mode is obtained at relatively large mass flow rates and/or relatively low currents. This mode strongly enhances jet fluctuations in the axial direction, cold flow entrainment, and turbulence, which limit the reproducibility of the coating quality.

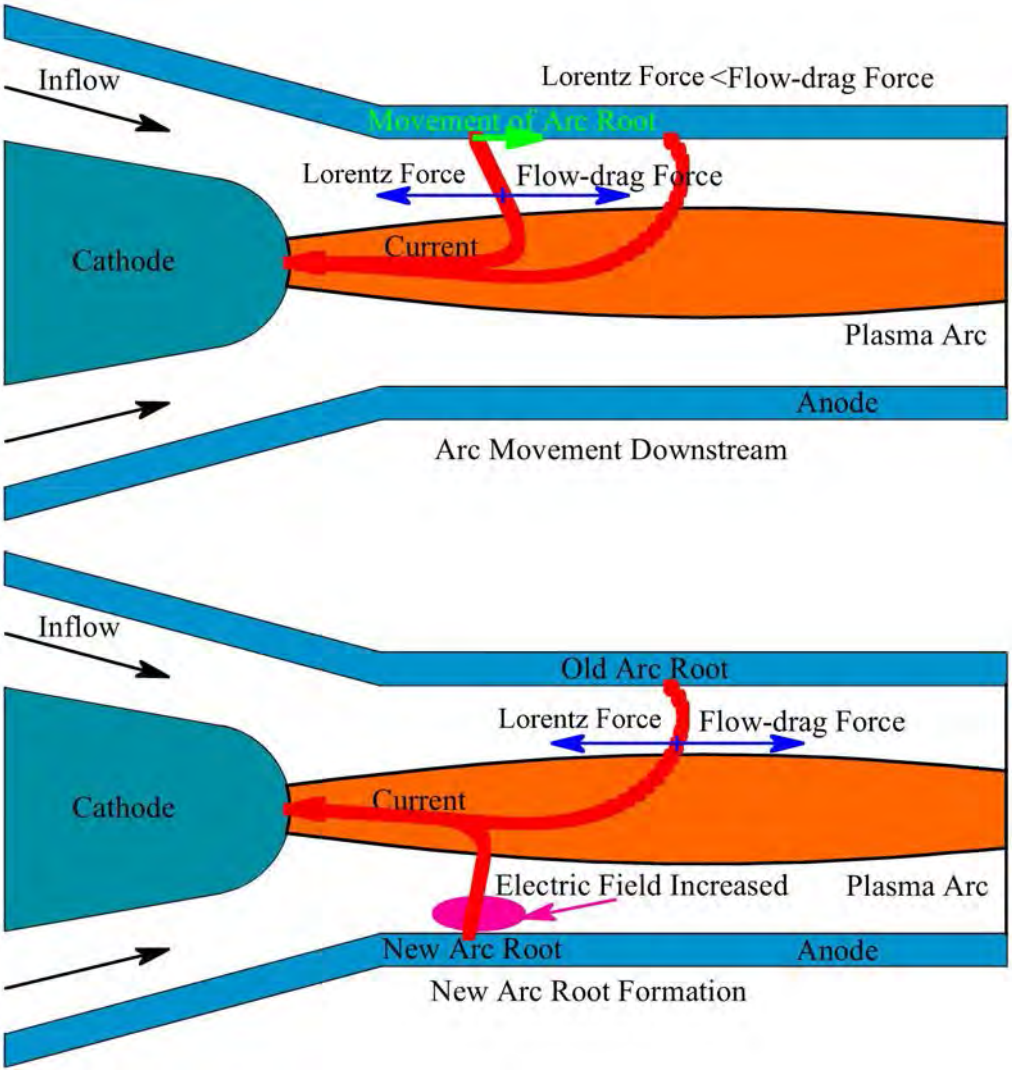


Figure 1-6. Arc movement due to imbalance between flow drag and electromagnetic (Lorentz) forces.

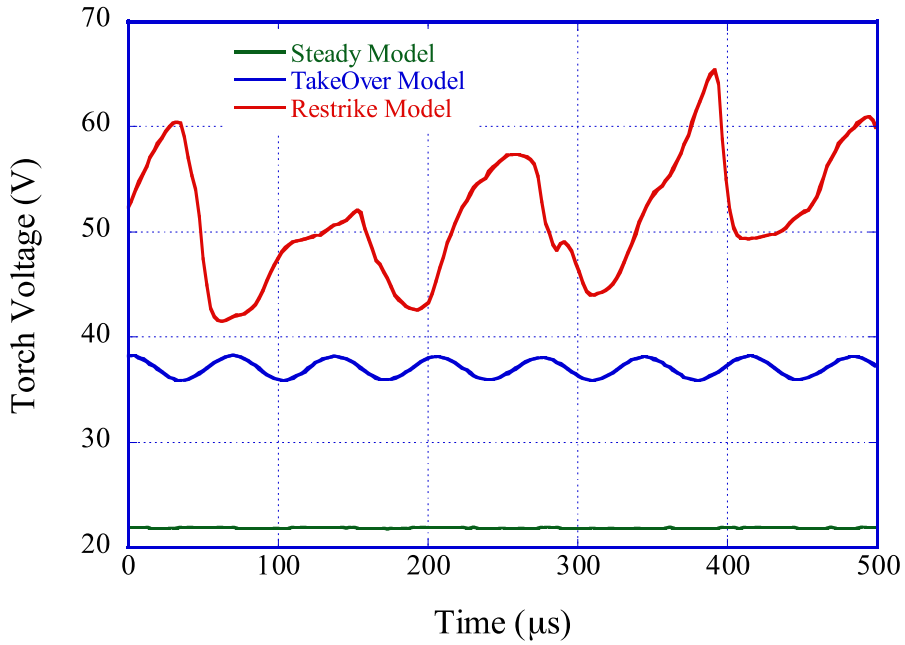


Figure 1-7. Schematic plot of voltage drop signals for the three operating modes of an arc plasma torch [13, 19].

The arc fluctuations in the torch significantly affect the electrode lifetimes and the electrothermal efficiency of the torch. A better understanding of the arc dynamics in the torch and the effect of the operational parameters on the arc characteristics should enable torches to be designed that have higher electrothermal efficiencies and longer electrode lifetimes.

### 1.3.2 Plasma jets

The plasma jet temperature, generally assuming local thermodynamic equilibrium (LTE) and its surrounding atmosphere entrainment (provided the latter is different from plasma forming gases) are characterized by: emission spectroscopy (mostly from atomic lines 8000 <T<14,000K), Rayleigh scattering (T< 10,000 or 16,000K depending on the resolution), and coherent anti-stokes Raman spectroscopy (CARS) (T< 10,000K). The plasma jet velocity at the torch exit varies from 600 m/s for pure Ar gas to 2200 m/s for Ar–$H_2$ mixed gas [7].

The plasma jet from a non-transferred arc plasma torch is usually very unstable. Plasma jet instabilities are caused in part by the high density and velocity gradients at the interface between the jet and the surrounding gas and by the pulsating force due to the arc moving in the torch. These instabilities generate eddy roll-ups at the interface between the plasma and the surrounding gas and eventually lead to large-scale turbulence [20–22], as depicted in figure 1-5.

The hot plasma jet can be considered to be a temporal flow due to its self-excited nature, which means that no external excitation is required to make the jet unstable. Furthermore, this type of flow (i.e., a hot jet discharging into a cold environment) is unconditionally unstable for a temperature ratio $T_{jet}/T_{environment} > 1.52$; this condition is almost always fulfilled in plasma jets for which the temperature ratio can readily exceed 10 ($T_{jet} \approx 10{,}000$ K; $T_{environment} < 1000$ K) [15]. Furthermore, the arc movement in the torch acts as a forcing mechanism, enhancing the inherently unstable nature of the plasma jet. Figure 1-8 shows the undulating motion of the plasma jet due to the arc dynamics in the torch [23]. A better understanding of the arc dynamics inside the torch and their role in forcing the plasma jet would assist design optimization of arc plasma torches, which could translate into more efficient, reliable, and reproducible plasma processes (particularly, plasma spray coating).

Besides the gas flow of the plasma jet, the parameters of the particles in the plasma arc are very important for understanding the properties of sprayed coatings. The ideal situation in plasma spraying would be when all particles that are injected reach the substrates with a temperature over their melting point and are uniformly heated (but not over heated: no vaporization, for example) with velocities as high as possible but compatible with a fully melted state [12, 24-25]. Gaining an understanding of plasma–particle interactions is critical for controlling the spray process, particularly its reliability and reproducibility. This is, however, a very complex problem due to the range of sizes (5–140 μm), velocities (50–500 m/s), and temperatures (1200–4500 K) of the

particles. In addition, plasma volumetric continuum emission, which is very high ($10^8$–$10^9$ W/m$^3$) at the core, will be drastically enhanced when particle vaporization occurs [1]. Initially, many laboratory set-ups were developed in the 1980s to study in-flight particles in plasma jets and their plumes. New sensors for spray process monitoring that could function in the harsh environment of spray booths were developed in the 1990s. They are mainly based on charge coupled devices (CCD) cameras and fast pyrometers [26–32]. A better understanding of the arc plasma jet and the particles in it would facilitate the control of the properties of plasma sprayed coatings by adjusting the operating conditions.

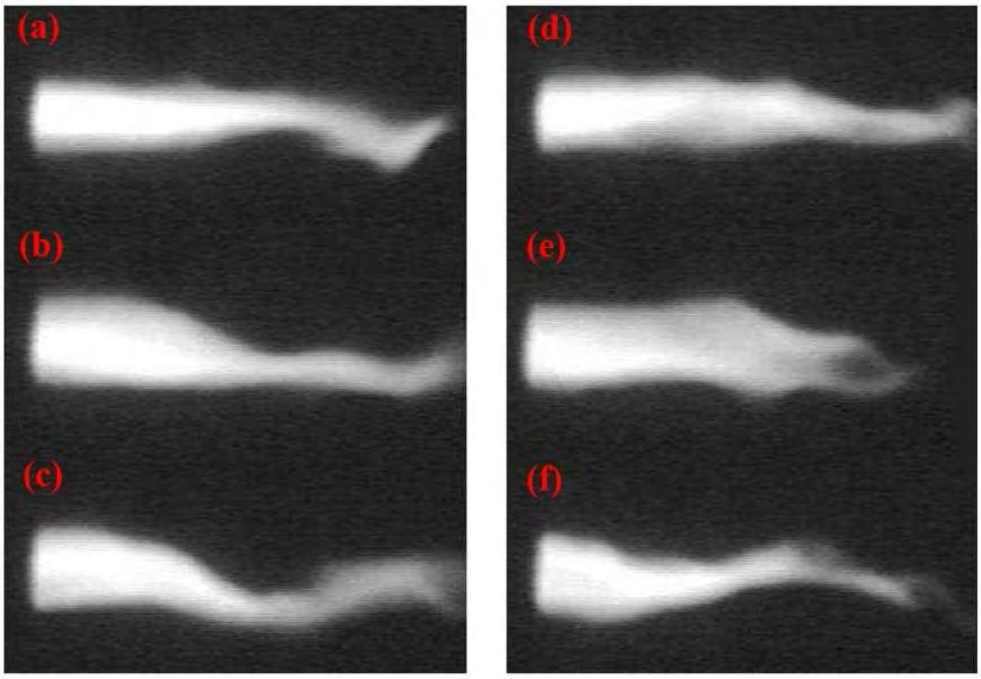


Figure 1-8. Time sequence of optical images of a plasma jet plume (~10 μs between frames) [Reprint from Ref. 23].

## 1.4. Motivation for this Research

Thermal plasma technology has been extensively used in materials processing since the early 1970s. It has been extensively studied through both measurements and modeling [7]. For the many applications based on thermal plasmas, plasma spraying is one of the most widely used. Despite its versatility, its limited reproducibility and low process efficiency have hindered its wider application. A major factor for this limited reproducibility is related to an inadequate understanding of the dynamics of the arc in the torch. In recent years, several robust, user-friendly particle diagnostic tools have become available for assessing the in-flight particle temperature, velocity, trajectory, and particle diameter distributions of plasma spray processes. However, many fundamentals are still poorly understood, particularly the dynamic behavior of an arc confined in a torch due to its interaction with the processing gas stream [19, 26, 33]. The arc movement in a torch has a first-order effect on both the coating quality (due to jet forcing, which enhances cold flow entrainment and non-uniform powder heating) and the anode lifetime (due to the localized heating of the anode). A better understanding of the arc dynamics inside arc plasma torches would enable improved torch designs and process controls to be developed, resulting in superior plasma processes, particularly plasma spray coating. Gaining an understanding of flow instabilities in arc plasma torches is one of the main efforts in research and development of plasma spraying technology [34].

Even though it is important to understand the plasma arc behavior inside the arc plasma torch, the coating properties are directly determined by the in-flight particle temperature and velocity. For the plasma spray process, it is very helpful to predict the particle temperature and velocity in the plasma jet. As a feedback, the predicted results benefit the control of spray conditions.

It is extremely difficult to directly observe the complete dynamics of the arc in the torch due to the intense radiation emitted from the arc and its confinement in the arc

plasma torch. It is also difficult to measure the temperature and velocity in the plasma jet due to the high temperature and gradients. In order to fulfill the measurement of the plasma jet, Expensive equipment is necessary. This situation has prompted the development of computational models for describing thermal plasma flows to enhance our understanding of the arc dynamics in arc plasma torches and to predict the particle temperature and velocity in a plasma jet. This research is motivated by the need to gain a fundamental understanding of the dynamic behavior of an arc generated by its interaction with processing gas flow in an arc plasma torch and to predict the in-flight particle parameters. The aim of this study is to gain a better understanding of arc behavior and thereby reduce anode erosion and enhance the plasma jet characteristics and the factors that affect the coating properties.

## 1.5. Scope and Approach of this Thesis

This thesis describes the development and implementation of modeling approaches for simulating plasma flow instabilities in plasma spray processes in non-transferred arc plasma torches and the plasma jet temperature and velocity. It is very challenging to model flow instabilities in arc plasma torches because the flow is inherently three-dimensional, time-dependent, and highly nonlinear, has high property gradients, is characterized by a wide range of time and spatial scales, and often includes chemical and thermal non-equilibrium effects, especially near the plasma boundaries. This thesis presents three modeling approaches: two conventional models and a newly developed model based on the LTE approximation. The difference among the three models is the adopted methods to ensure the electrical current passing through the low-temperature region near the electrodes. One conventional LTE model (model 1) artificially sets a high electric conductivity in the vicinity of electrode boundary while the other (model 2) artificially adjusts the electrical conductivity in an electric current path by employing a criterion based on a preset breakdown electric field. In the new model (model 3), the electrical conductivity of the

plasma gas is determined by the nominal electron temperature rather than the gas temperature.

In the current studies, the goal of the simulation is not to describe the physical process in which a new arc attachment forms, but rather to model the effect of the reattachment process on the dynamic behavior of the plasma flow. Using Model 1, a commercial non-transferred arc plasma torch operating with argon gas under different operating conditions was modeled. Even though model 1 is the simplest of the three models with the lowest computational cost, it effectively modeled the instability of the plasma arc in the plasma torch due to movement of the anodic arc root. However, the calculated arc voltage is much higher than the measured arc voltage due to the arc being longer in the simulation. To make the calculated arc voltage closer to the measured one, a criterion was employed to determine the new arc attachments by evaluating the local electric field in model 2. Using model 2, the arc dynamic behavior in the plasma torch can be modeled and the anode arc root is closer to the erosion position than the results obtained using model 1. However, like model 1, the arc voltage is still higher than the measured one due to the electrical conductivity being underestimated due to the LTE assumption. Unlike the non-equilibrium (NLTE) model being significant complexity, a novel LTE model (model 3) was developed to reduce the deviation caused by the LTE assumption. Model 3 employs a nominal electron temperature, which is based on the gas temperature and is modified by the electric field, to determine the gas electrical conductivity. Model 3 gives an arc voltage that is much closer to the measured one due to the arc attachment position being similar to that observed experimentally; moreover, the calculated heat energy of the plasma arc is almost identical to the measured one. However, the calculated arc was almost axisymmetric even through the arc fluctuated in axial direction. It seems that the radial movement of the arc cannot be modeled by model 3. Despite this, model 3 predicted the arc root position and the heat energy of the plasma arc more accurately than the two conventional models. Not taking consideration of the instability of the plasma arc inside the torch, the results

obtained using model 3 are closer to the measured ones than those of the two conventional models. The results calculated obtained by model 3 can thus be used to predict the average parameters of the plasma arc. Based on this, a steady-state 3D model was developed to predict the average particle temperature and velocity in the plasma jet outside the plasma torch using the results calculated by model 3. This model appears to be able to accurately predict the in-flight particle parameters.

This thesis is organized as follows:

Chapter 2 briefly describes measurements of a plasma torch and a plasma jet in order to provide reference values for the simulations. The arc voltage and current were measured to verify the calculated results. The heat energy of the plasma arc was also deduced by measuring the energy removed by the cooling water. The plasma jet was observed and the in-flight particle temperature and velocity were measured by both DPV-2000 system and SprayWatch system.

Chapter 3 presents the results and discusses the arc behavior in a plasma torch. This chapter describes implementation of the three models based on the LTE assumption to model the arc instability in a plasma torch. The characteristics of the three models are also discussed. The calculated arc voltage and the heat energy of the plasma arc are compared with the measured results.

Chapter 4 presents the results for gas flow and particle parameters in the plasma jet. The gas temperature and velocity of the plasma jet outside the plasma torch were calculated using the calculated gas temperature and velocity at the plasma torch exit obtained in Chapter 3. The particle temperature and velocity are also discussed. Finally, the calculated particle temperature and velocity are compared with the experimental ones.

A summary and recommendations for future work are given in Chapter 5.

## References

[1]. Boulos, M. I., Fauchais, P., and Pfender E., Thermal Plasmas: Fundamentals and Applications, Plenum Press, New York, 1994.

[2]. Vijay Nehra, Ashok Kumar and H K Dwivedi, Atmospheric Non-Thermal Plasma Sources, International Journal of Engineering, Volume (2): Issue (1) 2008.

[3]. Fauchais, P. and Vardelle, A., Thermal Plasmas, IEEE Transactions on Plasma Science, Vol. 25, No. 6, 1258-1280, 1997.

[4]. Venkatramani N., Industrial plasma torches and applications, Current Science, Vol. 83, No. 3, 10 August 2002.

[5]. Heberlein, J. V. R. and Voshall, R. E., Thermal Plasma Devices, Encyclopedia of Applied Physics, Vol. 21, 163-191, 1997.

[6]. Trelles J.P., Chazelas C., Vardelle A., and Heberlein J.V.R., Arc Plasma Torch Modeling, Journal of Thermal Spray Technology, Volume 18, Numbers 5-6, 728-752, 2009.

[7]. Fauchais P., Understanding plasma spraying, J. Phys. D: Appl. Phys. 37, R86–R108, 2004.

[8]. Mihovsky M., Thermal Plasma Application in Metallurgy, Journal of the University of Chemical Technology and Metallurgy, V45, No. 1, 3-18, 2010.

[9]. Zhukov M. F. and Zasypkin I. M., Thermal Plasma Torches: Design, Characteristics, Application, Cambridge Int Science Publishing, 2007.

[10]. Gomez E., Amutha Rani D., Cheeseman C.R., Deegan D., Wise M., Boccaccini A.R., Thermal plasma technology for the treatment of wastes: A critical review, Journal of Hazardous Materials, 161, (2009), 614–626.

[11]. Shanmugavelayutham G. and selvarajan V., Electrothermal efficiency, temperature and thermal conductivity of plasma jet in a DC plasma spray torch, Pramana-J. Phys., Vol. 61, No. 6, 1109–1119, December 2003.

[12]. Lech Pawlowski, The Science and Engineering of Thermal Spray Coatings: Second Edition, John Wiley& Sons, Ltd., 2008.

[13]. Wutzke, S. A., Conditions Governing the Symptomatic Behavior of an Electric Arc in Superimposed Flow Field, Ph. D. Thesis, University of Minnesota, 1967.

[14]. Trelles J. P. and Heberlein J. V. R., Simulation results of Arc Behavior in Different Plasma Spray Torches, Journal of Thermal Spray Technology, Volume 15, Number 4 (2006), 563-569.

[15]. Trelles J. P., Finite Element Modeling of Flow Instabilities in Arc Plasma Torches, Ph. D. Thesis, University of Minnesota, 2007.

[16]. Trelles J. P., Heberlein J. and Pfender E., Non-equilibrium Modelling of Arc Plasma Torches, Journal of Physics D: Applied Physics, Volume 40, Number 19 (2007), 5937.

[17]. Trelles J. P., Pfender E. and Heberlein J. V. R., Modelling of the arc reattachment process in plasma torches, Journal of Physics D: Applied Physics, Volume 40, Number 18, 5635, 2007.

[18]. Trelles J. P., Pfender E. and Heberlein J., Multiscale Finite Element Modeling of Arc Dynamics in a DC Plasma Torch, Plasma Chem. Plasma Process (2006) V26, 557-575

[19]. Duan Z. and Heberlein J., Arc Instabilities in a Plasma Spray Torch, Journal of Thermal Spray Technology, Volume 11(1) March 2002, 44-51.

[20]. Pfender, E., Fincke, J., and Spores, R., Entrainment of Cold Gas into Thermal Plasma Jet, Plasma Chemistry and Plasma Processing, Vol. 11, No. 4, 529-543, 1991.

[21]. Levitan, Y. S., Electric Fluctuations Caused by Gas dynamic Turbulence in Electric-Arc Devices, IEEE Transactions on Plasma Science, Vol. 24, No. 1, 137-142, 1996.

[22]. Hlína, J., Šonský, J., Němička, V., and Zachar, A., Statistics of Turbulent Structures

in a Thermal Plasma Jet, Journal of Physics D: Applied Physics, Vol. 38, 1760-1768, 2005.

[23]. Outcalt D., Private Communication, High Temperature and Plasma Laboratory, Department of Mechanical Engineering, University of Minnesota, 2005.

[24]. Fauchais P, Vardelle A and Dussoubs B, Quo Vadis Thermal Spraying?, J. Thermal Spray Technol., V10, 44–66, 2001.

[25]. Vardelle A, Moreau C and Fauchais P, The Dynamics of Deposit Formation in Thermal-Spray Processes, MRS Bull., July 2000, 25, 32–37.

[26]. Coudert J. F., planche M. P., fauchais P., Characterization of DC Plasma Torch Voltage Fluctuations, Plasma Chemistry and Plasma Processing, Vol. 16, No. 1, 1996 (Supplement), 211s-227s.

[27]. Jahn R. E., Temperature distribution and thermal efficiency of low power arc-heated plasma jets, Br. J. Appl. Phys. 14, 585, 1963.

[28]. Capetti A. and Pfender E., Probe Measurements in Argon Plasma Jets Operated in Ambient Argon, Plasma Chemistry and Plasma Processing, Vol. 9, No. 2, 1989.

[29]. Planche M. P., Coudert J. F. and Fauchais P., Velocity Measurements for Arc Jets Produced by a DC Plasma Spray Torch, Plasma Chemistry and Plasma Processing, Vol. 18, No. 2, 1998.

[30]. Duan Z., Beall L., Schein J., Heberlein J., and Stachowicz M., Diagnostics and Modeling of an Argon/Helium Plasma Spray Process, Journal of Thermal Spray Technology, Volume 9(2), 225-234, June 2000.

[31]. Bahbou M.F. and Nylen P., On-Line Measurement of Plasma-Sprayed Ni-Particles during Impact on a Ti-Surface:Influence of Surface Oxidation, Journal of Thermal Spray Technology, Volume 16(4), 506–511, December 2007.

[32]. Goutier S., Nogues-Delbos E., Vardelle M. and Fauchais P., Particle Temperature Fluctuations in Plasma Spraying, Journal of Thermal Spray Technology, Volume 17(5-6), 895–901, Mid-December 2008.

[33]. Ramasamy R. and Selvarajan V., Current-voltage characteristics of a non-transferred plasma spray torch, Eur. Phys. J. D 8, 125–129 (2000).

[34]. Pfender E., Thermal Plasma Technology: Where Do We Stand and Where Are We Going?, Plasma Chemistry and Plasma Processing, Vol. 19, No. 1, 1-31, 1999.

# Chapter 2
# Fundamental Properties of Plasma Spray

## 2.1. Introduction

To verify the validity of the models for plasma arc simulation, some plasma arc parameters were measured experimentally. It is extremely difficult to measure the gas temperature and velocity of a plasma arc in a plasma torch since it requires high-performance instruments. Therefore, the voltage and current of a plasma torch were measured and were used to predict the arc behavior in the plasma torch; the heat energy of the plasma arc was also measured. Moreover, anode erosion of the plasma spray torch was observed to predict the position of the anodic arc root. It is also difficult to measure the gas temperature and velocity of a plasma jet outside the plasma torch. Images of plasma jets were obtained using a SprayWatch system to investigate fluctuations of the plasma jet and the in-flight particle temperature and velocity were measured using both DPV-2000 and SprayWatch systems.

## 2.2. Background of the Experiments to Measure Arc Behavior

It is relatively difficult to experimentally measure the plasma arc parameters inside a plasma torch due to the extremely high temperature and confined space. Most previous experiments measured the current–voltage characteristics, voltage fluctuations, and the arc parameters of the torch outlet. Ramasamy and Selvarajan [1] measured the current–voltage characteristics of a non-transferred plasma torch for different flow rates, gas mixtures, and electrode gaps. Coudert et al. [2] experimentally measured the temporal evolution of the arc voltage and the light emission at a point in the plasma jet close to the nozzle exit. They

found that upstream arc spots had 30–40% longer lifetimes than downstream arc spots, which may significantly affect electrode erosion. Vysohlid [3] investigated arc voltage fluctuations in a Praxair SG-100 plasma torch over a wide range of operating conditions and discussed the average velocity. Dorier et al. [4] investigated the fluctuating behavior of a Sulzer Metco F4 DC plasma gun by performing time-resolved measurements of the arc voltage in conjunction with end-on imaging of the electrode gap interior using a gated camera. The arc root position was determined by analyzing the images. They found that prior to arc reattachment, the arc root is optically diffused because the gas boundary layer is thin and hot, whereas they observed a constricted attachment through a thick and cold boundary layer immediately after a major restrike. They concluded that anode wear strongly affects the arc root position on the anode inner surface and that attachment preferentially occurs in eroded regions. They also found that the arc can have more than one attachment over a time interval of 1 μs. Duan and Heberlein [5] investigated the instabilities of a plasma arc and a plasma jet by performing high-speed end-on observations of the arc. The combination of voltage trace analysis and high-speed video imaging of an arc in a commercial plasma torch revealed quantitative correlations between the cold-gas boundary layer thickness and the instability mode for a range of operating parameters. They found that the plasma torch has three distinctive operating modes: the restrike mode, the takeover mode, and the steady mode. Huang et al. [6] used a high-speed video camera to observe arc root motion in a DC argon–hydrogen plasma at a reduced pressure and they analyzed the time-resolved angular position of the arc root attachment point. They found that the arc root exhibits a chaotic, jumping motion along the radial direction of the anode surface.

The key parameters that determine the properties of coatings produced by a plasma spray are the particle velocity and temperature prior to impact. Consequently, many studies have focused on the plasma spray jet outside a plasma torch; in particular, the plasma jet characteristics and the behavior of injected particles have been extensively studied

experimentally. Jahn [7] spectroscopically measured the temperature distribution in an arc-heated plasma jet (5 to 20 kW) operated using argon or nitrogen (15 to 60 l/min). Moreover, the average temperature was estimated from the heat input. Capetti and Pfender [8] used an enthalpy probe to measure local enthalpies and velocities in plasma jets generated by a DC plasma spray torch. The validity of the measured enthalpy and velocity profiles was checked by energy flux and mass flux balances; reasonable agreement was found between the input quantities, which were measured independently, and those obtained by integrating the experimental profiles. The data were compared with those obtained by operating the same torch in ambient air. The temperatures and velocities measured in pure argon were substantially higher than those in air; consequently, jets in argon appear wider and substantially longer than those in air. Coudert et al. [9] measured the axial component of the radial velocity distribution of a plasma flow generated by a nonintrusive optical technique. Pure Ar and Ar–$H_2$ plasma flows were measured by this method and the experimental results were validated by calculations of the enthalpy and mass balances. Planche et al. [10] used an optical technique to determine the axial velocity of plasma jets for various experimental conditions to systematically study the effect of the working parameters on the plasma velocity. The arc current was varied between 200 and 600 A, the gas flow rate between 30 and 80 SLM, and the internal nozzle diameter between 6 and 10 mm; the plasma gases were either an Ar–$H_2$ mixture or $N_2$. Relatively well-defined tendencies were observed and the arc stability appeared to greatly influence velocity fluctuations. Duan et al. [11] developed a simple diagnostic system to monitor plasma jet instabilities and particle properties. The plasma jet in the plasma spray process was imaged using a laser strobe video system and the in-flight particle properties were measured using a DPV-2000 system. The results obtained were used to establish relationships between the spray process parameters. The coating qualities improve with increasing current and secondary gas flow rate due lengthening of the plasma jet and more effective heating of the sprayed particles. Bahbou and Nylen [12] used a modified

DPV-2000 system to measure thermal radiation and velocity of individual plasma-sprayed particles. These online measurements are helpful for determining the physical phenomena that occur when thermally sprayed particles impact onto a substrate. Goutier et al. [13] measured the time variation of the particle temperature and its correlation with voltage variations using two online techniques. They performed experiments with three plasma torches (one F4 and two 3MB) using argon–hydrogen (F4 and 3MB) and nitrogen–hydrogen (3MB) mixtures (all in restrike mode for voltage fluctuations) as plasma-forming gases. The results revealed a good correlation between the arc voltage and particle temperature fluctuations when the plasma torch was operated with argon–hydrogen mixtures and a high mass flow rate. However, no such correlation was observed when the torch was operated with nitrogen–hydrogen mixtures, even when the amplitude of the voltage fluctuations was two to three times higher than those obtained with Ar–$H_2$ mixtures.

Previous studies of plasma arcs and torches generally measured the arc voltage characteristics of a plasma torch and the gas behavior at the torch exit, while studies of plasma jets generally detected the jet behavior and the in-flight particle parameters. In the present research, the voltage and current of the plasma torch were measured and used to predict the arc behavior inside the plasma torch; the thermal energy of the plasma arc was also measured. Moreover, anode erosion of the plasma spray torch was observed to predict the position of the anode arc root. For the plasma jet outside the plasma torch, images of plasma jets were obtained using the SprayWatch system to clarify the fluctuation of the plasma jet and the in-flight particle temperature and velocity were measured with DPV-2000 and SprayWatch systems.

## 2.3. Experimental Equipment and Procedures

### 2.3.1 Plasma spray system

Figure 2-1 shows photographs of some components of the plasma spray system used in the present study. This system is an 80 kW automatic plasma spray system that was developed by Plasmadyne (a division of Geotel Inc.). It consists of a control console, a plasma spray gun, a power supply, a high-frequency starter, a powder feeding system, and a water cooling system (see figure 1-4). The important components of this system are the power supply, the control console, and the plasma spray gun (see figure 2-1).

Two thyristor-controlled DC power supplies (PS-61S) with a maximum capacity of 80 kW under continuous operation were employed as the power source for generating a plasma. The maximum current was 1000 A and the voltage was 80 V. The power supply could be operated from the control console.

The control console is upright and has all the controls and gauges necessary to operate the system. The console contains an automatic control unit, which allows automatic sequencing of the starting, operating, and shut down functions, and a safety interlock annunciator system.

The plasma torch used in the experiments is a non-transferred arc type (see figure 2-2). It has a copper rod cathode with a thoriated tungsten tip and a copper nozzle anode. The nozzle has a port near its edge for feeding the carrier gas and powder. To reduce electrode wear, electrodes are protected by an efficient water cooling system. During operation, the electrodes and electrical cables are cooled by chilled water.

(a) Control console

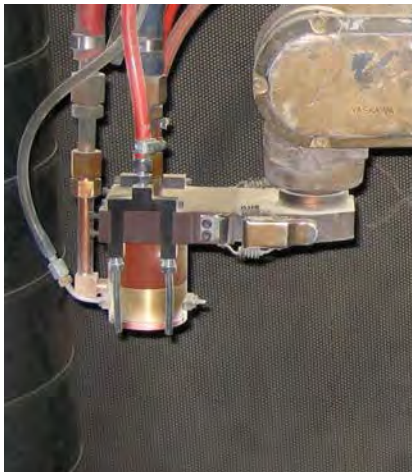

(b) Gun

(c) Power supply

Figure 2-1. Photographs of three components of the plasma spray system

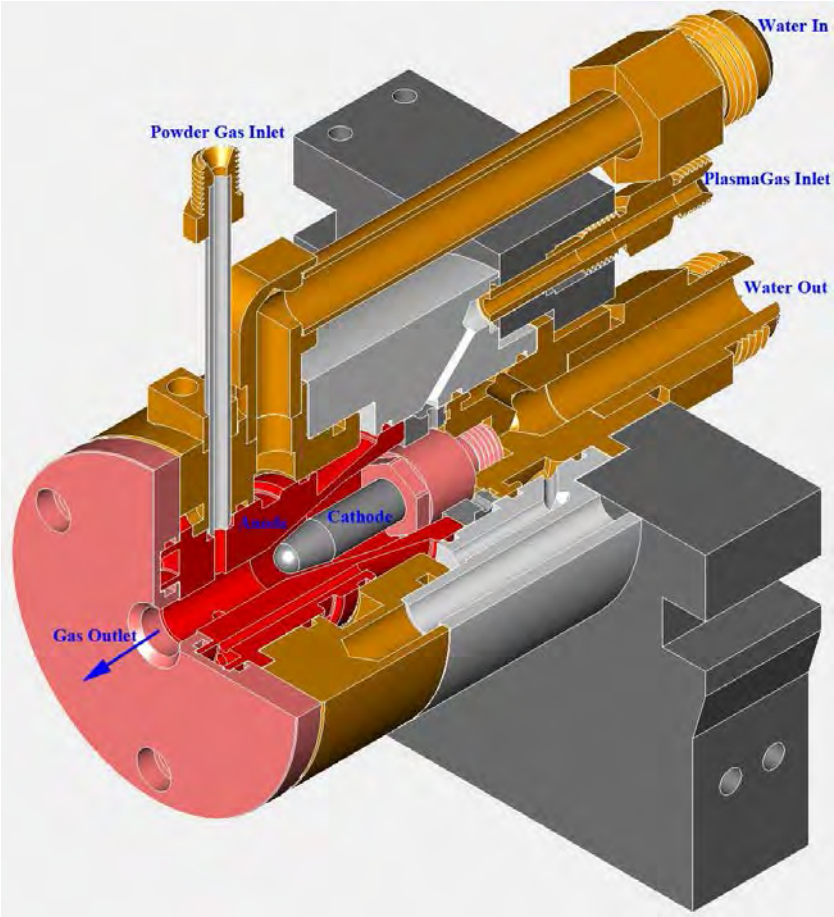


Figure 2-2. Schematic of plasma torch SG-100

### 2.3.2 DPV-2000 system

The DPV-2000 system from Tecnar Automation (Saint-Bruno, QC, Canada) is a new optical sensing device used in thermal spray processes. The system employs infrared pyrometry along with a dual slit optical device to perform in-flight diagnostics on individual particles. The DPV-2000 system provides precise temperature, velocity, and diameter measurements of up to 800 individual particles/s depending on the spraying conditions. Figure 2-3 shows a schematic of the DPV-2000 system. It consists of three main components: a sensor head, a detection module containing optical components and photodetectors, and a control module. A detailed description of the system is given in Ref. 14. To detect the cold particles (with a low temperature), a high-power diode laser is used

to illuminate in-flight particles (see figure 2-3).

Figure 2-4 shows the general setup of the optical sensor head and a photograph of the measurement system. When a particle travels through the field of view of the sensor head (i.e., the mask image), a corresponding image spot will form due to the radiation light from the particles in the plant where the two-slit mask is placed. The movement of such an image spot in the mask is converted into a two-peak signal and transmitted to the detection module by an optical fiber. The collected optical signals are spectrally separated by a dichroic mirror and then filtered by two bandpass filters centered at 995 and 787 nm. Signals from both detectors are amplified, digitized, and fed to a computer.

Figure 2-5 shows a typical two-peak signal detected by the system. From the two-peak signal, the particle velocity $v$ is defined as [15–16]

$$v = \frac{s}{TOF} \times M_l \qquad (Eq. 2-1)$$

where $TOF$ is the flight time between the two light pluses collected when the particle image spot moves from the first slit to the second one, $s$ is the distance between the two slits, and $M_l$ is the optical magnification of the lens.

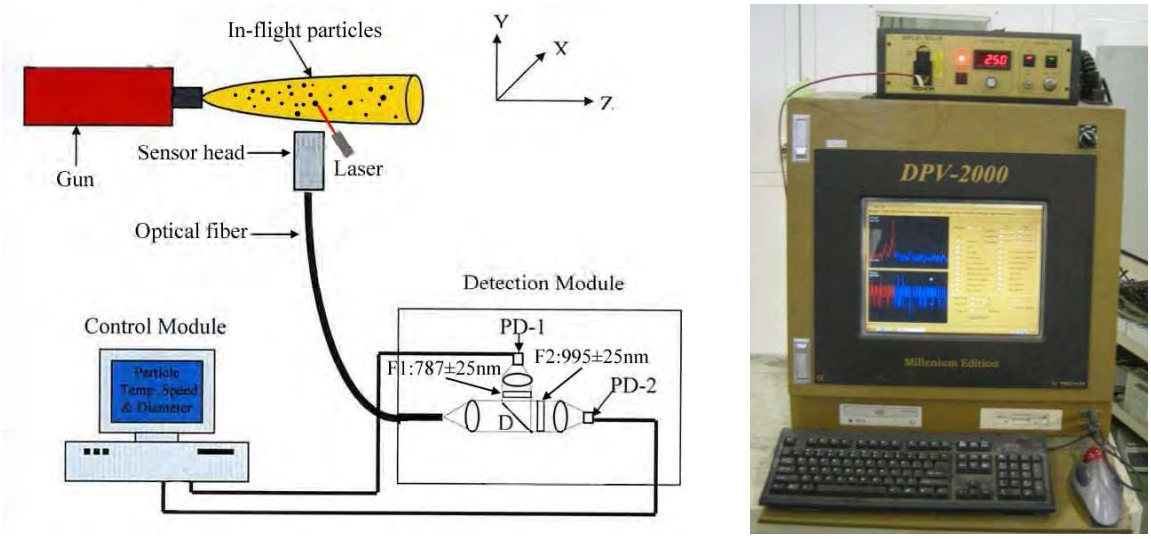


(a) (b)

Figure 2-3. (a) Schematic and (b) photograph of DPV-2000 system

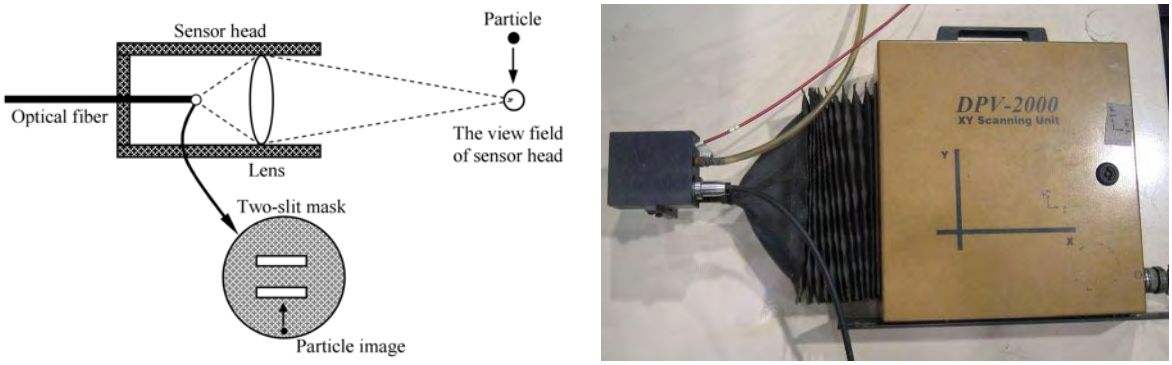


(a) (b)

Figure 2-4. (a) Schematic and (b) photograph of the optical sensor head

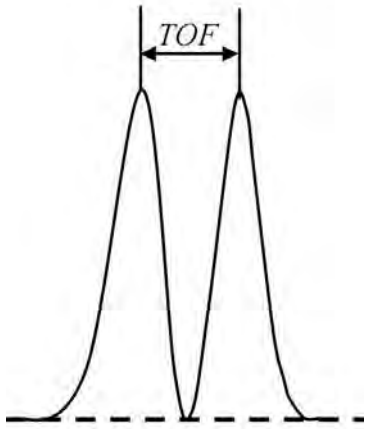


Figure 2-5. Illustration of two-peak signal

The particle temperature is measured using the technique of two-color pyrometry with two monochromatic signals from the two-color filtering channels. The surface temperature of the particles, $T_p$, is measured based on Planck's radiation law. The melted particles are assumed to be gray body emitters so they their emissivities at different wavelengths are similar. Therefore, $T_p$ is defined as [17].

$$T_p = \frac{c_2(\lambda_1 - \lambda_2)}{\lambda_1 \lambda_2} \left[ \frac{1}{\ln \frac{E(\lambda_1)}{E(\lambda_2)} + 5 \ln \frac{\lambda_1}{\lambda_2}} \right] \qquad (Eq. 2-2)$$

where $c_2$ is Planck constant, $\lambda_1$ and $\lambda_2$ are the wavelengths that pass through the two-color filtering channels, and $E(\lambda_i)$ is the theoretical energy that a particle radiates at the corresponding wavelength.

The DPV-2000 system performs calculations based on the assumptions that melted particles are spherical and that the signal energy is proportional to the square of the particle diameter $D$ [15], which is defined as

$$D = \sqrt{\frac{E(\lambda_i)}{DC}} \qquad (Eq. 2-3)$$

where $DC$ is a coefficient used to calibrate measured values of diameter to the actual value.

### 2.3.3 Spray Watch system

The SprayWatch system from Oseir Ltd. (Tampere, Finland) is an imaging system used for quality control of industrial thermal spray processes. It employs a high-quality, fast-shutter CCD camera to obtain digital images of the spray. The system consists of a compact air-cooled camera head and an industrial PC, as shown in figure 2-6.

The algorithm identifies individual particles in images obtain with a short exposure time and measures their position, direction, and velocity. Simultaneously, the camera obtains another image using a longer exposure time to measure the average particle temperature in the spray. The particle temperatures are measured by two-color pyrometry, similar to the DPV-2000 system. An optical double-stripe filter is installed in the camera and partially covers the CCD detector. The spray is imaged on the CCD at two different wavelengths so that the lateral distribution of the average particle temperature in the spray can be calculated using calibration data [18–19].


Figure 2-6. Spray Watch system

### 2.3.4 Measurement of torch voltage and electrothermal efficiency of the plasma torch

To ascertain the fluctuation inside the torch, the torch voltage and electric current were measured by a two-channel digital storage oscilloscope (TDS-2022C, Tektronix Inc.). The oscilloscope has a maximum sampling frequency of 2 GHz. The torch voltage and current were simultaneously measured with sampling periods of 4 and 0.4 μs. The average torch voltage can be obtained from the time-dependent torch voltage to calculate the electrothermal efficiency. Table 2-1 lists the spray conditions in measurements of the torch voltage fluctuation.

Table 2-1. Spray conditions in the measurement of torch voltage.

| | |
|---|---|
| Argon flow rate (SLM) | 50 |
| Electrical Current (A) | 300, 400, 500, 600, 700, 800 |
| Powder gas flow rate (SLM) | 5 |
| Cooling water flow rate (l/min) | 22-24 |

The electrothermal efficiency of the plasma torch was determined from the measured torch voltage and current. Since the arc fluctuates inside the torch, the electrothermal efficiency of the torch varies with time. In the current study, the average electrothermal efficiency was measured. It is necessary to measure the arc current, the torch voltage, and the cooling water temperature to determine the electrothermal efficiency. Hence, a PC-based data acquisition system was utilized to record these parameters. Experiments were carried out under the same spray conditions listed in Table 2-1.

The electrothermal efficiency of the torch is calculated using

$$\eta(\%) = \frac{Q_{plasma}}{UI} \times 100\% \qquad (Eq. 2-4)$$

where $U$ is the torch voltage, $I$ is the operating current, and $Q_{plasma}$ is the total heat energy transferred to the plasma arc, which is calculated using

$$Q_{plasma} = U_p I - Q_{loss} = U_p I - \rho_w F_w C_p (T_2 - T_1) \qquad (Eq. 2-5)$$

where $Q_{loss}$ is the power dissipated by the cooling water, $U_p$ is the voltage between the two electrical cables where the cooling water temperature was measured, $\rho_w$ is the density, $F_w$ the flow rate, and $C_p$ specific heat of cooling water. $T_1$ and $T_2$ represent the cooling water temperature at the inlet and outlet in the electric cables, respectively. The difference between $U$ and $U_p$ is the voltage drop at the electrical cables.

In the current study, $U_p$ was measured at the cables connected to the starter and the cooling water temperature was also measured inside the electric cables connected the starter to measure the power dissipated by the cooling water.

### 2.3.5 Anode erosion measurement

To predict the position of the arc attachment on the anode inner surface, the erosion position was determined from images of the cross sections of used anodes. To accelerate the erosion rate, the spray conditions used for the anode erosion test differ slightly from those used in previous experiments because the auxiliary plasma gas of helium was injected and mixed with argon gas to increase the plasma voltage (see Table 2-2). A new

anode was employed to spray at the conditions lasting a specific time. And then, the anode was cut along its center line to observe its erosion situation.

### 2.3.6 In-flight particle temperature and velocity measurements

Commercially available oxide ceramic powders of PC.AT13T, supplied by Saint-Gobain Ceramic Materials Co. Ltd., were used to measure the in-flight particle temperature and velocity. The chemical composition of the powder is given in Table 2-3; it mainly consists of alumina and titania. Figure 2-7 shows the morphology of the powder; it has an irregular shape due to crushing. The powder size distribution was characterized using a laser diffraction particle size analyzer (Seishin Trading Co., Ltd., Kobe, Japan). Figure 2-8 shows the volume distribution of the diameter. The measured volume average diameter is about 31 μm.

Table 2-2. Operating conditions for anode erosion experiments.

| | |
|---|---|
| Argon flow rate (SLM) | 50 |
| Helium flow rate (SLM) | 20 |
| Electrical Current (A) | 750 |
| Powder gas flow rate (SLM) | 8 |
| Average torch voltage (V) | 40 |
| Cooling water flow rate (l/min) | 22-24 |

Table 2-3. Chemical composition of the powder

| Composition | $Al_2O_3$ | $TiO_2$ | CaO | $SiO_2$ | $Fe_2O_3$ | MgO |
|---|---|---|---|---|---|---|
| Ratio (%) | 84.32 | 14.10 | 0.14 | 1.10 | 0.10 | 0.24 |

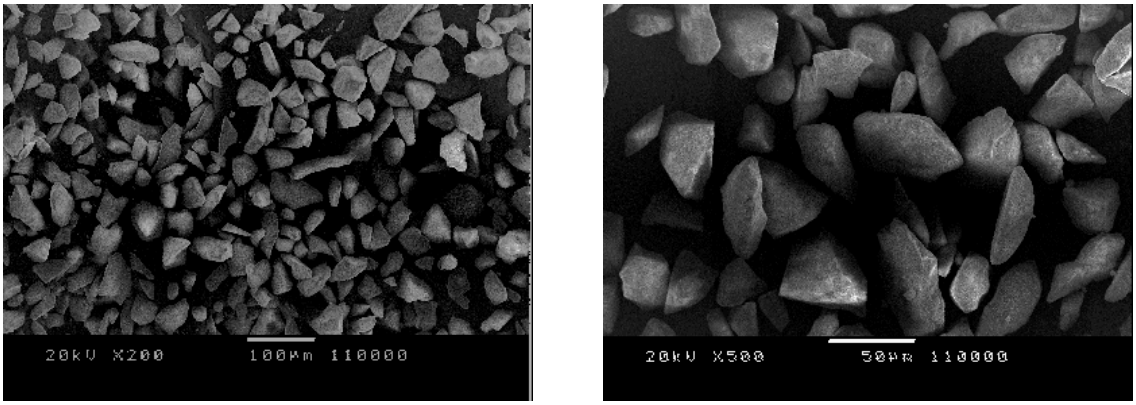


Figure 2-7. Morphology of PC.AT13T powder

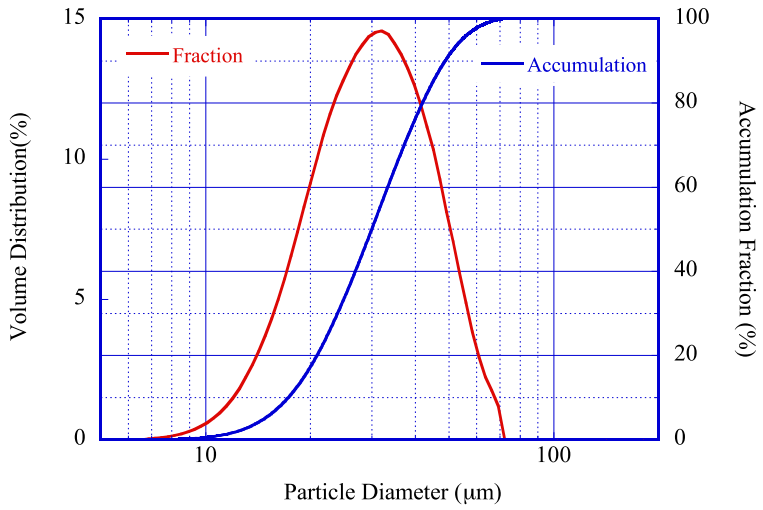


Figure 2-8. Diameter distributions of PC.AT13T powder

Figure 2-9 shows the sensor orientation for the measurement of the in-flight particle temperature and velocity. The field of view of the DPV-2000 sensor is determined by the two-slit photomask installed in the sensor head; in the present experiment it was 0.135×0.17 mm. The field of view of the SprayWatch system is determined by the CCD size; in the present experiment it was 23.28×26.84 mm. Although the DPV-2000 system has a smaller field of view than the SprayWatch system, the system was equipped with a two-axis electrical scanning unit motion controller to measure the parameters of particles with relatively large areas (see figure 2-4(b)). Table 2-4 lists the spray conditions used in

the current study. Argon gas with a flow rate of 50 SLM was employed as the plasma gas, the electrical current was 500 A, and the measurement distance from the torch exit was varied between 10 and 50 mm in an interval of 10 mm.

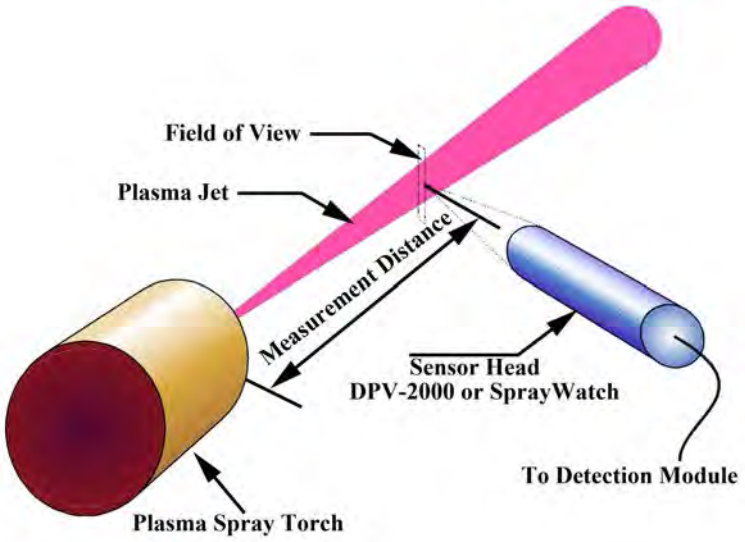


Figure 2-9. Sensors orientation

Table 2-4. Plasma spray conditions for the measurement of in-flight particle parameters.

| | |
|---|---|
| Argon flow rate (SLM) | 50 |
| Electrical Current (A) | 500 |
| Powder gas flow rate (SLM) | 9 |
| Cooling water flow rate (l/min) | 22-24 |
| Measurement distance (mm) | 10, 20, 30, 40, 50 |

## 2.4. Results and Discussion

### 2.4.1 Torch voltage and electrothermal efficiency of plasma spray torch

Figure 2-10 shows the time-dependent voltage and current measured by an oscilloscope with different sampling periods. With a sampling period of the order of milliseconds, the current fluctuates between 250 and 550 A when a current of 400 A is applied and it fluctuates between 600 and 1000 A when a current of 800 A is applied, as shown in figures 2-10(a) and (c). The current fluctuates with a frequency of about 300 Hz; this frequency is determined by the power supply. Three-phase AC power with a frequency of 50 Hz was used in the plasma spray system; the power supply frequency will be 300 Hz after simple rectification. Although the current fluctuates with a frequency of 300 Hz, the torch voltage fluctuates in a small range with no clear fluctuation frequency. The torch voltage fluctuates between 27 and 30 V when a current of 400 A is applied and it fluctuates between 24 and 26 V when a current of 800 A is applied, as shown in figures 2-10(a) and (c). When a higher sampling frequency of the order of microseconds is used, no clear fluctuation frequency is observed for any of the arc currents or voltage signals used, as shown in figures 2-10(b) and (d). The torch voltage appears to be nearly constant, whereas the arc current fluctuates over a large range. From the results of arc voltage, it can be predicted that the anodic arc root only moves in a small range on the anodic inner surface.

The average torch and starter voltage can be obtained from the signals measured by the oscilloscope (see figure 2-11). The difference between the torch and starter voltage is the voltage drop at the power cables. The torch voltage decreases slightly when the current is increased. There are two reasons for this reduction in the torch voltage. One is the electrical conductivity of plasma gas decreases as the current increases, so that the voltage drop on the plasma column decreases. Another reason is that the sheath voltage decreases with increasing current density in the electrodes [20–21]. The starter voltage remains almost constant, whereas the torch voltage decreases with increasing applied current; this

is attributed to the voltage drop at the power cables increasing, as shown in figure 2-11.

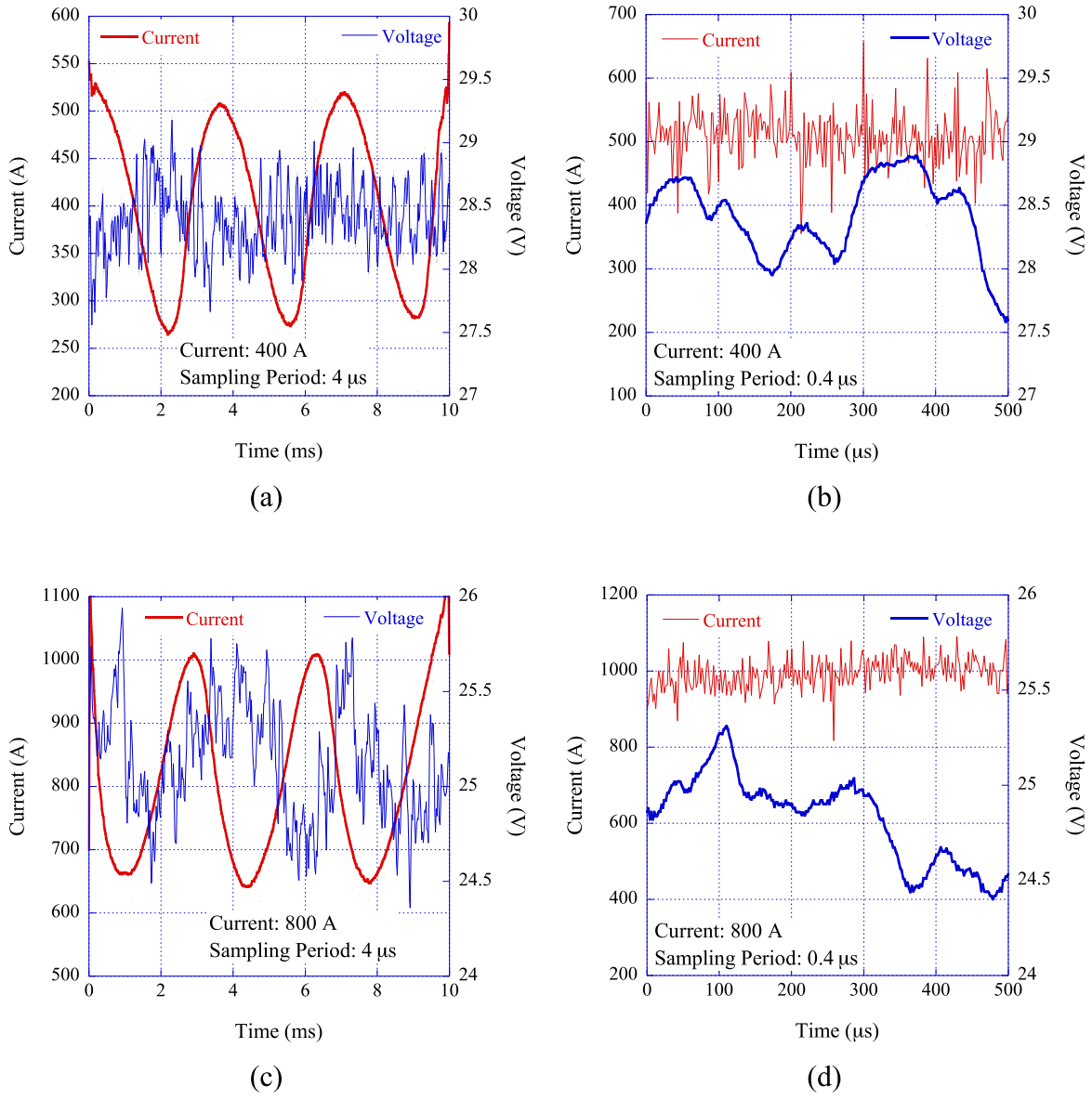


Figure 2-10. Time-dependent torch voltage and current

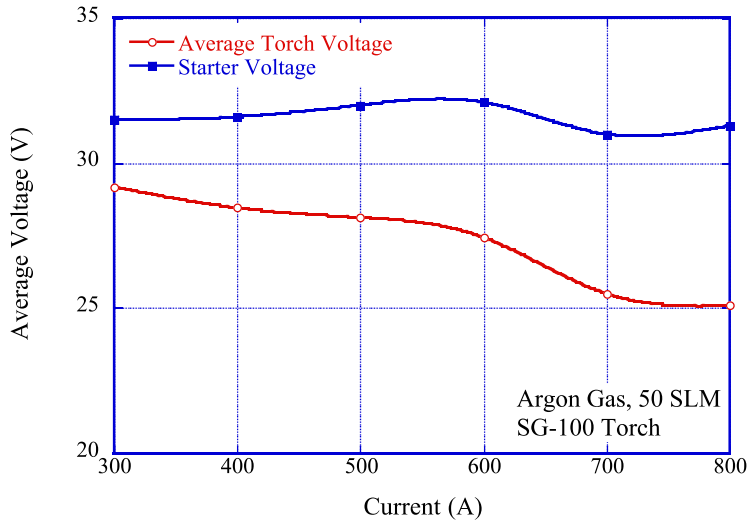


Figure 2-11. Measured torch and starter voltage

Figure 2-12 shows the heat energy transferred to the plasma arc, which was determined from the electrical energy calculated using Eq. 2-5. It reveals that the energy transferred to the plasma increases with increasing applied current. Therefore, It is thus necessary to apply a higher current to increase the plasma gas temperature in order to prepare high-quality coatings for the refractory materials such as high-melting-point metals or ceramics.

The efficiency of the plasma torch was calculated from the measured average voltage, current, and energy transferred to the plasma arc as shown in figure 2-13. The electrothermal efficiency of the torch is nearly 50% and it increases slightly with increasing applied current. When the energy loss due to heating in the power cables is considered, the efficiency of the power supply is about 40% and it remains almost constant when the applied current is varied. Although the energy loss in the power cables increases with increasing applied current, this is compensated by the increase in the electrothermal efficiency of the plasma torch; consequently, the heat efficiency of the power supply remains almost constant.

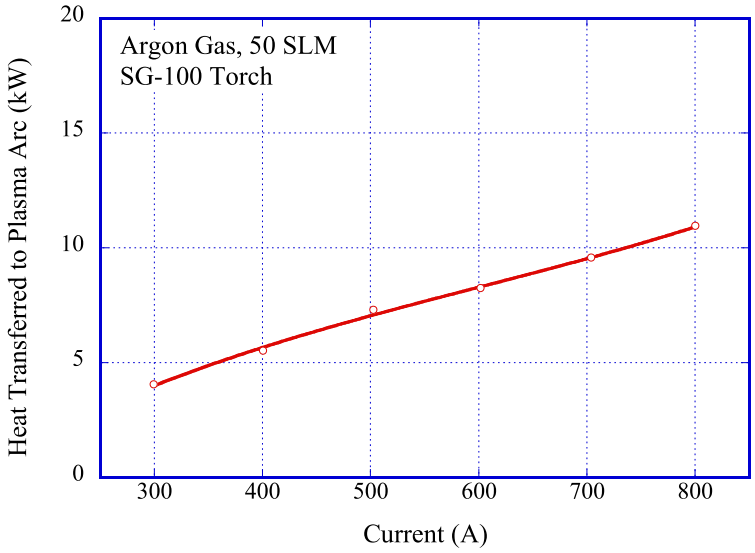


Figure 2-12. Heat transferred to plasma arc

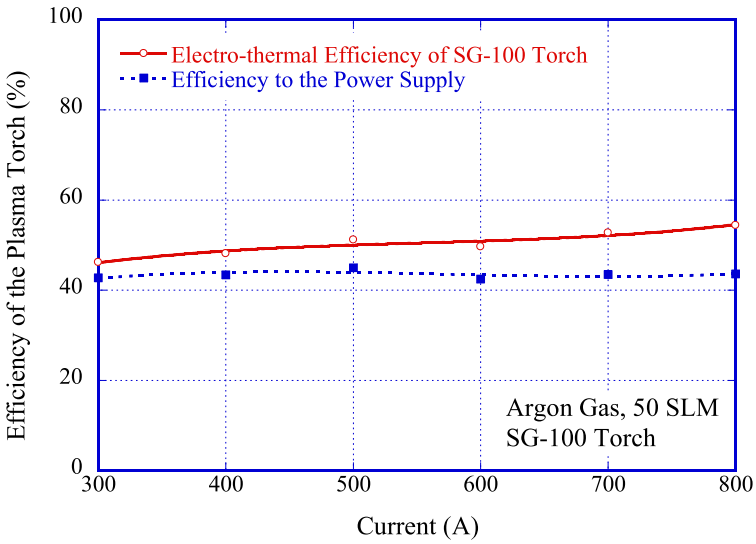


Figure 2-13. Electrothermal efficiency of SG-100 torch

### 2.4.2 Anode erosion of plasma spray torch

After measuring the torch voltage, the anode erosion was observed to ascertain the arc root position. Figure 2-14 shows cross-sectional photographs of the eroded anodes. The anode shown in figure 2-14(a) was used for 30 h and the internal surface of the anode was

slightly eroded. The anode became severely eroded after extended use, as shown in figure 2-14(b). The anode appears to be always eroded close to the corner of the internal surface of the anode. Extended usage only increases the eroded region. This indicates that the arc length varies little within an annular location; consequently, the torch voltage varies little over time (see figure 2-10).

### 2.4.3 Plasma jet photographs taken by SprayWatch system

After performing measurements of the plasma arc inside the torch, some tests were carried out to measure the behavior of the plasma jets. First, the plasma jet was observed by the SprayWatch system with a special filter in front of the CCD camera to protect it from the intense plasma arc. Figure 2-15 shows photographs of the plasma jet obtained by the SprayWatch system with a time interval of 1 s.

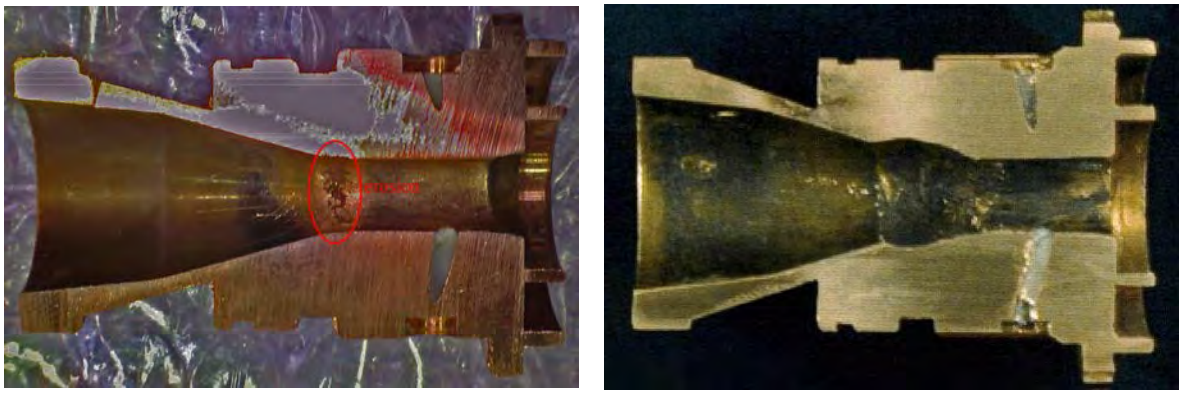

(a) Slight erosion for relatively short usage (b) Severe erosion for relatively long usage

Figure 2-14. Eroded anode

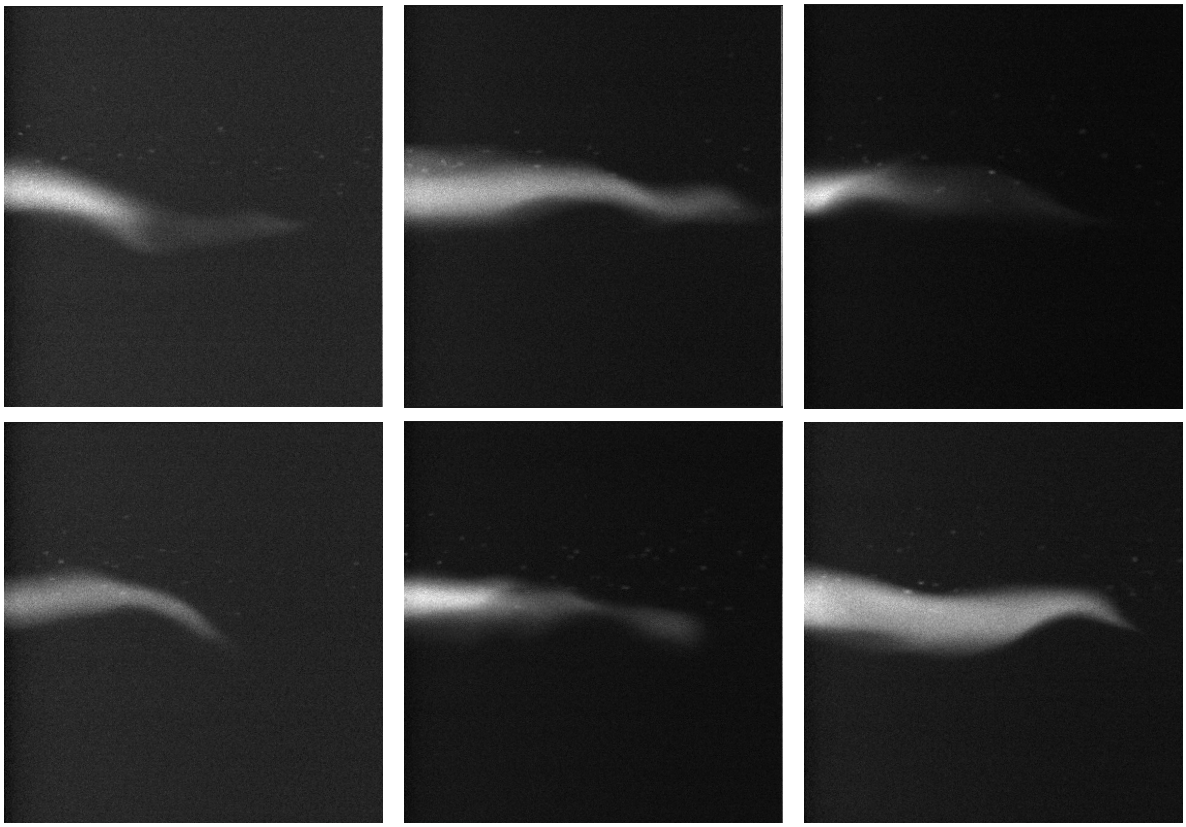

Figure 2-15. Photographs of plasma jet taken by SprayWatch system with a time interval of 1 s

The photographs reveal that the length and direction of the plasma jet vary with time. Thus, the plasma jet fluctuates with time.

### 2.4.4 Particle temperature and velocity measured by SprayWatch and DPV-2000 systems

As the plasma jet fluctuates, the in-flight particle parameters are also expected to fluctuate. However, it is difficult to measure fluctuations in the in-flight particle parameters using the DPV-2000 and SprayWatch systems, since they can measure only the steady-state temperature and velocity. The high-intensity background emitted by the plasma jet makes it difficult to detect the radiation emitted by in-flight particles with sensors, especially near the torch outlet [22]. Figure 2-16 shows the particle numbers

detected by DPV-2000 and SprayWatch systems over 5 s. It reveals that the DPV-2000 and SprayWatch systems can detect in-flight particles 20 and 30 mm from the torch outlet, respectively. The background appears affect the DPV-2000 system little at distances from the torch outlet greater than 20 mm. The particle number detected by DPV-2000 decreases when the spray distance from the torch outlet is increased to 30 mm due to the divergence of the in-flight particles. However, the background has some effect on the SprayWatch system for spray distances up to 50 mm; since the effect of the background decreases with increasing spray distance, the number of particles detected gradually increases with increasing spray distance. The CCD camera of SprayWatch system appears to have a lower accuracy than the two-slit photomask sensor of the DPV-2000 system.

The DPV-2000 system can simultaneously measure the particle velocity and temperature, whereas the SprayWatch system can measure only the in-flight particle velocity (it cannot measure the particle temperature). However, the SprayWatch system can integrate the intensity from all the particles produced by a single flash so that the average particle temperature can be deduced. Figure 2-17 shows the particle velocity distributions measured by the SprayWatch and DPV-2000 systems. For both systems, the measured in-flight particle velocities ranged from 100 to 300 m/s.

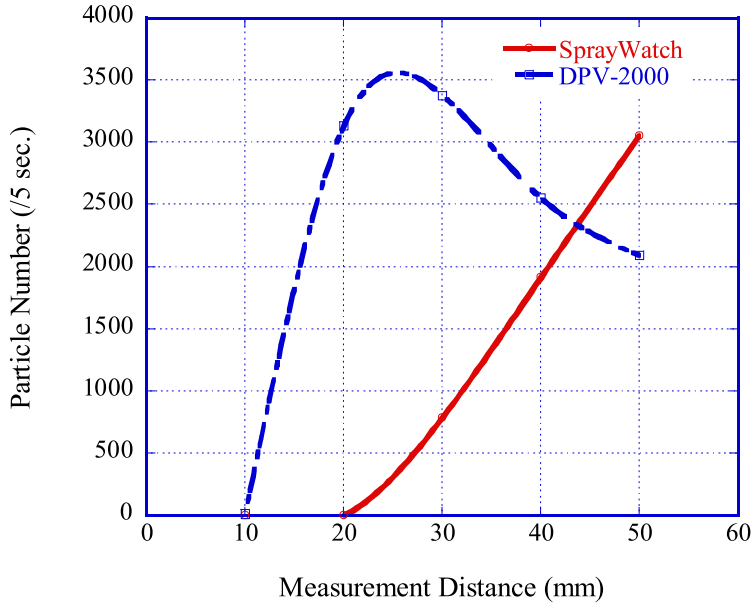


Figure 2-16. Particle numbers detected by DPV-2000 and SprayWatch systems

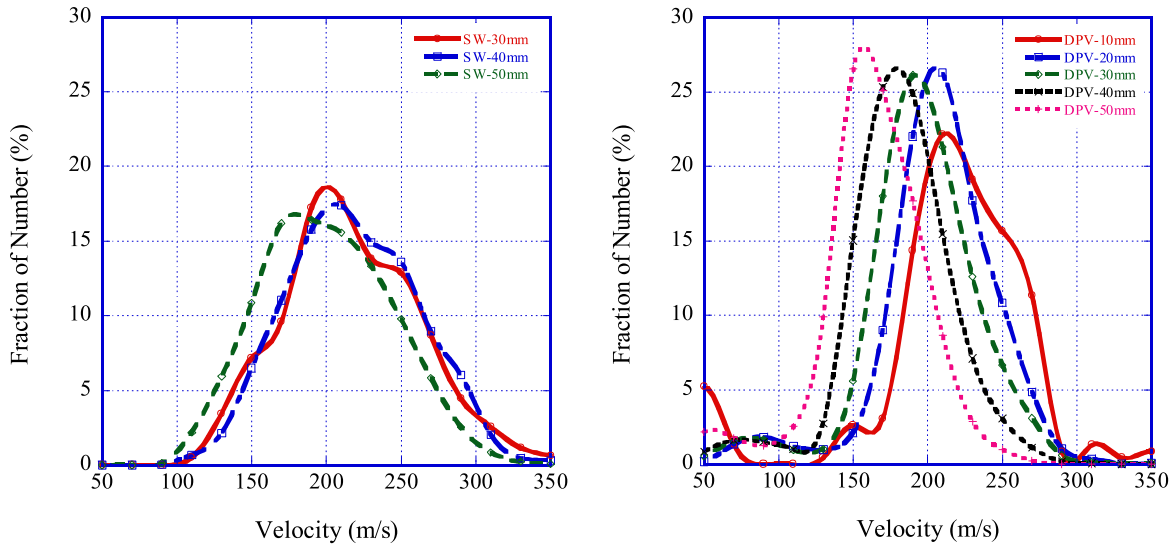


(a) (b)

Figure 2-17. In-flight velocity distributions measured by (a) SprayWatch and (b) DPV-2000 systems.

Figure 2-18 shows the average particle temperature and velocity measured by the SprayWatch and DPV-2000 systems. The measured particle temperature increases as the

spray distance is increased to 30 mm for the results measured by the DPV-2000 system; the particle temperature decreases when the spray distance is further increased. The particle temperature measured by the SprayWatch system is similar to that measured by the DPV-2000 system, but it shows no obvious correlation with spray distance. This is due to the background from the high intensity arc, since the sensor is unable to detect particles in regions with high backgrounds. The particle velocities measured by the two systems show the same tendency with spray distance: they both decrease with increasing spray distance. The velocity measured by the SprayWatch system is higher than that measured by the DPV-2000 system. The difference between the two systems is caused by the effect of the background due to the arc and by limited resolution of the CCD camera in the SprayWatch system.

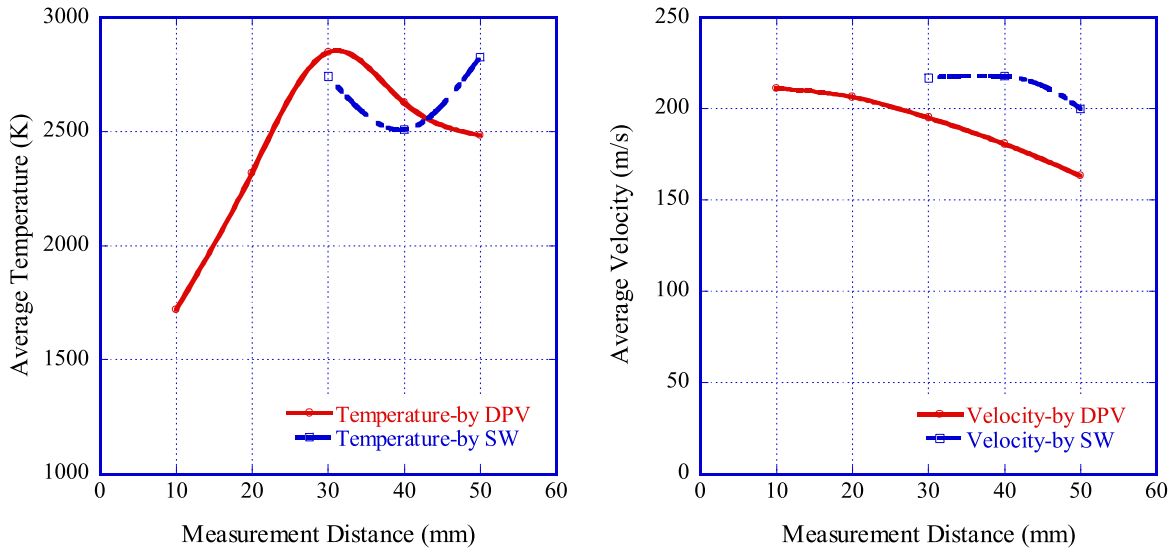


(a) (b)

Figure 2-18. (a) Average particle temperature and (b) velocity measured by SprayWatch and DPV-2000 systems.

## References

[1]. Ramasamy R. and Selvarajan V., Current-voltage characteristics of a non-transferred plasma spray torch, Eur. Phys. J. D 8, 125–129 (2000).

[2]. Coudert J. F., planche M. P., fauchais P., Characterization of DC Plasma Torch Voltage Fluctuations, Plasma Chemistry and Plasma Processing, Vol. 16, No. 1, 1996 (Supplement), 211s-227s.

[3]. Vysohlid Martin, Arc Voltage Fluctuations in a Plasma Torch, M.Sc. Thesis, University of Minnesota, 2003.

[4]. Dorier J.-L., Gindrat M., Hollenstein C., Salito A., Loch M. and Barbezat G., Time-resolved imaging of anodic arc root behavior during fluctuations of a DC plasma spraying torch, IEEE Transactions on Plasma Science, vol. 29, issue 3, 2001, 494-501.

[5]. Duan Z. and Heberlein J., Arc Instabilities in a Plasma Spray Torch, Journal of Thermal Spray Technology, Volume 11(1) March 2002, 44-51.

[6]. Huang He-Ji, Pan Wen-Xia, Wu Cheng-Kang, Arc Root Motions in an Argon–Hydrogen Direct-Current Plasma Torch at Reduced Pressure, Chin. Phys. Lett., Vol. 25,No. 11 (2008), 4058-4060.

[7]. Jahn R. E., Temperature distribution and thermal efficiency of low power arc-heated plasma jets, Br. J. Appl. Phys. 14, 585, 1963.

[8]. Capetti A. and Pfender E., Probe Measurements in Argon Plasma Jets Operated in Ambient Argon, Plasma Chemistry and Plasma Processing, Vol. 9, No. 2, 1989.

[9]. J. F. Coudert, M. P. Planch and P. Fauchais, Velocity Measurement of DC Plasma Jets Based on Arc Root Fluctuations, Plasma Chemistry and Plasma Processing, Volume 15, Number 1, 47-70, 1995.

[10]. Planche M. P., Coudert J. F. and Fauchais P., Velocity Measurements for Arc Jets Produced by a DC Plasma Spray Torch, Plasma Chemistry and Plasma Processing,

Vol. 18, No. 2, 1998.

[11]. Duan Z., Beall L., Schein J., Heberlein J., and Stachowicz M., Diagnostics and Modeling of an Argon/Helium Plasma Spray Process, Journal of Thermal Spray Technology, Volume 9(2), 225-234, June 2000.

[12]. Bahbou M.F. and Nylen P., On-Line Measurement of Plasma-Sprayed Ni-Particles during Impact on a Ti-Surface:Influence of Surface Oxidation, Journal of Thermal Spray Technology, Volume 16(4), 506–511, December 2007.

[13]. Goutier S., Nogues-Delbos E., Vardelle M. and Fauchais P., Particle Temperature Fluctuations in Plasma Spraying, Journal of Thermal Spray Technology, Volume 17(5-6), 895–901, Mid-December 2008.

[14]. Moreau C., P. Gougeon, M. Lamontagne, G. Vaudreuil and P. Cielo, On-line Control of the Plasma Spraying Process by Monitoring the Temperature, Velocity and Trajectory of In-flight Particles, Thermal Spray Industrial Applications, C.C. Berndt and S. Sampath, Ed., June 20-24, 1994 (Boston, MA), ASM International, 1994, p 431-437.

[15]. Pouliot L., DPV-2000 Reference Manual, Rev. 5.0, TECNAR Automation Ltd, Canda, 1999, p 7.

[16]. Li C-J., T. Wu, C. X. Li, and B. Sun, Effect of Spray Particle Trajectory on the Measurement Signal of Particle Parameters Based on Thermal Radiation, Journal of Thermal Spray Technology, V12 (1), 2003, ASM International, p 80-94.

[17]. Khan M.A., C. Allemand, and T.W. Eagar, “Non-Contact True Temperature Measurements for Process Diagnostics”, Proc. of materials research symposium on process diagnostics: Materials, Combustion, Fusion, 117, 119, 1988.

[18]. Hämäläinen E., J. Vattulainen, T. Alahautala, R. Hernberg, P. Vuoristo and T. Mäntylä, Imaging Diagnostics in Thermal Spraying-SprayWatch System, Thermal Spray 2000: Surface Engineering via Applied Research (ASM International), p 79 – 83, 2000.

[19]. Hämäläinen E., Kriikka N. and Barbezat G., On-line Optical Diagnostics of a Rotating Internal Diameter Plasma Spray Gun Used for Coating of Cylinder Bores in Automotive Industry, Thermal Spray 2003: Advancing the Science & Applying the Technology, (Ed.) C. Moreau and B. Marple, Published by ASM International, Materials Park, Ohio, USA, 2003.

[20]. Benilov M. S., Understanding and modelling plasma-electrode interaction in high-pressure arc discharges: a review, J. Phys. D: Appl. Phys. 41 (2008), p1-30

[21]. Zhou X. and J. Heberlein, Analysis of the arc-cathode interaction of free-burning arcs, Plasma Source Sci. Technol. 3 (1994), p564-574

[22]. Gougeon P. and C. Moreau, In-flight particle surface temperature measurement: Influence of the plasma light scattered by the particles, Journal of Thermal Spray Technology, Volume 2, Number 3, 229-233 (1993)

# Chapter 3
# Simulation of Arc Plasma Properties in a Plasma Spray Torch

## 3.1 Introduction

In the previous chapter, the plasma torch voltage and current and particle parameters in the plasma jets were measured to investigate plasma arcs in plasma torches and plasma jets outside plasma torches. In this chapter, a plasma arc in a plasma torch is numerically analyzed. It is extremely challenging to model DC arc plasma torches because they exhibit highly nonlinear plasma flow and high property gradients. In this study, three LTE models were used to model plasma flow in a plasma torch and the results obtained were compared with measurement results.

## 3.2 Background of Plasma Arc Simulation

As mentioned in Chapter 2, it is difficult to experimentally investigate arc behavior inside plasma torches. Fortunately, numerical calculations can be used to investigate arc behavior in plasma torches. Despite its complexity, many studies in the past several decades have numerically simulated the characteristics of DC arc plasma torches. Numerical simulations of plasma arcs are much more attractive than experimental studies because they do not require expensive experimental equipment and they have benefited from the development of high-speed computers.

In the initial stages of simulating plasma arcs, two-dimensional (2D) axisymmetric steady-state modeling techniques based on the LTE assumption were employed to predict the heat transfer and flow patterns inside a plasma torch. The behavior of an arc operated

in the non-transferred mode with a conical cathode and a nozzle anode was studied by applying general 2D conservation equations and auxiliary relations in the simulation of arc channel flow. The gas velocity and temperature inside a plasma torch were calculated and the position of the anode arc root in a plasma torch was predicted by the Steenbeck minimum principle [1]. Favalli and Szente [2] developed a computer code to calculate temperature and velocity profiles for a non-transferred plasma torch and jet using a 2D steady-state model. However, the arc voltage of a torch in the turbulent regime predicted by 2D axisymmetric steady-state models is much higher than the measured value; in addition, the predicted axial location of the arc attachment at the anode surface is much farther downstream than that observed in experiments [3].

The rapid development of computers made it feasible to calculate heat transfer and fluid flow for a 3D thermal plasma torch. The most frequently used models for simulating plasma spray torches are based on the LTE approximation. They regard the plasma flow as a property-varying electromagnetic reactive fluid in chemical equilibrium, where the internal energy of the fluid is characterized by a single parameter, the gas temperature. Selvan et al. [4–5] developed a 3D steady-state LTE model to describe the temperature and velocity distributions in a DC non-transferred plasma torch. They also discussed the arc core radius and arc length. The torch power and efficiency predicted by the model were in good agreement experimentally measured values. However, the model overestimated the plasma gas temperature near the arc root due to the assumption that the electric current is transferred to the anode only through a fixed arc root. Klinger et al. [6] also developed a 3D steady-state LTE model of a plasma arc in a DC plasma torch. However, the arc root position was determined arbitrarily. Li et al. [3, 7] discussed the axial position of the anode arc root on the anode surface using the Steenbeck's minimum principle in a 3D steady-state model for a DC non-transferred arc plasma torch. They showed that the position of the anode arc root attachment and the arc shape predicted by employing the Steenbeck minimum principle are reasonably consistent with those observed

experimentally. Using this principle, they also analyzed the characteristics of heat transfer and flow patterns in both the plasma torch and plasma jet regions. Moreover, they also predicted the corresponding heating histories and 3D trajectories of nickel powders based on the calculated 3D temperature and flow field.

After 3D steady-state LTE models had been developed that could accurately predict the arc root position and heat and flow patterns in a plasma torch, time-dependent 3D models were developed to model the fluctuations of plasma arcs and jets. Baudry et al. [8] and Moreau et al. [9] developed a time-dependent 3D LTE model to model the fluctuations in a plasma arc in a plasma torch. They showed that the model accurately predicted the arc behavior and voltage fluctuations for an arc operated in the restrike mode. However, it still overestimated the length of the arc attachment at the anode wall. To improve the prediction of arc behavior in a plasma torch, Trelles et al. [10–13] developed a reattachment model to simulate the fluctuations of a plasma arc. They specified a criterion for determining the position where an attachment occurs by defining a breakdown electric field. The calculated peak frequencies of the voltage signal, arc lengths, and anode spot sizes agreed reasonably well with experimental observations. However, the calculated total voltage drop exceeded experimentally measured values due to the LTE assumption giving a poorly defined cold boundary layer around the arc. To clarify the importance of thermal non-equilibrium effects inside the torch, particularly in the anode attachment region, Trelles et al. developed a two-temperature NLTE model to simulate a non-transferred arc plasma torch. The results obtained with the NLTE model differed significantly from those obtained with the LTE model, especially the arc dynamics, the total voltage drop, and the outlet temperatures and velocities. The NLTE model results show improved agreement with experimental observations [14]. However, it is extremely difficult to solve the NLTE model because two-temperature chemical equilibrium needs to be considered compared with the LTE model.

Almost all previous simulations of plasma arcs are based on the LTE assumption. The

NLTE model has begun to be used to model plasma arcs inside plasma torches, but it has a high computational cost due to its complexity. This motivated us to develop a simpler model that is similar to the LTE model, but which has a high accuracy, similar to that of the NLTE model. In the present study, the LTE assumption was assumed to be valid to reduce the computational cost. Due to the LTE assumption in the conventional LTE mode, the electron temperature is equal to heavy particle temperature, which is low near the electrodes, especially near the anode surface. Hence, the equilibrium electrical conductivity, being a function of the electron temperature, is extremely low, which reduces the electric current in the electrodes. To alleviate this situation, some additional assumptions are required to give a high electrical conductivity near the electrodes. To improve the calculation accuracy, a novel LTE model was developed in which the electrical conductivity of a plasma gas was determined from the nominal electron temperature. Two conventional LTE models were also employed in the present study to verify the accuracy of the novel LTE model. One conventional model is very simple: it sets an artificially high electrical conductivity near the electrodes. The other conventional LTE model is a model developed by Trelles et al. [10–12], known as the reattachment model. Using these three LTE models, the plasma gas temperature and velocity distributions in a DC plasma torch were calculated and the distributions of electrical potential and current density were also investigated. The calculated results were compared with experimentally measured results.

## 3.3 Modeling of Plasma Arc in a Plasma Spray Torch

### 3.3.1 Assumptions

The model developed in this study is based on the following main assumptions for simulating heat transfer and flow patterns in a plasma torch:

(1) The continuum assumption is valid so that the plasma can be considered a compressible gas in the LTE state.

(2) The plasma is optically thin.

(3) Gravitational effects and viscous dissipation are negligible.

(4) The induced electric field is negligible compared with the applied electric field strength the plasma arc region.

(5) The gas pressure variation inside the torch is so small that the effects of pressure on the thermodynamic and transport properties of the plasma gas are negligible. Due to the LTE assumption, the thermodynamic and transport properties of the plasma gas (e.g., specific heat, dynamic viscosity, thermal conductivity, and volumetric net radiation losses) are determined by the gas temperature, with the exception of the electrical conductivity of the plasma gas.

### 3.3.2 Arc plasma models

Due to the LTE assumption, the electron temperature is equal to the heavy particle temperature, which is low near the electrodes, especially near the anode surface. Hence, the equilibrium electrical conductivity is extremely low (less than $10^{-2}$ S/m), which limits the flow of electric current though the electrodes. Three methods were employed to alleviate this in the present study.

**1) Model 1: Electrical conductivity near the electrode interface is artificially set**

This model is the simplest one in conventional LTE models. In this model, the electrical conductivity is essentially determined by the gas temperature, but the electrical conductivity in the vicinity of the electrode interface was set artificially high to overcome the low electrical conductivity near the electrode interface. A new attachment will form if some regions of the arc are sufficiently close to the anode surface, as shown in figure 3-1. In this study, the region with a high electrical conductivity in front of the anode is less than 0.1 mm thick and the specified electrical conductivity is $10^4$ S/m.

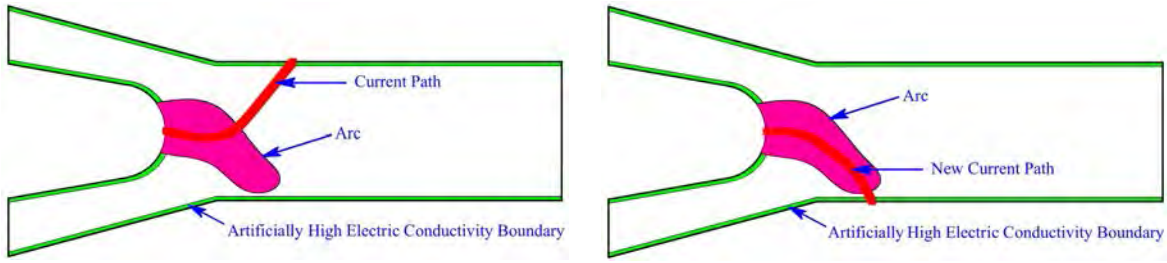


(a) (b)

Figure 3-1. Arc reattachment model in which a high electrical conductivity is artificially set at the electrode interface.

**2) Model 2: Electrical conductivity of the current flow path is artificially set based on the breakdown electric field**

The second model was developed by Trelles et al. [10–12]. Since it is a conventional LTE model, the electrical conductivity is basically determined by the gas temperature except in some specific region where an electric conducting path is artificially specified. This mode is illustrated in figure 3-2. As the arc moves downstream, the local electric field will somewhere exceed the breakdown electric field $E_b$ (see figure 3-2(a)). A high electrical conductivity channel is then specified, which traverses the maximum electric field region and travels vertically to the anode surface (see figure 3-2(b)). The electric current will pass through the channel and a new attachment will form (see figure 3-2(c)). Finally, the old attachment disappears and the electric current will only pass through the new electric current path (see figure 3-2(d)).

In this study, the breakdown electric field $E_b$ was set to $10^5$ V/m. The electrical conductivity in the channel is modified according to:

$$\sigma = \max(\sigma_{eq}, \sigma_b) \qquad (Eq. 3-1)$$

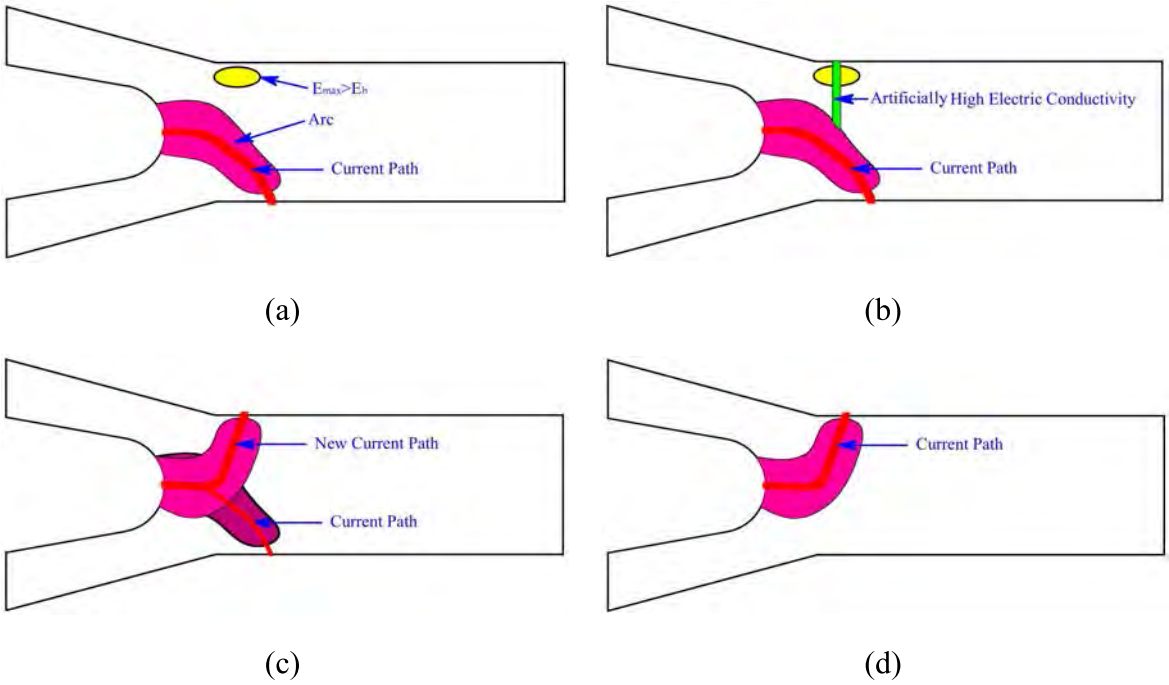


Figure 3-2. Arc reattachment model modified by a critical electric field.

where $\sigma_{eq}$ is the equilibrium electrical conductivity of the plasma and $\sigma_b$ is the electrical conductivity that characterizes the breakdown process, which is assumed to be of the form [11]:

$$\sigma_b = \sigma_{b0}\exp\left(-\beta_b\left(\frac{r_b}{R_b}\right)^{n_b}\right) \qquad (Eq.3-2)$$

where $r_b$ is the distance of the applied position from the center line of the cylindrical conducting channel. The parameters $R_b$, $\beta_b$, and $n_b$ define the shape of the $\sigma_b$ profile. The following values were used in the present study: $R_b$=1.25 mm, $\beta_b$=6, $n_b$=4 and $\sigma_{b0}$=$10^4$ S/m. Figure 3-3 shows the profile of $\sigma_b$. The electrical conductivity in the cylindrical channel will maintain $\sigma_b$ in the simulation until the temperature at 0.15 mm from the anode exceeds 9000 K in the cylindrical channel, since the electrical current path will maintain itself even when the electrical conductivity in the channel is not set artificially high.

**3) Model 3: Electrical conductivity determined by a nominal electron temperature**

To improve the calculation accuracy without increasing the computational cost, a novel LTE model was developed. In this model, the electrical conductivity of the plasma gas is determined by the nominal electron temperature rather than the gas temperature. Only considering the energy balance of electron that gains from the electrical field and loses to the heavy particles via collisions, the nominal electron temperature was put forward, which was derived from the gas temperature, corrected by the electric field strength.

As Porytskyy reported [15–16], for a weakly ionized gaseous medium, equilibrium between electrons and a mixture of atomic gases occurs because of the effect of the electric field on the electrons and the collisions between the electron and the heavy particles. Therefore, the nominal electron temperature can be calculated from the following equation [17–18]:

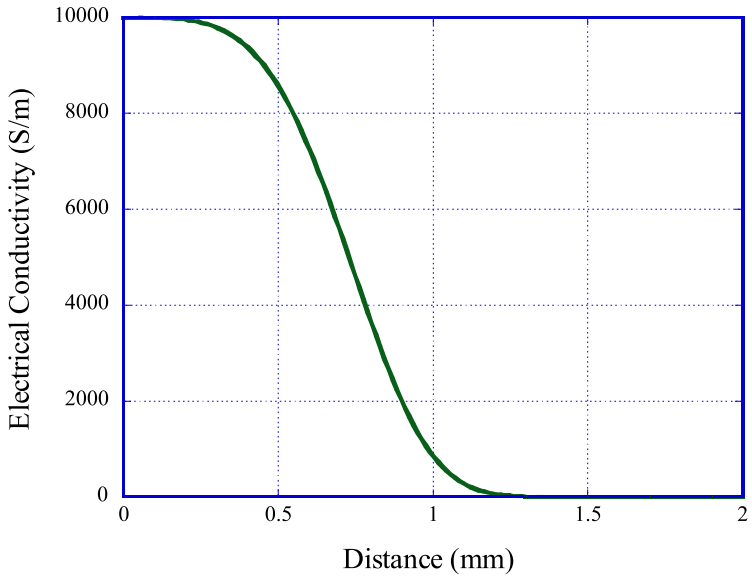


Figure 3-3. Profile of artificial electrical conductivity channel

$$\sigma|E|^2 = 3k(T_e - T)\frac{m_e}{m_h} n_e \upsilon_{eh} \qquad (Eq.3-3)$$

$$\upsilon_{eh} = \sum_k n_k \, Q_{ek} V_e \qquad (Eq.3-4)$$

where $\sigma$ is the electrical conductivity, $E$ is the electric field, $k$ is the Boltzmann constant, $T_e$ is the nominal electron temperature, $T$ is the plasma gas temperature, $m_h$ is the mass of a heavy particle, $m_e$ is the electron mass, $n_e$ is the electron number density, $\upsilon_{eh}$ is the electron–heavy particle collision frequency, $n_k$ is the number density of heavy particles (both atoms and ions), $Q_{ek}$ is the electron–heavy particle collision cross-section, and $V_e$ is the average electron thermal velocity. For argon gas, the collision cross-section $Q_{ek}$ is given by the following empirical formulas [19–21].

The electron–atom collision cross-section is given by:

$$Q_{en} = \begin{matrix} (0.713 - 4.5\times10^{-4}T_e + 1.5\times10^{-7}T_e^2)\times10^{-20} & (T_e \le 3000\ K) \\ (-0.488 + 3.96\times10^{-4}T_e)\times10^{-20} & (T_e > 3000\ K) \end{matrix} \qquad (Eq.3-5)$$

The electron–ion collision cross-section is given by:

$$Q_{ei} = \frac{e^4 \ln\Lambda}{24\pi(\epsilon_0 k T_e)^2} \qquad (Eq.3-6)$$

where $\ln\Lambda$ is the Spitzer logarithm, which is given by:

$$\Lambda = \frac{12\pi(\epsilon_0 k T_e)^{3/2}}{e^3 n_e^{1/2}} \qquad (Eq.3-7)$$

where $\epsilon_0$ is the vacuum permittivity ($\approx 8.854\times 10^{-12}$ F/m).

The problem of the low electrical conductivity in the vicinity of the electrodes can be solved by using the proposed nominal electron temperature to determine the electrical conductivity of the plasma gas.

### 3.3.3 Governing equations

Based on the above assumptions, the governing equations for a 3D time-dependent flow of arc plasma can be written as follows:

Conservation of mass:

$$\frac{\partial \rho}{\partial t} + \nabla \cdot \left(\rho \vec{V}\right) = 0 \qquad (Eq. 3-8)$$

Conservation of momentum:

$$\rho\left(\frac{\partial \vec{V}}{\partial t} + \vec{V}.\nabla\vec{V}\right) = \vec{j}\times\vec{B} - \nabla\left[P + \frac{2}{3}\mu\left(\nabla \cdot \vec{V}\right)\right] + 2\nabla \cdot \left(\mu\overleftrightarrow{S}\right) \qquad (Eq. 3-9)$$

Conservation of energy:

$$\rho c_p\left(\frac{\partial T}{\partial t} + \vec{V}.\nabla T\right) - \frac{DP}{Dt} = \vec{j}.\vec{E} - S_r + \nabla \cdot (\lambda \nabla T) \qquad (Eq. 3-10)$$

Maxwell equations:

$$\nabla \cdot (-\sigma \nabla \emptyset) = 0 \qquad (Eq. 3-11)$$

$$\vec{E} = -\nabla \emptyset \qquad (Eq. 3-12)$$

$$\Delta \vec{A} = -\mu_0 \vec{j} \qquad (Eq. 3-13)$$

$$\vec{B} = \nabla \times \vec{A} \qquad (Eq. 3-14)$$

Ohm's law:

$$\vec{j} = \sigma \vec{E} \qquad (Eq. 3-15)$$

where $\rho$ is the gas mass density, $t$ is time, $\vec{V}$ is the gas velocity, $\vec{j}$ is the electric current density vector, $\vec{B}$ is the magnetic induction vector, $P$ is the gas pressure, $\mu$ is the dynamic viscosity, $\overleftrightarrow{S}$ is the strain rate tensor, $c_p$ is the specific heat at constant pressure, $T$ is the gas temperature, $\vec{E}$ is the electric field, $S_r$ is the net volumetric radiation losses, $\lambda$ is the thermal conductivity of the gas, $\sigma$ is the electrical conductivity, $\emptyset$ is the electric potential, $\vec{A}$ is the magnetic vector potential, and $\mu_0$ is the permeability of free space..

### 3.3.4 Plasma gas compositions

Plasma gas is assumed to be in chemical equilibrium; therefore, according to the

assumptions in section 3.3.1, its composition is determined by the mass action law (minimization of the Gibbs free energy), the quasi-neutrality condition, and Dalton's law of partial pressures [22]. Considering the gas temperature of the plasma spray process, argon gas will primarily consist of four species in this study: argon atoms, ions, double ions, and electrons (Ar, $Ar^+$, $Ar^{++}$, and $e^-$). The equilibrium equations for $Ar^+$ and $Ar^{++}$ are:

$$Ar \leftrightharpoons Ar^+ + e - \varepsilon_1 \qquad (Eq. 3-16)$$

$$Ar^+ \leftrightharpoons Ar^{++} + e - \varepsilon_2 \qquad (Eq. 3-17)$$

where $\varepsilon_1$ and $\varepsilon_2$ are the ionization potentials of $Ar^+$ and $Ar^{++}$, respectively. If all the particles are in equilibrium, Saha equations can be derived from the minimization of Gibbs free energy law [15, 23]. The Saha equations using in this study are:

$$\frac{n_i n_e}{n_{i-1}} = \frac{Q_e Q_i}{Q_{i-1}} \left(\frac{2\pi m_e kT}{h^2}\right)^{3/2} \exp\left(\frac{-e\varepsilon_i}{kT}\right); i = 1, 2 \qquad (Eq. 3-18)$$

where the subscript $i$ includes all the ionized species (i.e. $i = 0$ for Ar, $i = 1$ for $Ar^+$, $i = 2$ for $Ar^{++}$), $n_i$ is the number density of species $i$, $Q_e$ is the electronic partition function, $Q_i$ is the partition function of species $i$, $m_e$ is the electron mass, $k$ is the Boltzmann constant, $T$ is the plasma gas temperature, $h$ is Planck's constant, $e$ is the electric charge of an electron, and $\varepsilon_i$ is the ionization potential of an $i$-times ionized atom. For argon gas, $\varepsilon_1$ and $\varepsilon_2$ are 15.76 and 27.63 eV respectively [23–24] and $Q_i$ is shown in figure 3-4 [25–27].

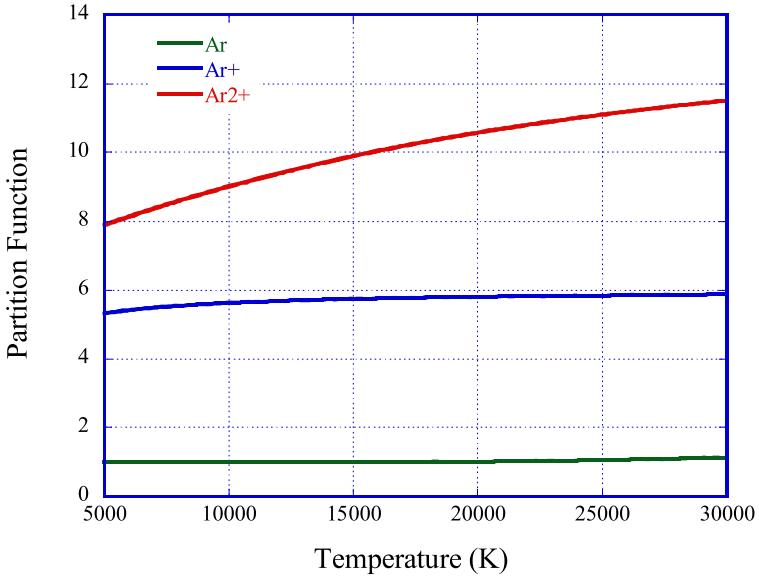


Figure 3-4. Partition function of argon and its ions.

Dalton's law of partial pressures is expressed by:

$$\sum n_i + n_e = \frac{P}{kT}; i = 0, 1, 2 \qquad (Eq. 3-19)$$

where $n_i$ is the number density of Ar, $Ar^+$, and $Ar^{++}$, $n_e$ is the electron number density, $P$ is the gas pressure, $k$ is the Boltzmann constant, and $T$ is the plasma gas temperature.

The quasi-neutrality condition is represented by:

$$n_e = Z_i \sum n_i \,; i = 1, 2 \qquad (Eq. 3-20)$$

where $Z_i$ is the charge number of ions $i$.

Utilizing the Saha equation, Dalton's law of partial pressures and the quasi-neutrality condition, the plasma gas composition for a given total pressure and temperature can be calculated. Figure 3-5 shows the chemical equilibrium composition of argon plasma as a function of gas temperature at a pressure of 1 atm. It shows that argon gas begins to ionize into many singly ionized ions above a temperature of 5000 K and that the singly ionized ions become doubly ionized ions at temperatures above 15,000 K.

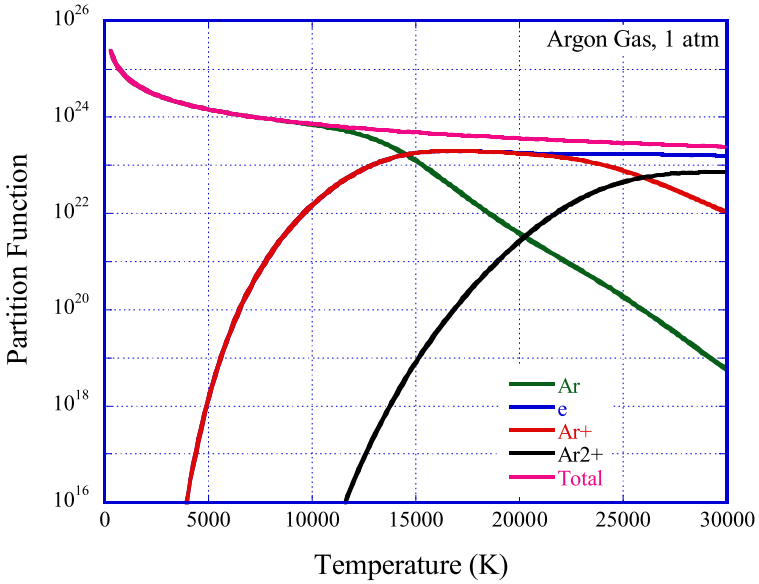


Figure 3-5. Chemical equilibrium composition of a four-component argon plasma as a function of gas temperature at a pressure of 1 atm.

### 3.3.5 Nominal electron temperature

To determine the electrical conductivity of plasma gas, the electron temperature must be calculated. It is difficult to solve the electron energy conservation equation to obtain the electron temperature because of the high nonlinearity and coupling to the other conditions. In the present study, a nominal electron temperature was proposed to approximate the actual electron temperature.

Figure 3-6 shows the nominal electron temperature of argon gas for various electric field strengths at a pressure of 1 atm calculated using equations 3-3 to 3-7. It reveals that a high electric field strength prevents the system reaching equilibrium in which the gas temperature is equal to the electron temperature. Therefore, the nominal electron temperature is much higher than the gas temperature for high electric field strengths, especially for low gas temperatures. In contrast, the nominal electron temperature is similar to the gas temperature for a low electric field strength due to weak ionization. When the

gas temperature is sufficiently high to generate many collisions between heavy particles and electrons, the nominal electron temperature will be similar to the gas temperature with little dependence on the electric field strength.

### 3.3.6 Transport properties of plasma gas

Once the plasma composition has been determined, the total mass density of the plasma gas can be calculated using:

$$\rho = \frac{P}{R_g T} \qquad with\ R_g = k\left(\frac{n_h + n_e}{n_h m_h + n_e m_e}\right) \qquad (Eq. 3-21)$$

where $R_g$ is the gas constant, $k$ is the Boltzmann constant, $T$ is the plasma temperature, $n_h$ is the number density of heavy particles, $n_e$ is the electron number density, $m_h$ is the mass of a heavy particle, and $m_e$ the electron mass.

The calculated gas density is shown in figure 3-7. The plasma gas has a lower density than an ideal gas above a gas temperature of 10,000 K due to ionization.

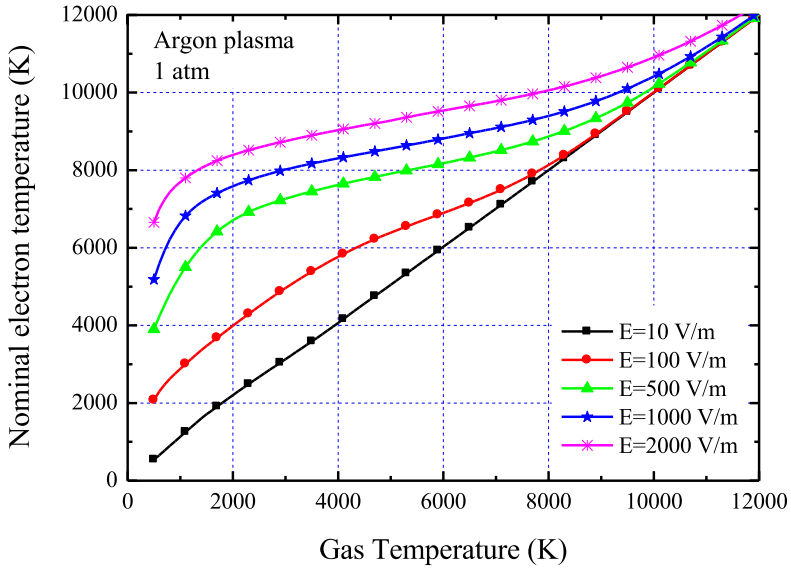


Figure 3-6. Relationship between nominal electron temperature and gas temperature for five different electric field strengths.

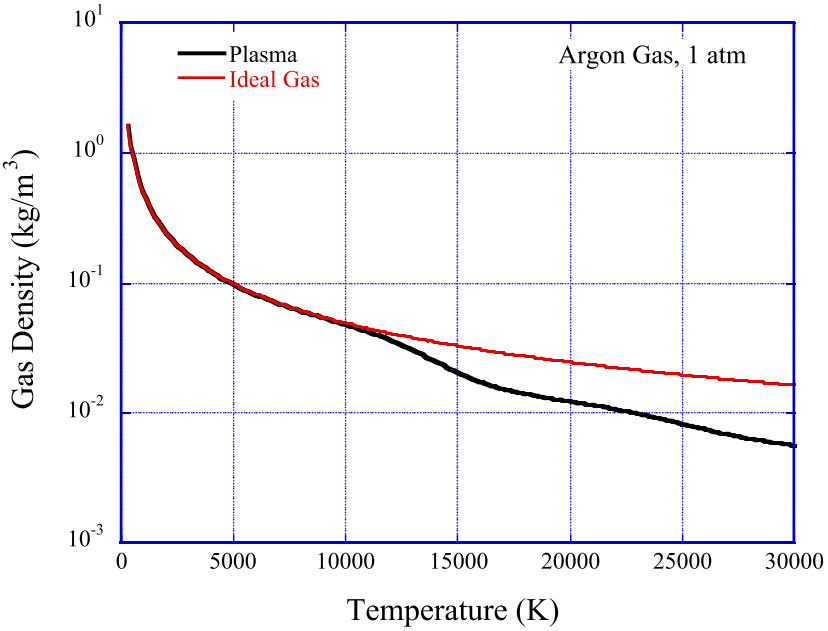


Figure 3-7. Gas density of argon plasma.

As mentioned above, the electrical conductivity of plasma gas depends on the nominal electron temperature in model 3. Methods for calculating the electrical conductivity have been described in several studies [14, 28–30]. Figure 3-8 shows the dependence of the electrical conductivity of argon plasma gas on the electron temperature. Even though figure 3-8 shows that the electrical conductivity of plasma gas is depends on the electron temperature, $Te/T = 1$ can be employed in the two conventional models (models 1 and 2) due to the LTE assumption.

Based on the assumptions given in Section 3.3.1, the other thermodynamic and transport properties (e.g., the specific heat, thermal conductivity, viscosity, and volumetric radiation) of the plasma gas depend only on the gas temperature. The values of these parameters used in the present study are taken from Ref. 22. The specific heat, thermal conductivity, viscosity, and volumetric radiation of argon plasma are plotted in Figures 3-9 to 3-12.

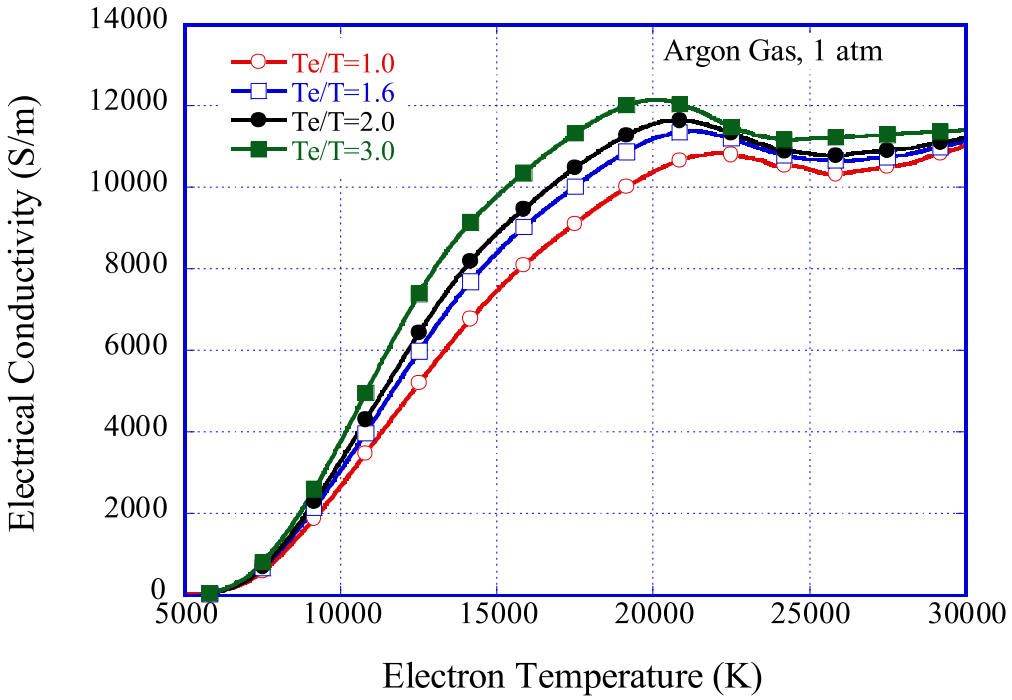


Figure 3-8. Electrical conductivity of argon plasma

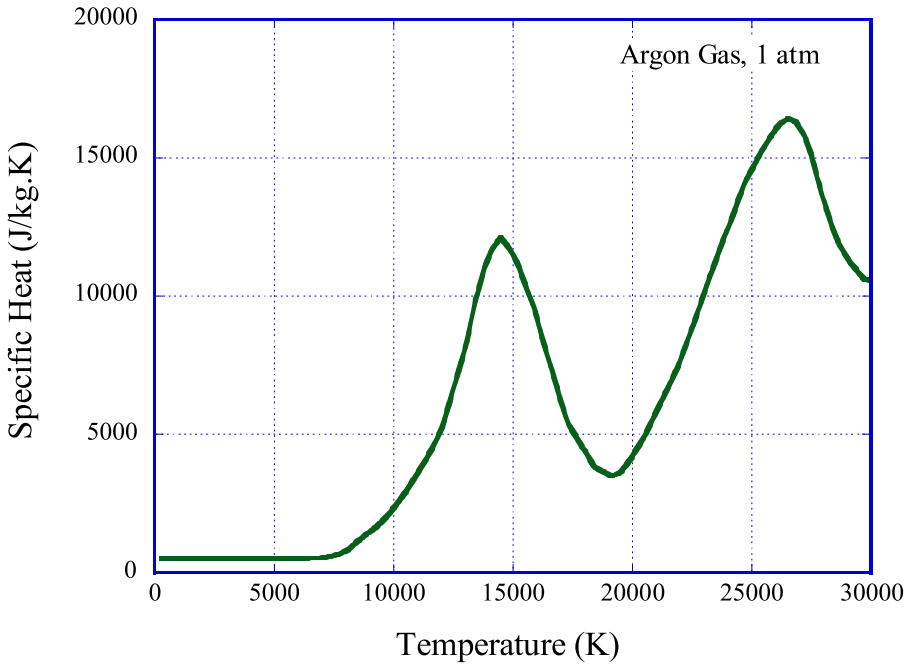


Figure 3-9. Specific heat of argon plasma

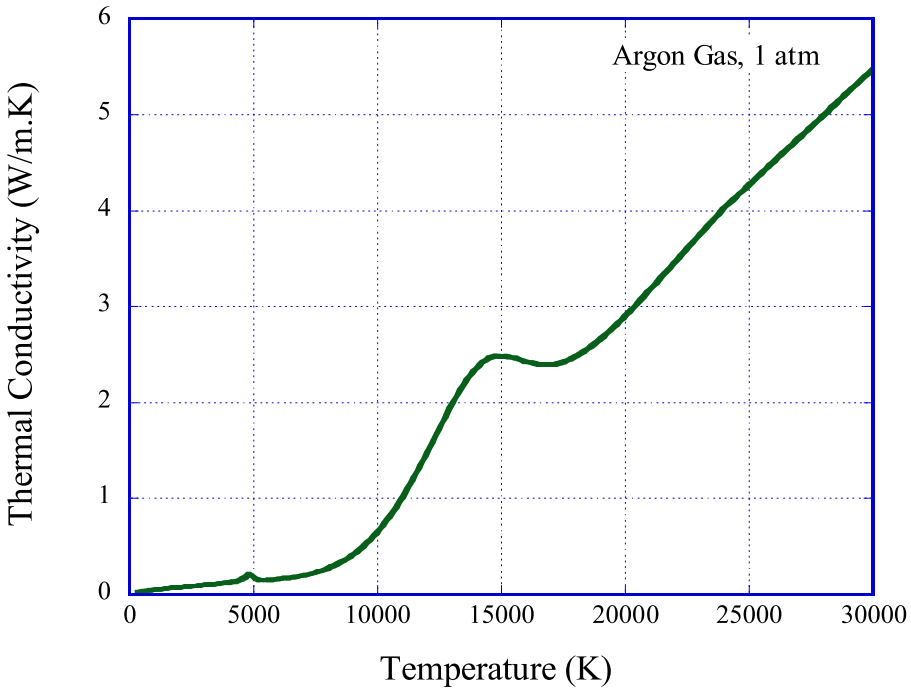


Figure 3-10. Thermal conductivity of argon plasma

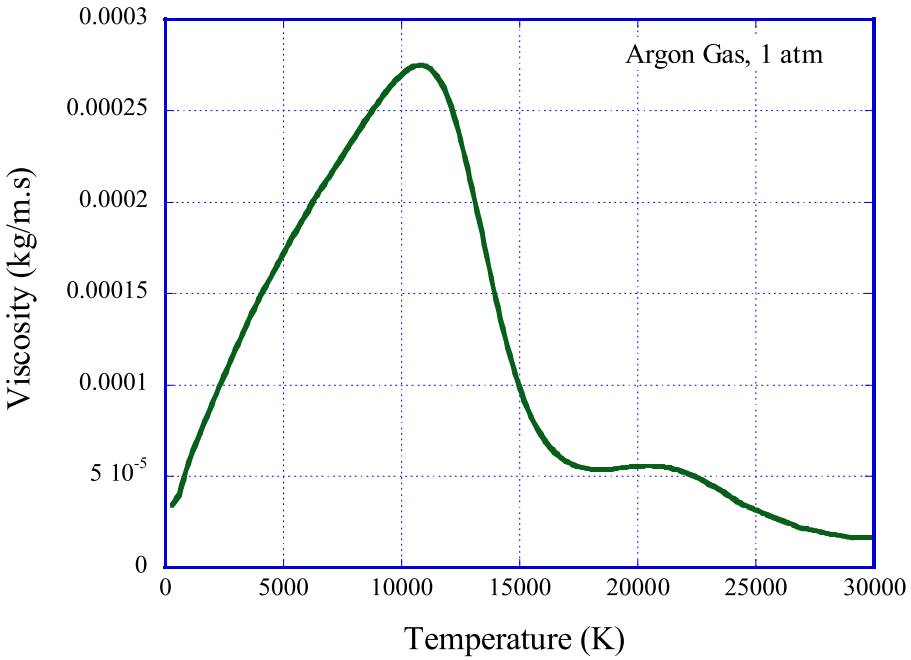


Figure 3-11. Viscosity of argon plasma

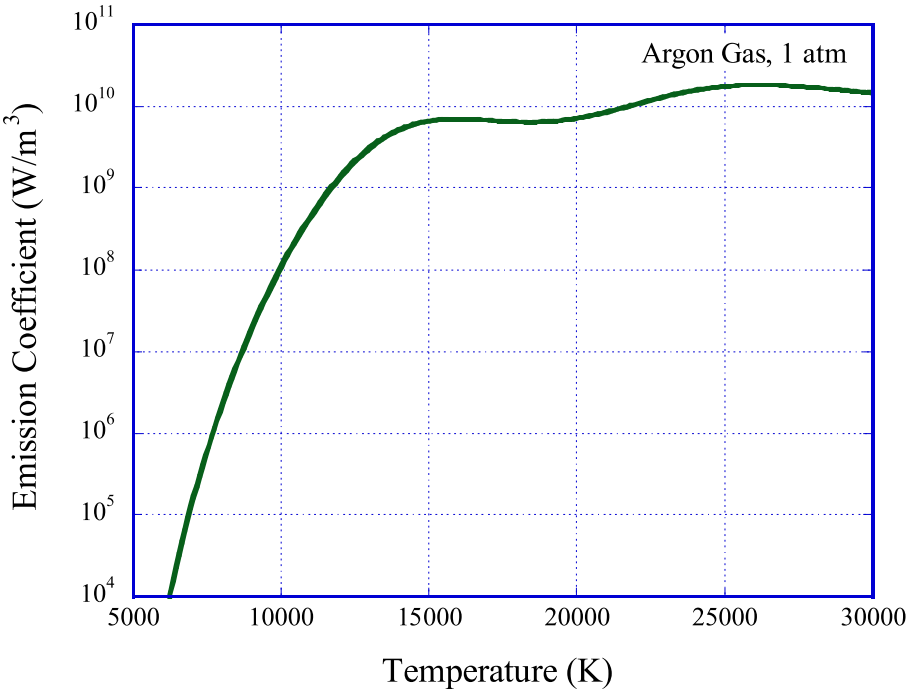


Figure 3-12. Emission coefficient of argon plasma

### 3.3.7 Computational domain and boundary conditions

The geometry used in the present study corresponds to that of the SG-100 plasma torch manufactured by Praxair. Figure 3-13 shows the dimensions of this torch. The computational domain is formed by the region inside the torch defined by the cathode, the gas flow inlet, the anode, and the outlet (see figure 3-14). The computational domain is discretized using structured hexahedral cells. The total numbers of nodes and cells are 224,567 and 217,600, respectively.

As seen in figure 3-14, the boundary of the computational domain has four different faces to allow the boundary conditions to be specified. Tables 3-1 and 3-2 respectively show the gas flow and electromagnetic boundary conditions used in the simulation, where $P_{in}$ represents the inlet pressure (= 111,325 Pa; overpressure: 10 kPa), $h_w$ is the convective heat transfer coefficient at the anode wall (= $2\times10^4$ $W.m^{-2}.K^{-1}$ [9, 11]), and $T_w$ is the cooling water temperature (= 500 K). The boundary conditions for the cathode temperature

$T(r)$ given in Table 3-1 and the electrical current density $j(r)$ given in Table 3-2 are defined by:

$$T(r) = 500 + 3000 \exp\left(-\left(\frac{r}{2R_c}\right)^{n_c}\right) \qquad (Eq. 3-22)$$

$$j(r) = J_{cath0} \exp\left(-\left(\frac{r}{R_c}\right)^{n_c}\right) \qquad (Eq. 3-23)$$

where $r$ is the radial distance from the torch axis ($r^2 = x^2 + y^2$) and $J_{cath0}$ and $n_c$ are the parameters that specify the shape of the current density profile. $R_c$ is a coefficient that ensures that integration of $j(r)$ over the cathode surface equals the total applied current. Table 3-3 lists the values of the shape parameters used in the present study [11, 13–14]. Figure 3-15 shows profiles of the temperature and current density over the cathode surface.

The gas flow inside the plasma torch was calculated using Fluent 6.3, which is commercial computational fluid dynamic (CFD) software. The Simple algorithm is employed in this study to calculate the gas flow. The K–ε model is utilized to deal with the turbulence in the flow.

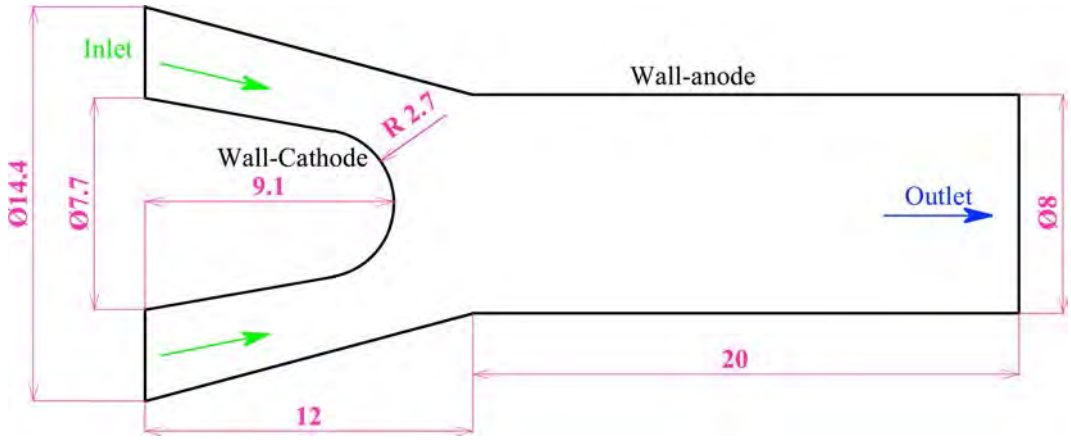


Figure 3-13. Dimensions of SG-100 torch

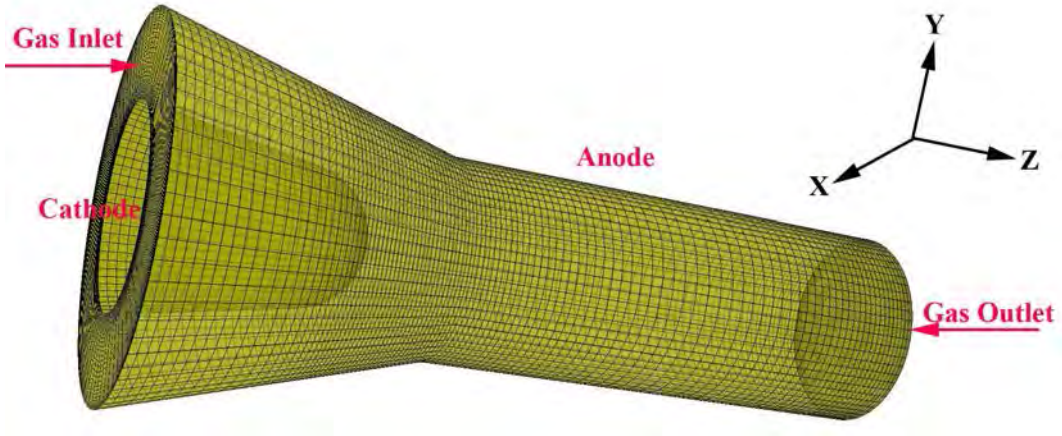


Figure 3-14. Computational domain and mesh of plasma torch

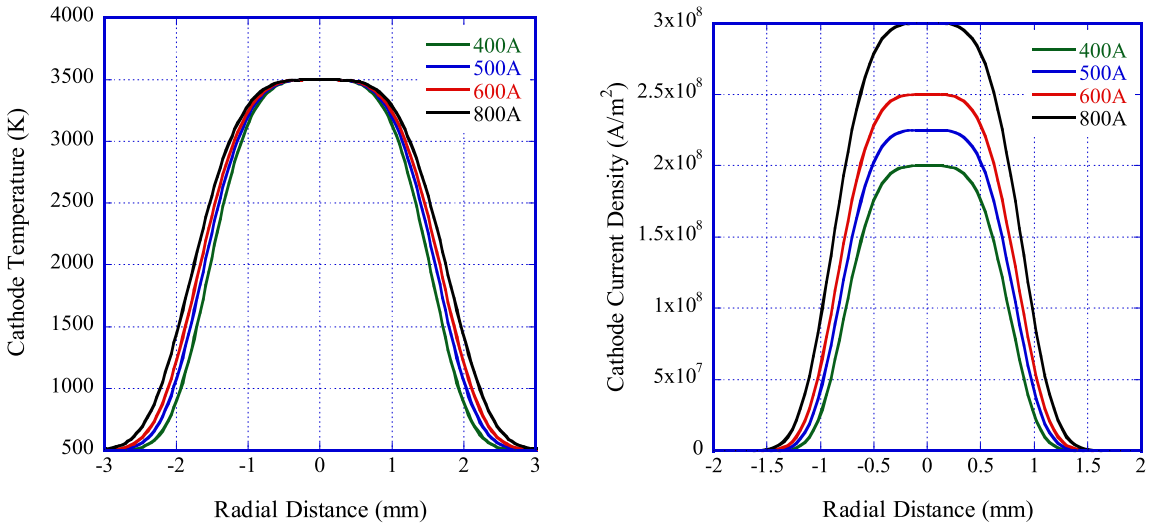


(a) Cathode temperature (b) Cathode current density

Figure 3-15. Profiles of boundary conditions over the cathode surface

To compare the numerical results with the experiment results presented in Chapter 2, the spray conditions used in the simulation are similar those given in Chapter 2; the applied current was varied and the gas flow rate was kept constant at 50 SLM. Table 3-4 lists the detailed conditions used in the current simulation.

Table 3-1. Boundary conditions for the gas flow equations.

| | Pressure | Velocity | Temperature |
|---|---|---|---|
| Inlet | $P_{in}$ | Mass flow rate | 300 K |
| Cathode | $\partial P/\partial n = 0$ | 0 | *T(r)* |
| Anode | $\partial P/\partial n = 0$ | 0 | $Q_a = h_w(T - T_w)$ |
| Outlet | 1 atm | $\partial V_i/\partial n = 0$ | $\partial T/\partial n = 0$ |

Table 3-2. Boundary conditions for the electromagnetism equations.

| | Electrical Potential | Magnetic Potential |
|---|---|---|
| Inlet | $\partial \emptyset/\partial n = 0$ | 0 |
| Cathode | *j(r)* | $\partial A_i/\partial n = 0$ |
| Anode | 0 | $\partial A_i/\partial n = 0$ |
| Outlet | $\partial \emptyset/\partial n = 0$ | $\partial A_i/\partial n = 0$ |

Comment: $\partial/\partial n$ is differentiation in the direction of the (outer-) normal to the boundary.

Table 3-3. Shape parameters of current density.

| Specified Current (A) | $J_{cath0}$ (A/m$^2$) | $n_c$ | Rc (mm) |
|---|---|---|---|
| 400 | 2.0e8 | 4 | 0.835093 |
| 500 | 2.25e8 | 4 | 0.878893 |
| 600 | 2.5e8 | 4 | 0.912245 |
| 800 | 3e8 | 4 | 0.959752 |

Table 3-4: Simulation conditions

| Case No. | Model No. | Gas | Current (A) | Flow rate (SLM) |
|---|---|---|---|---|
| C1 | 1 | Argon | 400 | 50 |
| C2 | 1 | Argon | 500 | 50 |
| C3 | 1 | Argon | 600 | 50 |
| C4 | 2 | Argon | 400 | 50 |
| C5 | 2 | Argon | 500 | 50 |
| C6 | 2 | Argon | 600 | 50 |
| C7 | 3 | Argon | 400 | 50 |
| C8 | 3 | Argon | 500 | 50 |
| C9 | 3 | Argon | 600 | 50 |
| C10 | 3 | Argon | 800 | 50 |

## 3.4 Simulation results and discussion

### 3.4.1 Model 1: Electrical conductivity near the electrode interface is artificially set

**1) Arc voltage and electrical potential inside torch**

Figure 3-16 shows the arc voltage calculated by model 1. It reveals that the arc voltage fluctuates with an amplitude between 52 and 56 V for a current of 400 A, between 50 and 55 V for a current of 500 A, and between 48 and 52 V for a current of 600 A. The arc voltage decreased slightly with increasing applied current.

Figure 3-17 shows the instantaneous electric potential distributions inside the torch at two representative times for observing the voltage drop near the extreme points. Due to the assumption of a higher electrical conductivity near the electrodes, the sheath voltage drop of electrodes cannot be estimated; consequently, the electric potential varies little along the cathode interface. The electric potential is lowest at the cathode interface and highest at the

anode interface according to the boundary conditions for the electrical potential.

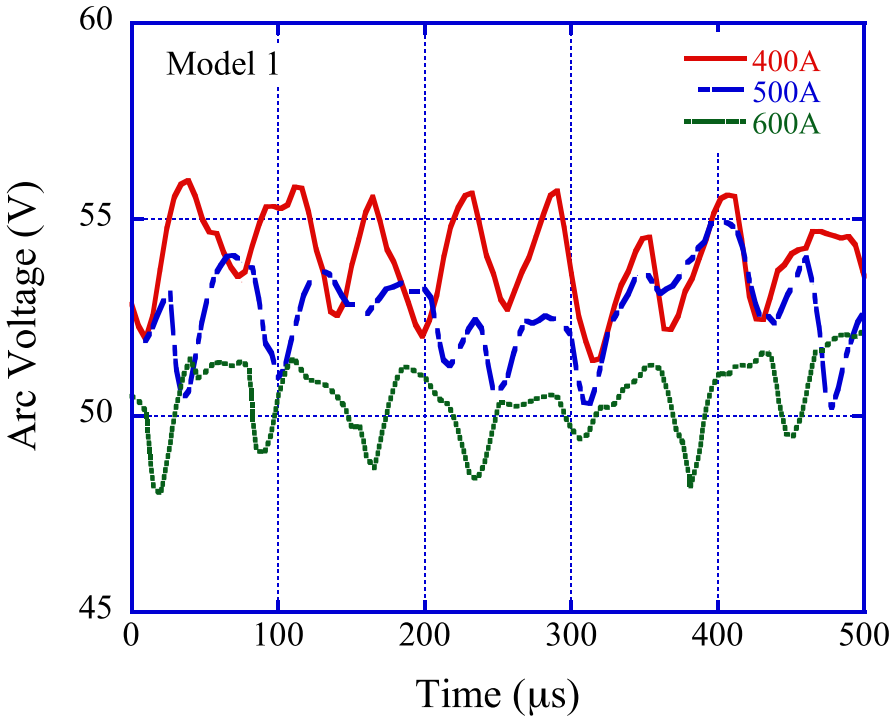


Figure 3-16. Arc voltage calculated by model 1

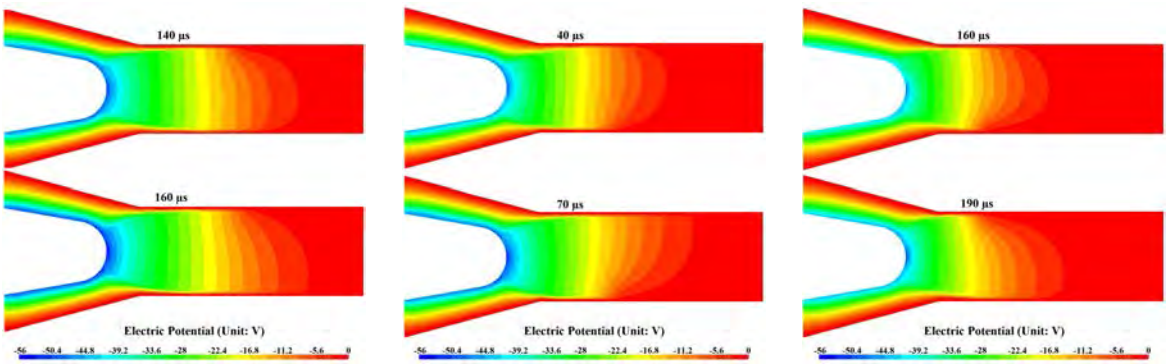


(a) (b) (c)

Figure 3-17. Instantaneous electric potential distributions inside the torch for currents of (a) 400, (b) 500, and (c) 600 A calculated by model 1.

**2) Plasma gas temperature and velocity inside the torch**

Figures 3-18 to 3-21 show the instantaneous gas temperature and velocity distributions inside the torch at several representative times for observing the arc voltage (see figure 3-16). They show that the temperature and velocity distributions of the arc fluctuate with time. The temperature and velocity of the plasma gas inside the torch increase with increasing applied current. The plasma core temperatures are about 32,000, 35,000, and 38,000 K for currents of 400, 500, and 600 A, respectively. The maximum gas velocities inside the torch are about 1300, 1600, and 2000 m/s for currents of 400, 500, and 600 A, respectively.

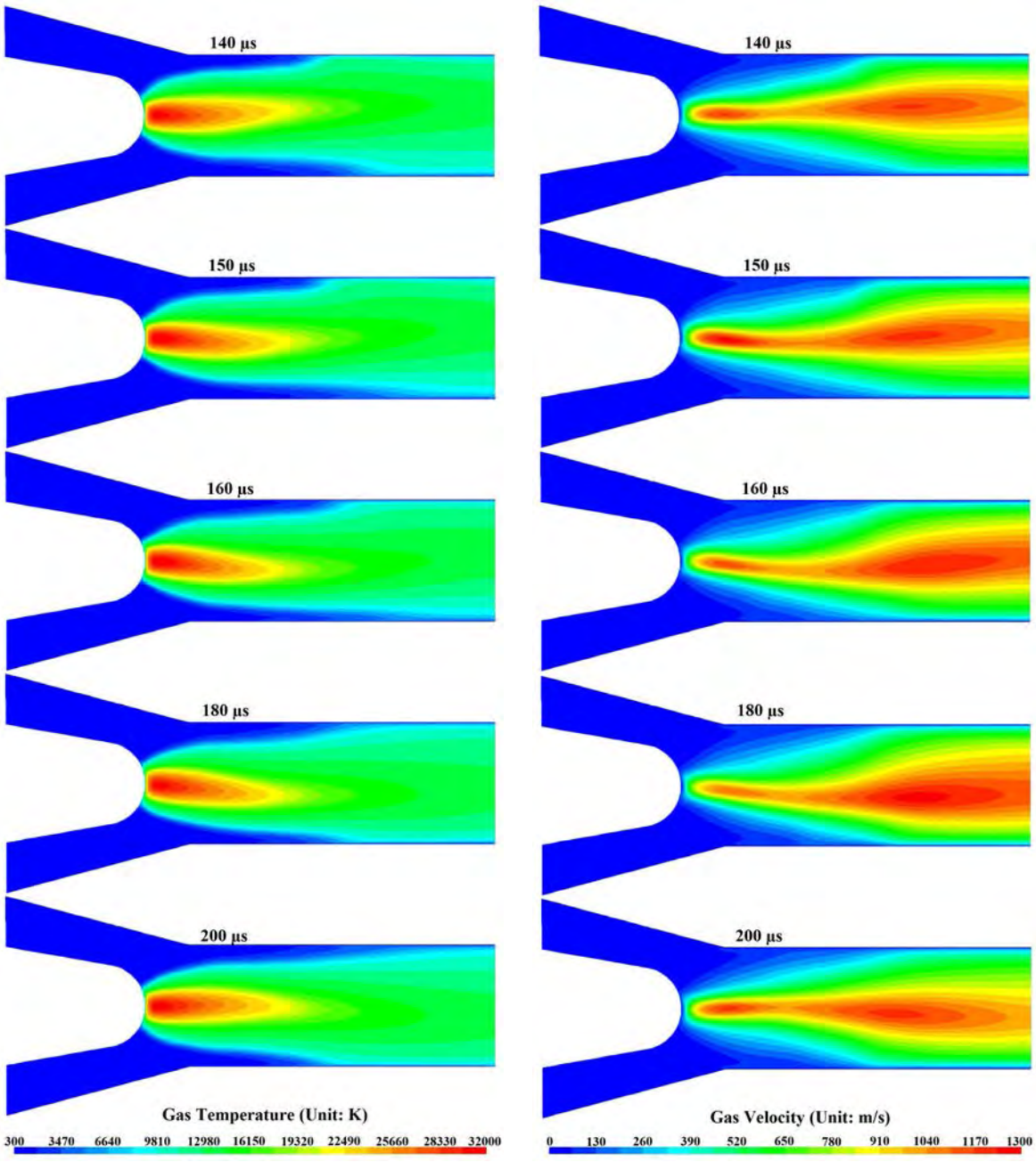


(a) (b)

Figure 3-18. Instantaneous (a) temperature and (b) velocity distributions inside the torch for a current of 400 A calculated by model 1.

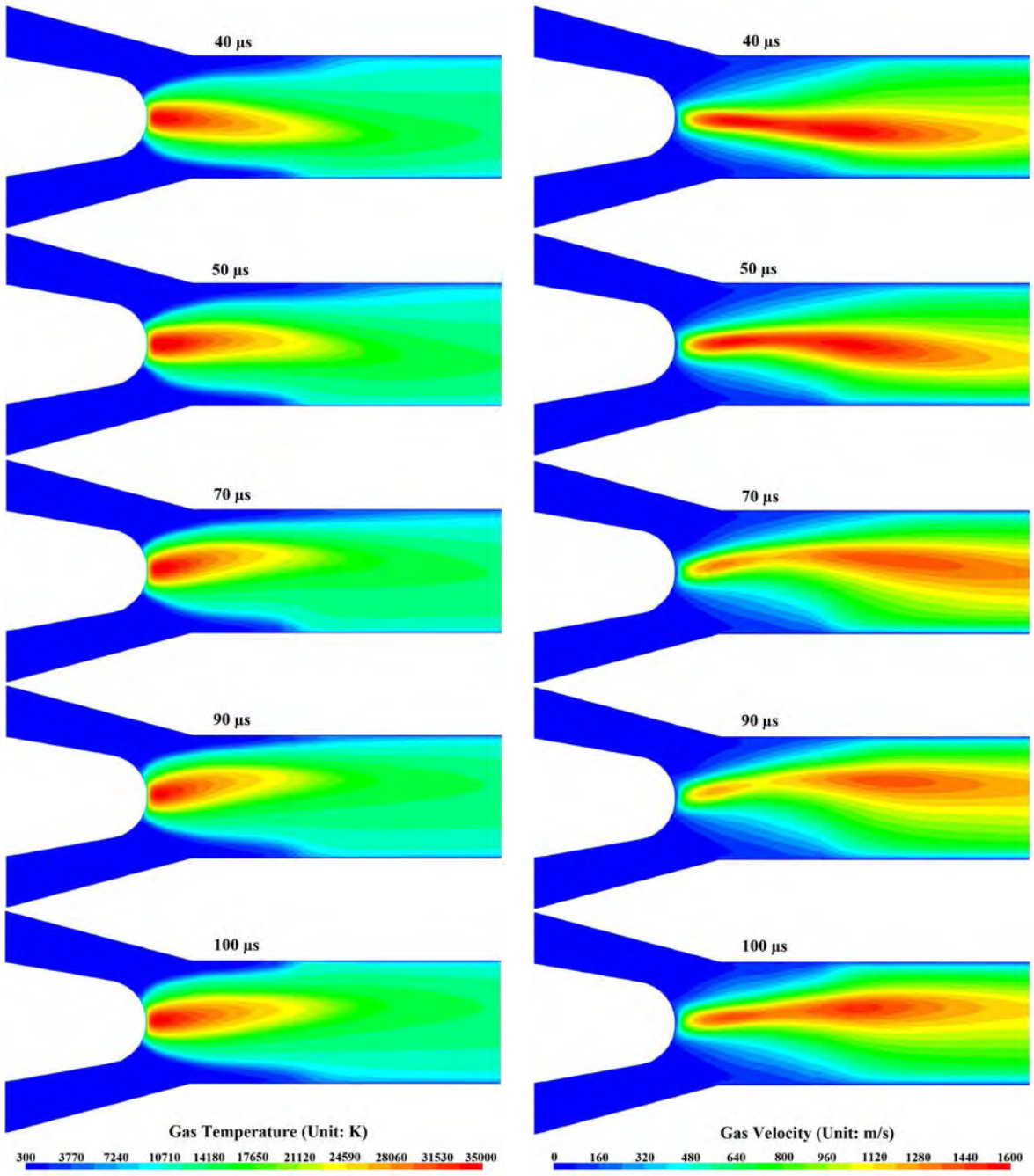


(b) (b)

Figure 3-19. Instantaneous (a) temperature and (b) velocity distributions inside the torch for a current of 500 A calculated by model 1.

To visualize the 3D distribution of gas temperature inside the torch, figure 3-20 shows the temperature distributions in a perpendicular plane to the one shown in figure 3-19 and several axial cross-sections at a time of 70 μs. The arc deviates to the upper boundary (see figure 3-19) at a time of 70 μs, but almost symmetric distribution was obtained in the vertical plane (see figure 3-20(a)). Figure 3-20(b) indicates that the asymmetric arc was obtained due to fluctuations of the arc inside the torch, despite an axisymmetric geometry being used.

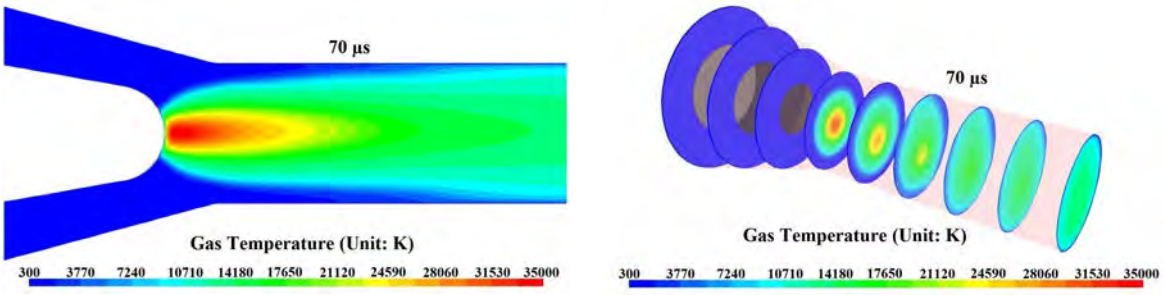


(a) Plane perpendicular to the one in figure 3-19

(b) Axial cross-sections

Figure 3-20. Instantaneous temperature distributions inside the torch at 70 μs for a current of 500 A calculated by model 1.

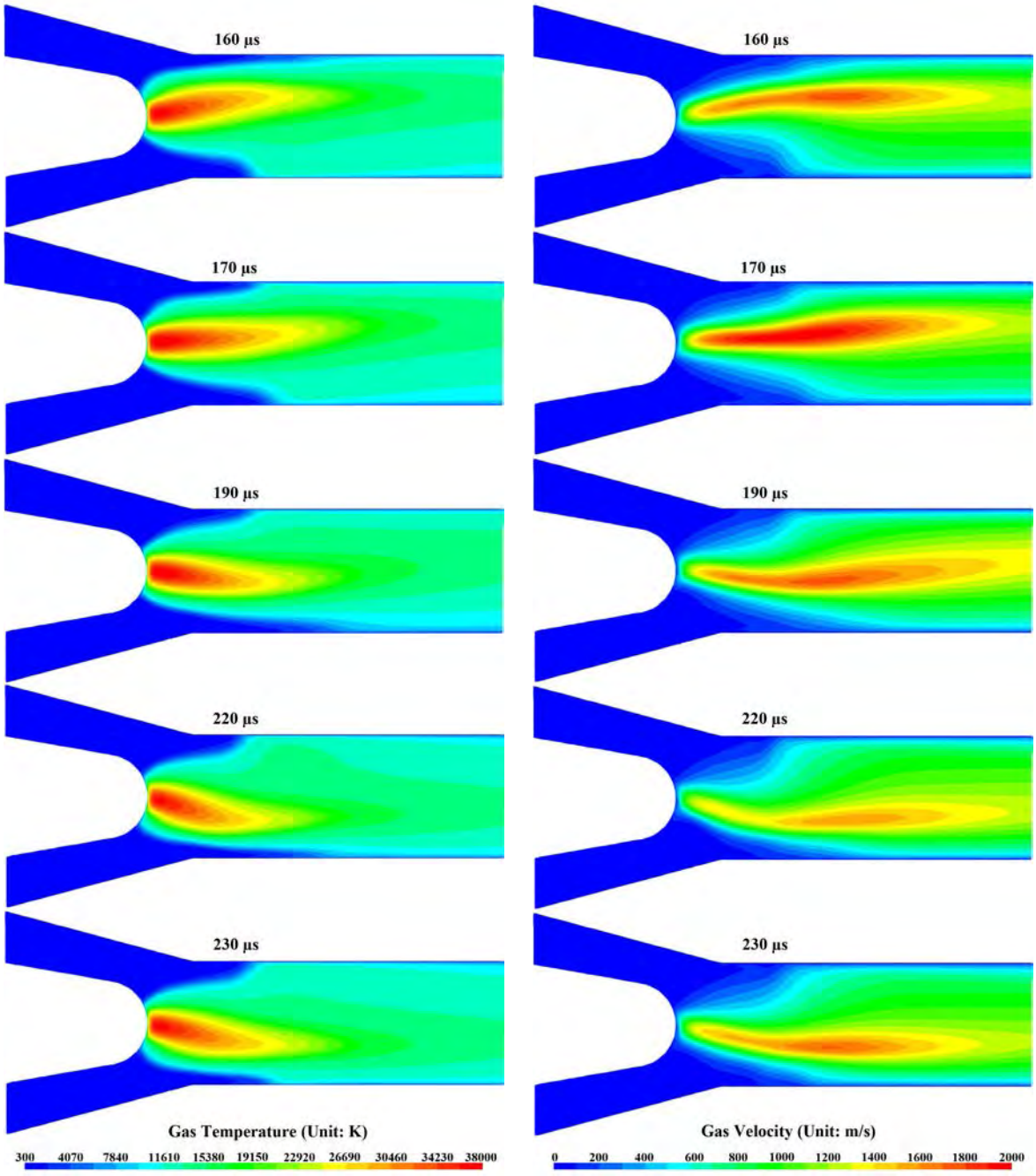


(c) (b)

Figure 3-21. Instantaneous (a) temperature and (b) velocity distributions inside the torch for a current of 600 A calculated by model 1.

**3) Electrical current density distribution inside the torch**

Figure 3-22 shows the electrical current density distributions inside the torch. Figures 3-18 to 3-21 reveal that the gas temperature distributions of the arc gradually deviate to the opposite side of the current attachment. If the temperature distributions of the arc close enough to the anode interface, a new current path will form. Consequently, a current will simultaneously flow through the old and new arc roots. Over time, the old arc root will disappear while the new one will remain (see figure 3-22). Figure 3-22 reveals that the arc length decreases with increasing applied current, so that the arc voltage decreases slightly (see figure 3-16).

**4) Electric field inside the plasma torch**

Figure 3-23 shows the electric field strength distributions inside the torch with argon gas (50 SLM) for currents of 400 to 600 A obtained with model 1. It reveals that the electric field is highest at the edge of the arc near the anode interface.

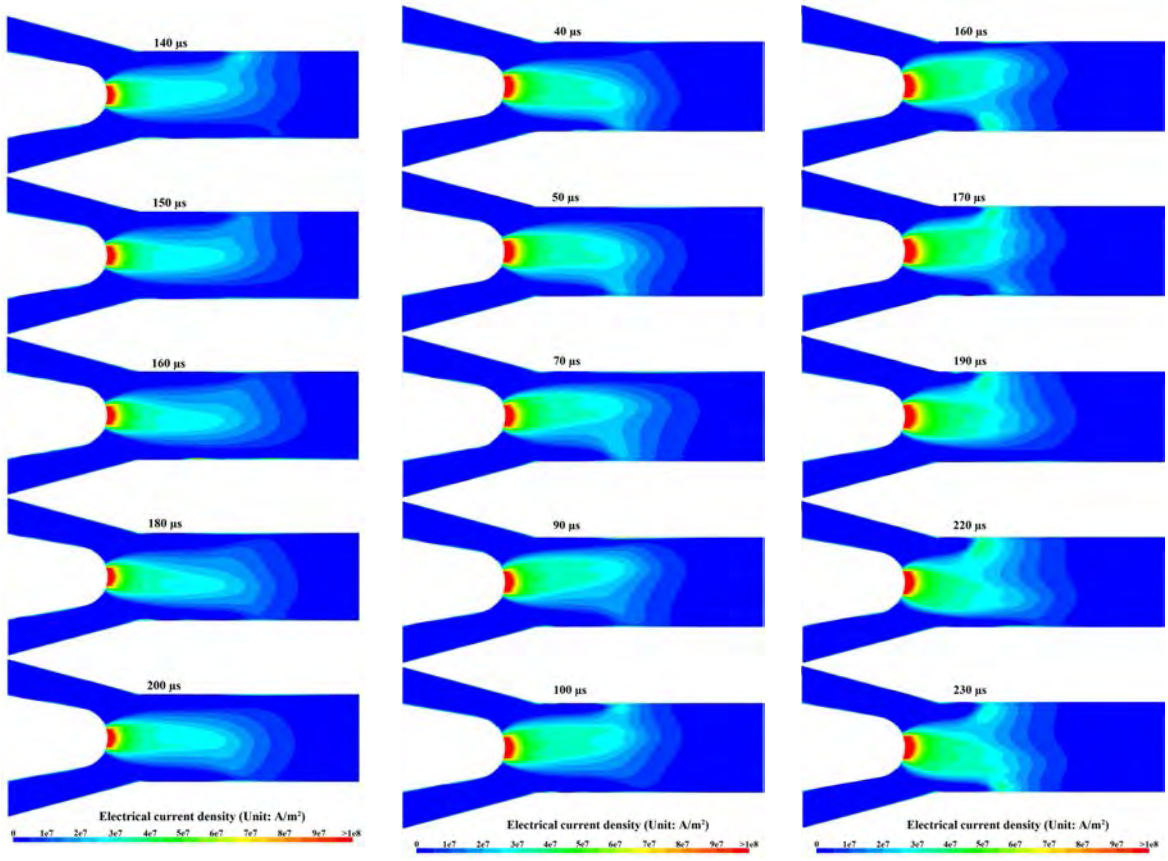


(d) (b) (c)

Figure 3-22. Instantaneous electrical current distributions inside the torch for currents of (a) 400, (b) 500, and (c) 600 A calculated by model 1.

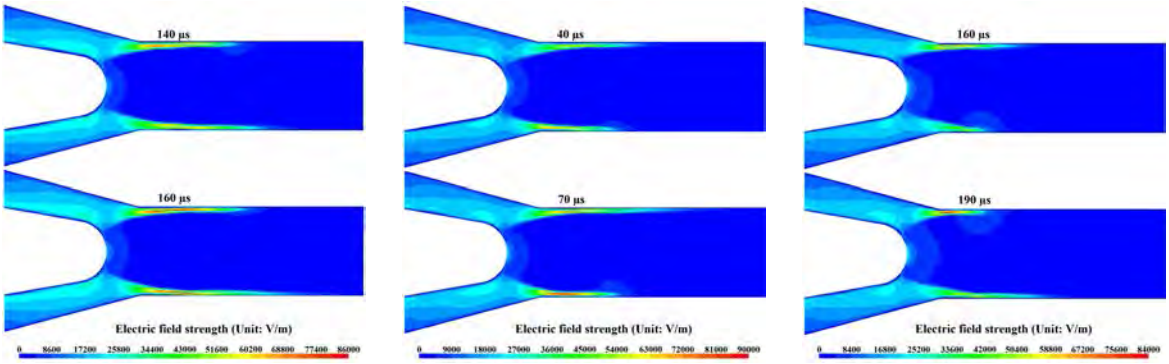


(a) (b) (c)

Figure 3-23. Instantaneous electric field distributions inside the torch for currents of (a) 400, (b) 500, and (c) 600 A calculated by model 1.

**5) Gas flow at torch exit**

Figure 3-24 shows the plasma gas temperature and velocity distributions at the torch exit for currents of 400, 500, and 600 A obtained with model 1. All the plasma gas temperature and velocity distributions are non-axisymmetric due to the arc fluctuations inside the torch. The highest temperature is at the same location as the highest velocity; the gas velocity fluctuates more than the temperature. The maximum gas temperatures at the torch exit are about 14,000, 15,000, and 15,000 K for applied currents of 400, 500, and 600 A, respectively. The maximum gas velocities at the torch exit are about 1150, 1300, and 1400 m/s for applied currents of 400, 500 A, and 600 A, respectively. The gas temperature and velocity tend to increase with increasing applied current.

### 3.4.2 Model 2: artificial breakdown electric field

**1) Electrical field strength and current density distributions inside the torch**

Since the electric field is the main factor in determining the arc attachment on the inner surface of anode in model 2, the electric field is analyzed first. Figure 3-25 shows the instantaneous electric field distributions inside the torch for currents of 400 and 500 A obtained with model 2. Since electric field fluctuates with time, a high electric field will be generated near the anode interface at some time. For applied currents of 400 and 500 A, high electric fields were obtained at times of about 340 and 150 μs, respectively (see figure 3-25). Based on the assumption of model 2, an artificial breakdown path will form when electric field exceeds the preset breakdown electric field of $10^5$ V/m.

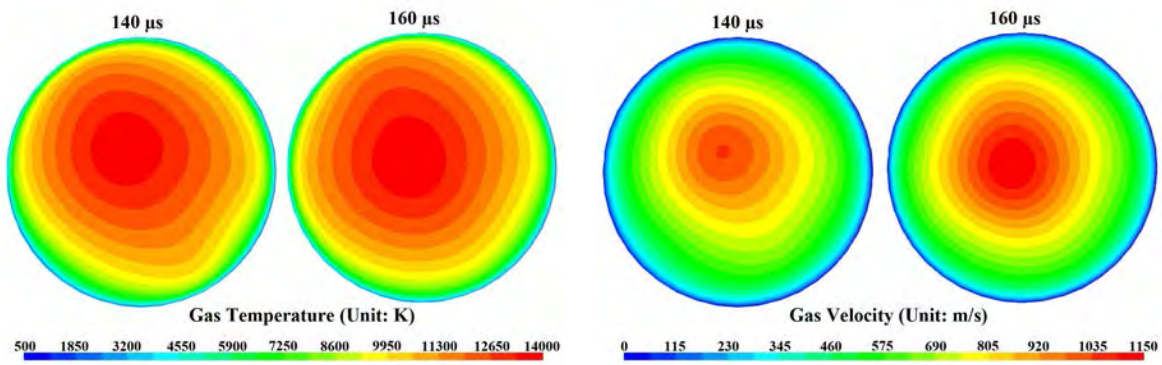


(a)

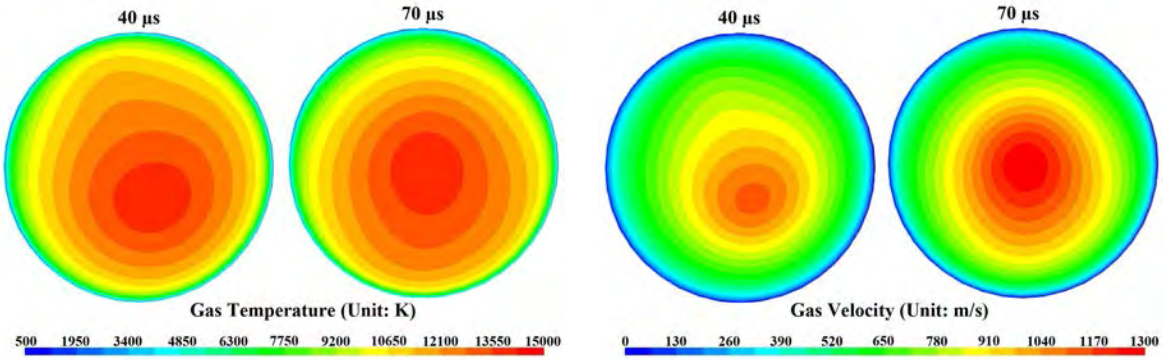


(b)

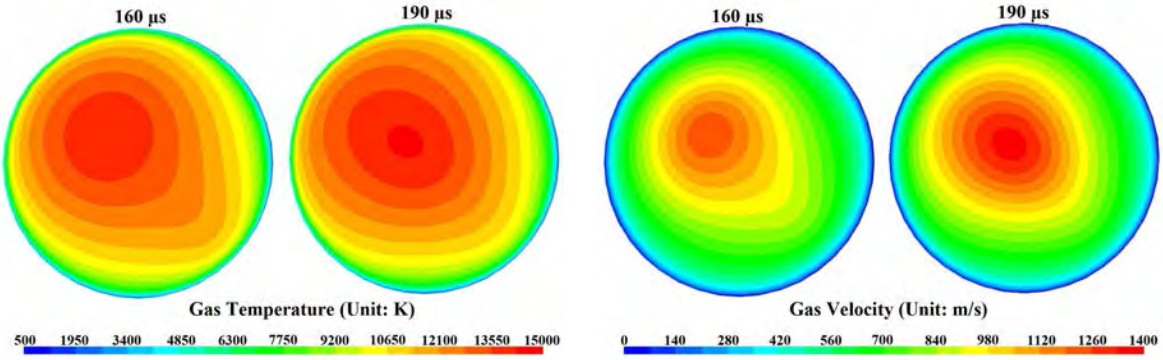


(c)

Figure 3-24. Plasma gas temperature and velocity distributions at the torch exit for currents of (a) 400, (b) 500, and (c) 600 A calculated by model 1.

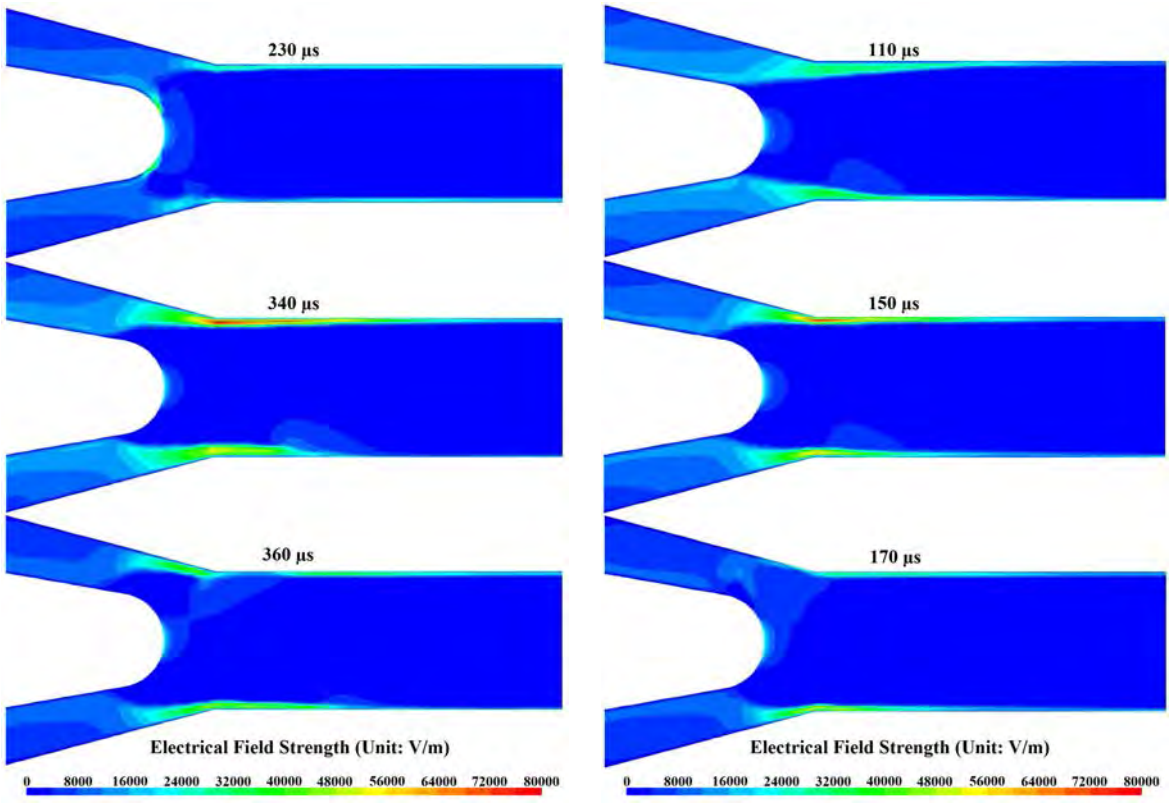


(a) (b)

Figure 3-25. Instantaneous electric field strength distributions inside the torch for currents of (a) 400 and (b) 500 A calculated by model 2.

Figure 3-26 shows the instantaneous electrical current density distributions inside the torch for currents of 400 and 500 A calculated by model 2. It shows that the arc fluctuates inside the torch due to the movement and transition of the arc attachment (arc root). For an applied current of 400 A, the arc root moves downstream and the arc length increases from 210 to 340 μs; this is attributed to the flow drag force exceeding the electromagnetic force. The electric field distributions in figure 3-25 reveal that the electric field somewhere upstream becomes stronger with downstream movement of the arc root. At some time prior to 360 μs, the maximum electric field at the location exceeds the preset breakdown electric field, resulting in the formation of a new electric current path and a sudden reduction in the electric field in the region of the previous highest electric field (see figure 3-25). The

assumptions employed in model 2 appear to be valid. The same phenomena are observed for an applied current of 500 A. The arc root moved downstream from 20 to 110 μs and this caused the electric field to increase somewhere upstream on the opposite side of arc root (see figure 3-25). As the electric field increase continually at the specific location, a new arc root will form due to the specified artificial conduction channel, as shown in figure 3-26 at a time of 160 μs.

**2) Plasma gas temperature and velocity inside the torch**

As figure 3-26 shows, the parameters inside the plasma torch are expected to fluctuate and the arc root moves and transitions. Figures 3-27 to 3-29 show the time evolutions of the gas temperature and velocity distributions inside the plasma torch for applied currents of 400, 500, and 600 A, respectively. They show that the gas temperature and velocity fluctuate inside the torch for all three applied currents. The arc attachment observed in the profiles of gas temperature distributions and the locations are nearly identical to the ones in the profiles of electric current density distributions (see figure 3-26). Careful observation of the temperature, electric current density, and field distributions reveals that the arc of temperature distributions deviates to the opposite side of the electrical current density distributions with time until a new arc attachment forms. The electric field at the fringe of the arc becomes stronger as the temperature distribution of the arc deviates. Once a local electric field exceeds the preset breakdown electric field, a new electric current path forms through this location, initiating the next stage of arc root transition.

The fluctuation of the gas velocity is more significant than that of the gas temperature inside the torch. The gas temperature and velocity increase with increasing applied current. The maximum temperatures inside the torch are about 34,000 37,000, and 40,000 K for applied currents of 400, 500, and 600 A, respectively. The maximum velocities inside the torch are about 1600, 2000, and 2400 m/s for applied currents of 400, 500, and 600 A, respectively.

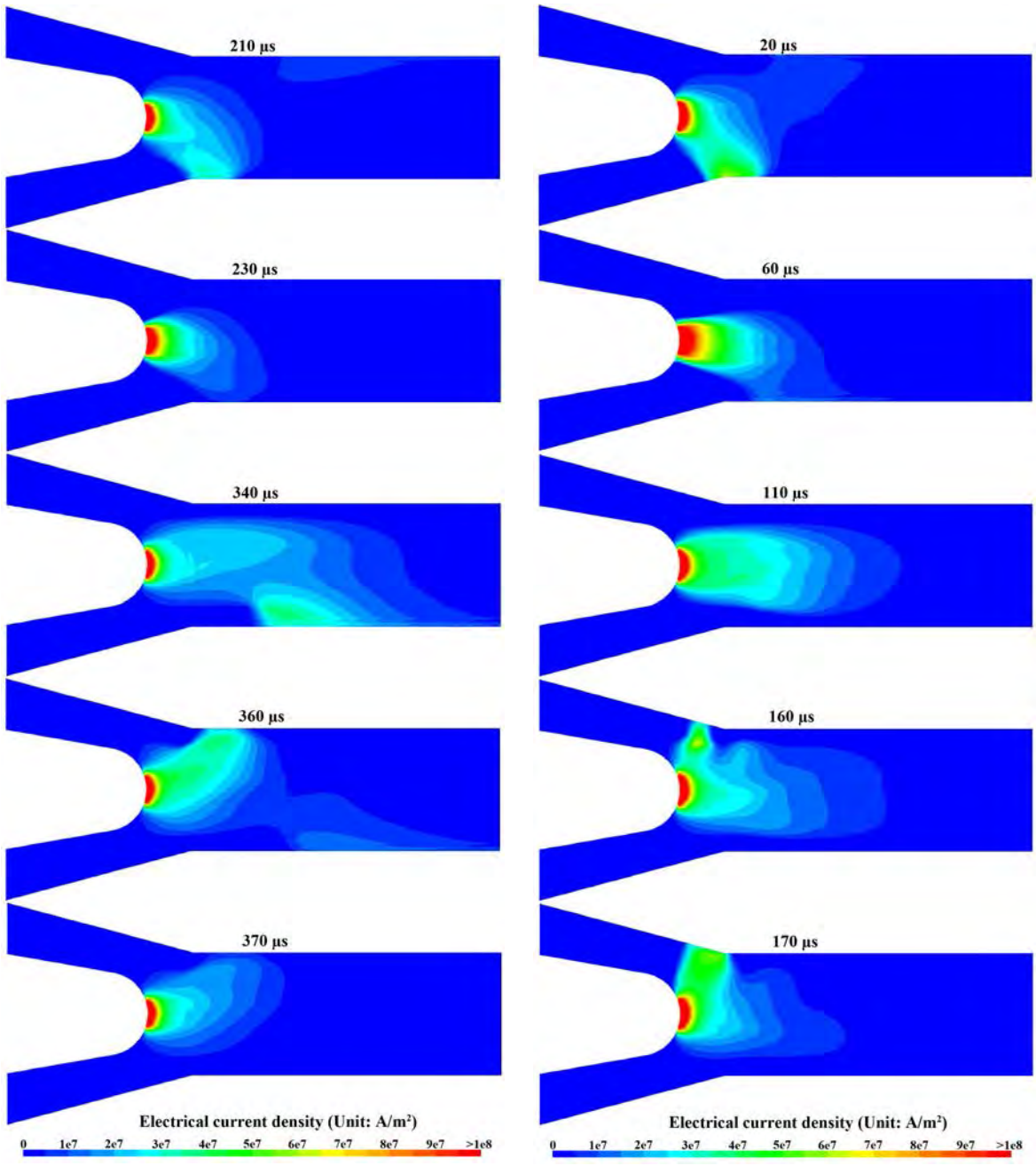


(a) (b)

Figure 3-26. Instantaneous electrical current density distributions inside the torch for currents of (a) 400 and (b) 500 A calculated by model 2.

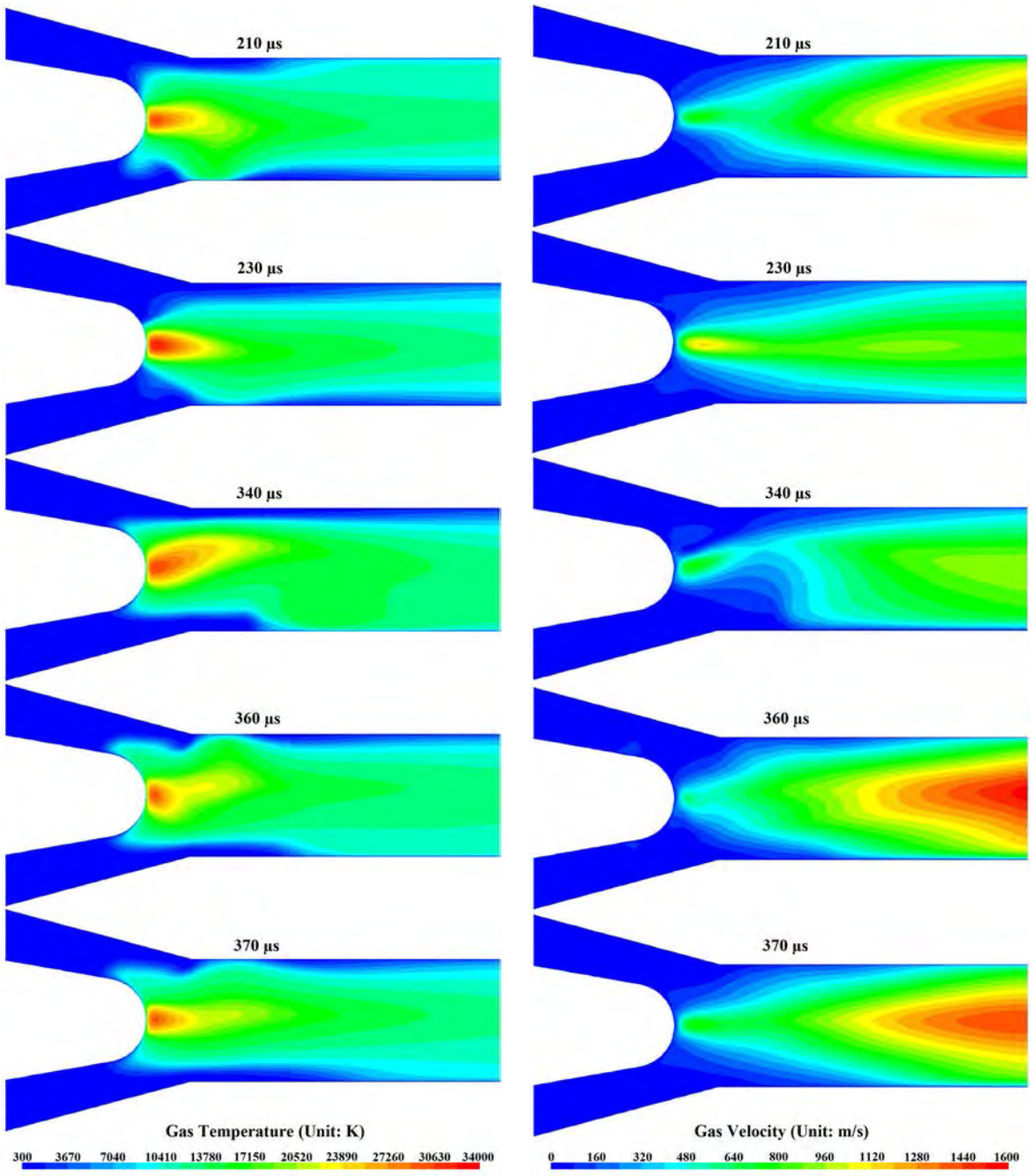


(e) (b)

Figure 3-27. Instantaneous (a) temperature and (b) velocity distributions inside the torch for a current of 400 A calculated by model 2.

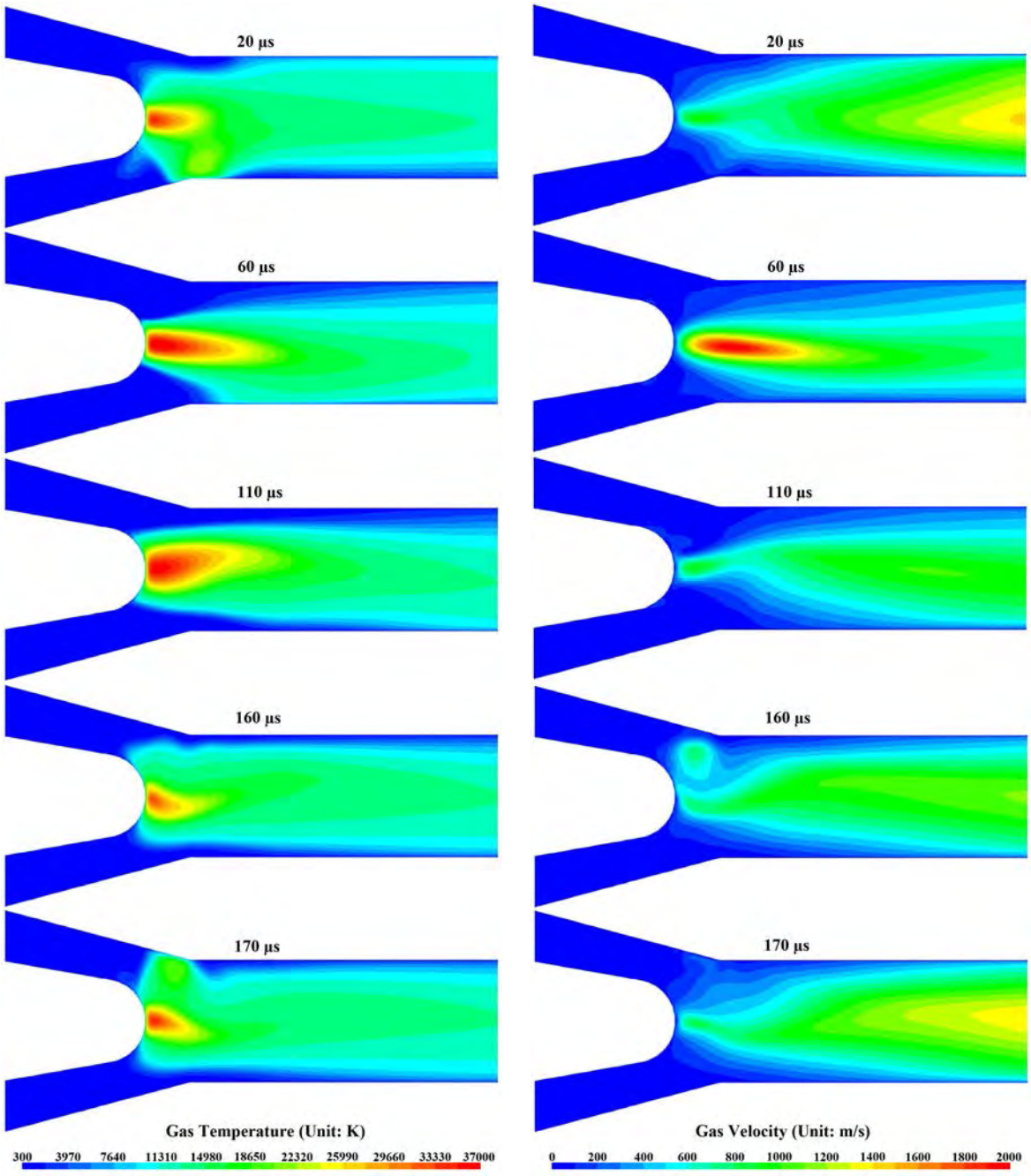


(a) (b)

Figure 3-28. Instantaneous (a) temperature and (b) velocity distributions inside the torch for a current of 500 A calculated by model 2.

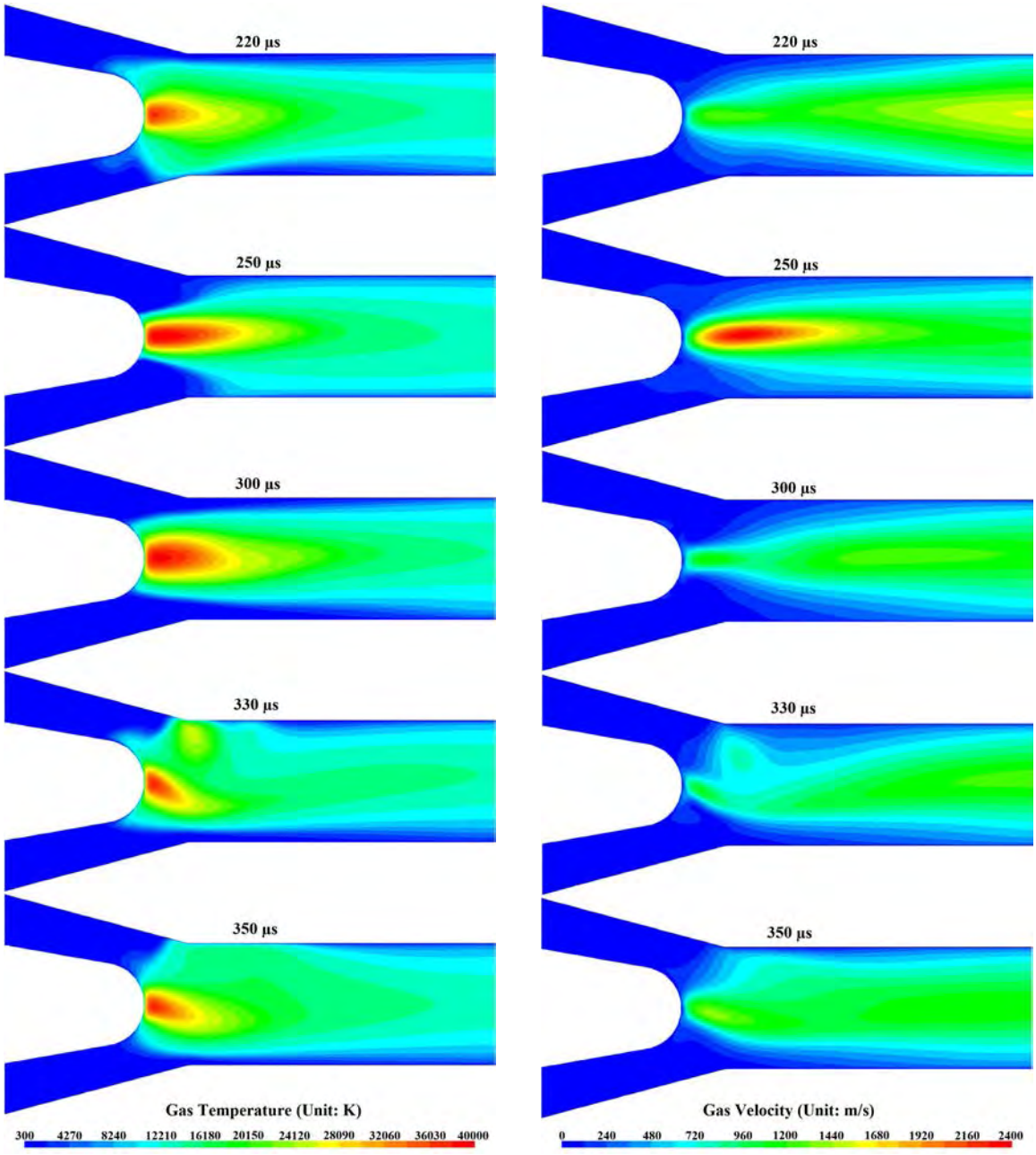


(f) (b)

Figure 3-29. Instantaneous (a) temperature and (b) velocity distributions inside the torch for a current of 600 A calculated by model 2.

**3) Arc voltage and electrical potential inside the torch**

Figure 3-30 shows the arc voltage calculated by model 2. It reveals that the arc voltage fluctuates inside the torch due to movement and transition of the arc root.

Comparison with figure 3-26, which shows the current density distributions, reveals that the arc voltage is proportional to the arc attachment length. The arc voltage increases as the arc root moves downstream and decreases as a new root forms. The average arc voltage increases slightly when the applied current is increased from 400 to 600 A and the arc voltage fluctuates with an amplitude between 30 and 60 V in model 2.

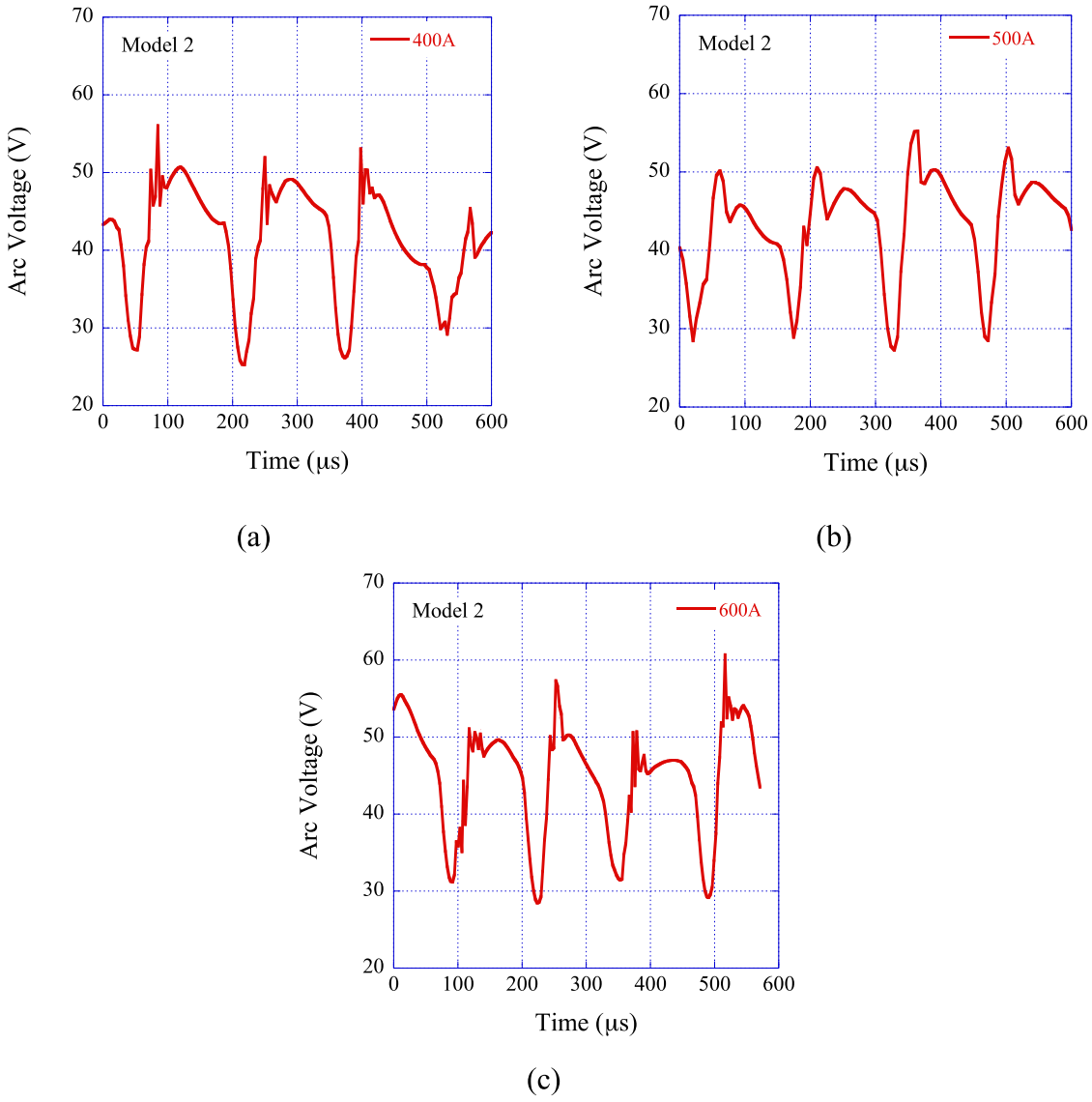


Figure 3-30. Arc voltage for an applied currents of (a) 400, (b) 500, (c) and 600 A calculated by model 2

Figure 3-31 shows the instantaneous electric potential distributions inside the torch at two representative times for observing the arc voltage near the extreme points when a current of 500 A is applied. This figure reveals that the electric potential inside the torch fluctuates, similar to the other parameters inside the torch. Observing the electric potential distribution, the electrical potential varies along the cathode interface despite the fact that a uniform electric potential is applied to the cathode. The minimum electrical potential of the plasma gas is observed at the cathode tip; the electrical potential along the cathode interface decreases with increasing distance from the cathode tip. This is due to the voltage drop in the cathode sheath, which is not considered in the present study. Benilov [31] and Zhou and Heberlein [32] found that increasing the temperature and the electric current density reduces the voltage drop in the sheath. Since the electrical potential of the gas at the cathode interface should be the value of the torch voltage subtracting the sheath voltage drop, different electrical potential is observed at the cathode interface because of the different sheath voltage drop.

**4) Gas flow at the torch exit**

Figure 3-32 shows the plasma gas temperatures and velocity distributions at the torch exit for currents of 400, 500, and 600 A obtained with model 2. Similar to the results obtained using model 1, all the plasma gas temperature and velocity distributions are non-axisymmetric due to arc fluctuation inside the torch. The region of high gas temperature is close to that of high gas velocity and the velocity fluctuates more than the temperature. The maximum gas temperatures at the torch exit are about 13,500, 13,500, and 14,500 K for applied currents of 400, 500, and 600 A, respectively. The maximum gas velocities at the torch exit are about 1440, 1440, and 1600 m/s for applied currents of 400, 500, and 600 A, respectively. The gas temperature and velocity at the torch exit tend to increase slightly with increasing applied current.

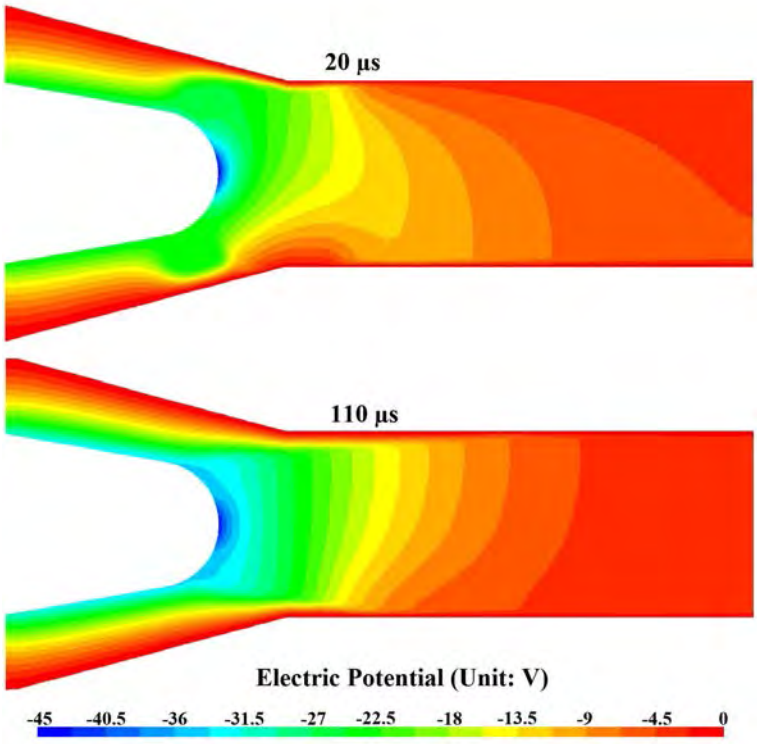


Figure 3-31. Instantaneous electric potential distributions inside the torch for a current of 500 A calculated by model 2.

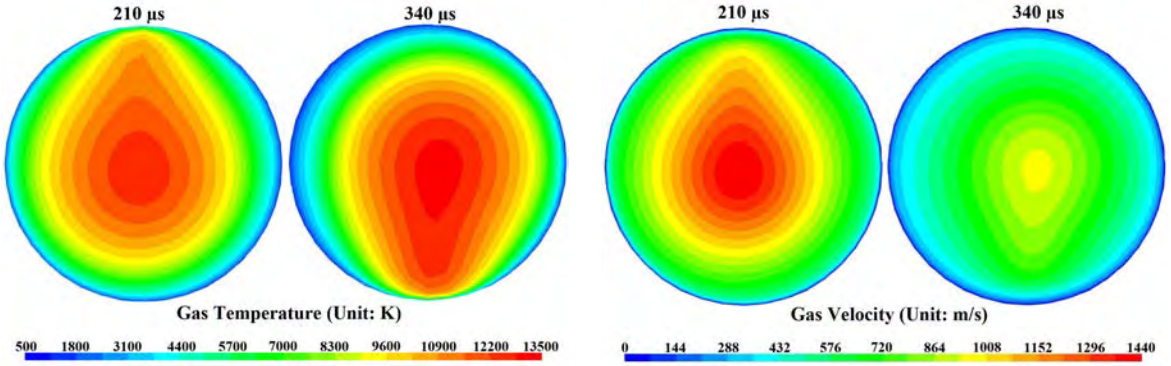


(a)

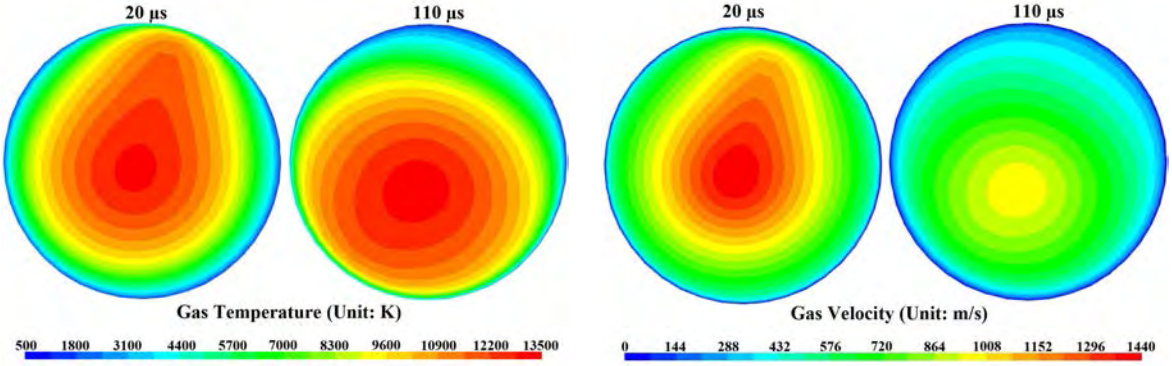


(b)

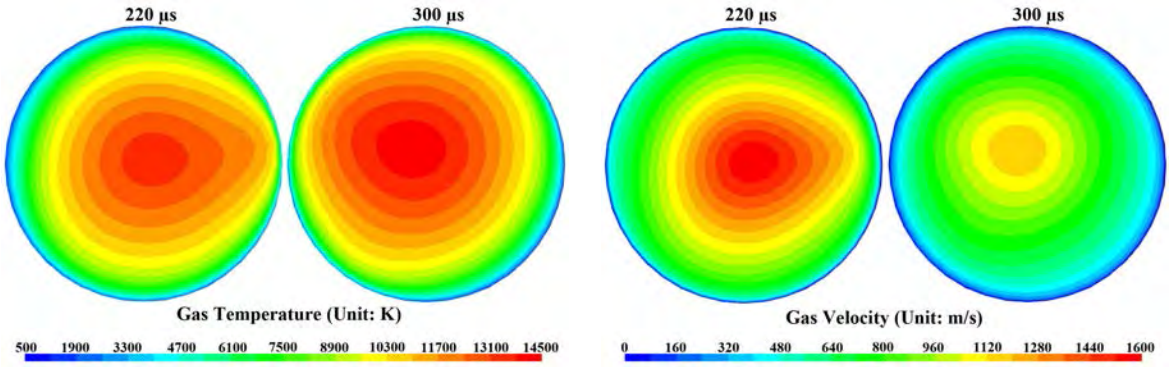


(c)

Figure 3-32. Plasma gas temperature and velocity distributions at the torch exit for currents of (a) 400, (b) 500, and (c) 600 A calculated by model 2.

### 3.4.3 Model 3: nominal electron temperature

#### 1) Electric field and nominal electron temperature

Figure 3-33(a) shows the electric field distribution of a cross section of the torch at 250 μs for an applied current of 600 A calculated by model 3. It reveals that there is a high electric field in the circular field from the cathode tip to the internal anode surface near the inner corner. As a result of the assumption used in model 3, the nominal electron temperature in this area will differ greatly from the heavy particle temperature. Figure 3-33(b) shows the calculated nominal electron temperature distribution inside the torch. The nominal electron temperature is clearly higher than the gas temperature; this difference varies with region. In the high temperature region near the plasma core, the nominal electron temperature is similar to the gas temperature since there are sufficiently many collisions between electrons and heavy particles due to the high gas temperature. However, the nominal electron temperature and the gas temperature differ significantly far from the plasma core, especially in regions near the inner corner on the internal surface of the anode where the nominal electron temperature is over 10,000 K. This is because there are too few collisions between the electrons and the heavy particles in regions with low gas temperatures, resulting in a large temperature difference between the electrons and the gas. Consequently, the electrical current can flow to the anode despite the lower gas temperature near the anode interface due to the higher electrical conductivity, which is determined by the nominal electron temperature. Therefore, the problem of a low electrical conductivity near the anode interface in conventional LTE models has been overcome in this study via the calculation of the nominal electron temperature. By employing the assumption used in model 3, simulations can be executed without making further assumptions about the electrical conductivity.

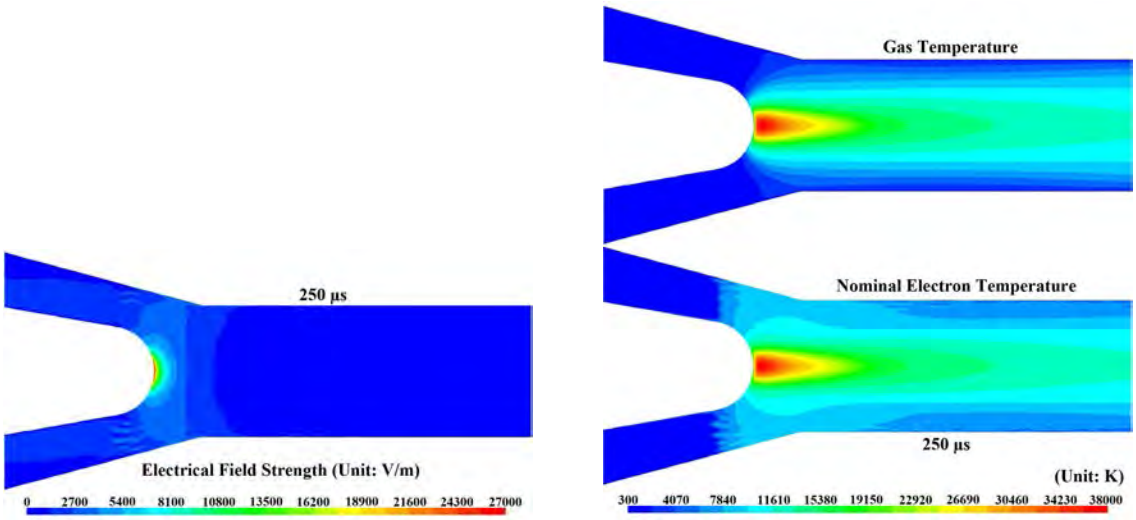


(a) (b)

Figure 3-33. (a) Electric field and (b) gas and nominal electron temperature distributions of a cross-section inside the torch at 250 μs for an applied current of 600 A.

**2) Electrical current density**

Figure 3-34 shows the electric current density distributions inside the torch calculated by model 3. It reveals that the arc length (i.e., the length of the high electric current density region) remains almost constant with time for applied currents of 400 and 500 A. However, the arc length varies with time for applied currents of 600 and 800 A. The electric current distributions reveal that relatively steady arcs are generated for the lower applied currents of 400 or 500 A, whereas the arc fluctuates for applied currents of over 600 A. Furthermore, the arc length increases with increasing applied current. Even though the arc length varies with time and applied current (see figure 3-34), the arc attachment on the internal surface of anode is in a similar location, namely the region where most of the electrical current passes through.

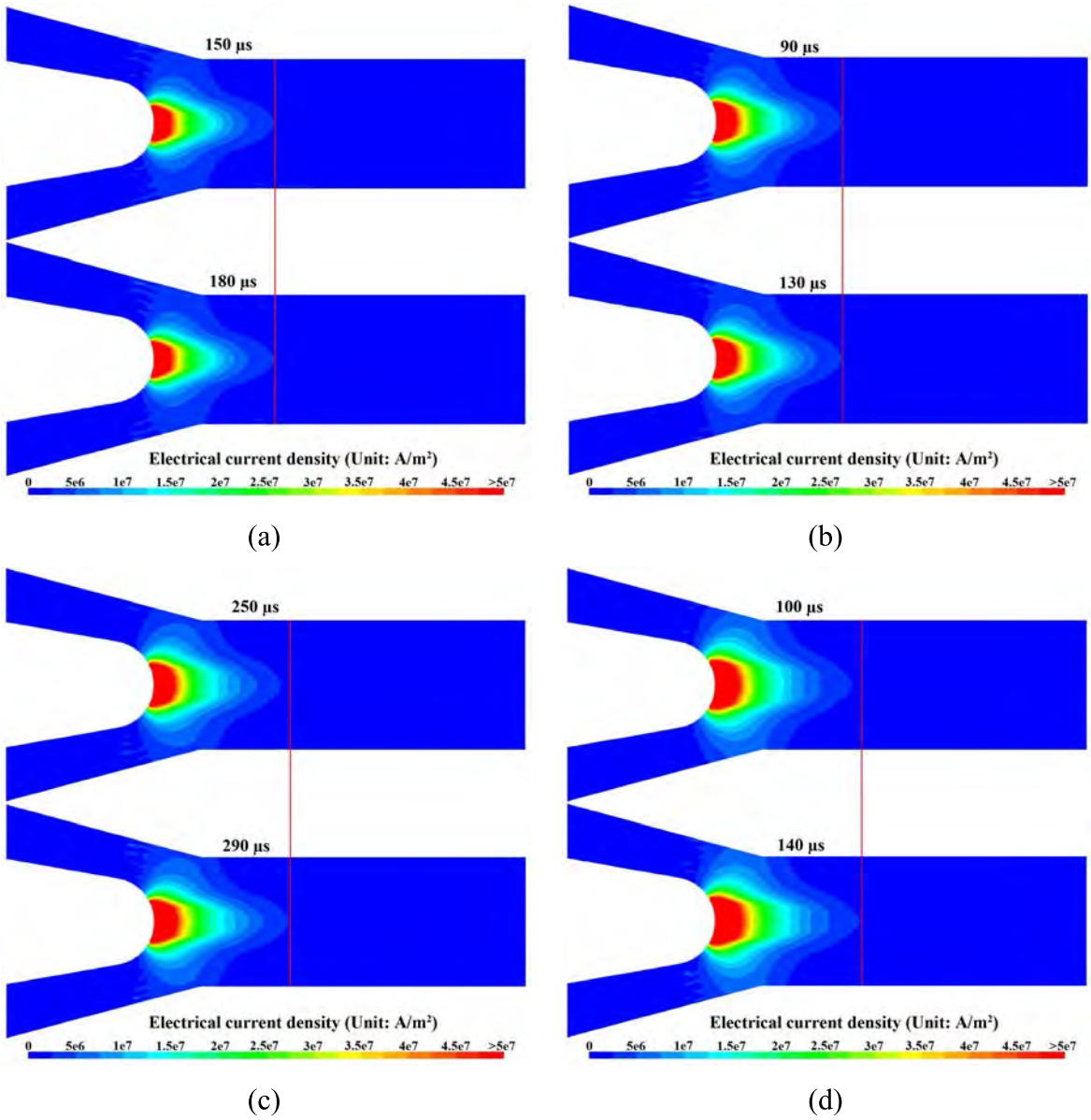


Figure 3-34. Electric current density distributions of a cross-section inside the torch for applied currents of (a) 400, (b) 500, (c) 600, and (d) 800 A calculated by model 3.

**3) Plasma gas temperature and velocity inside the torch**

Figures 3-35 to 3-38 show the instantaneous temperature and velocity distributions inside the torch calculated by model 3 for applied currents of 400, 500, 600, and 800 A, respectively. They reveal that the temperature and velocity distributions are nearly axisymmetrical for all the electric currents used. The temperature and velocity remain

almost constant with time for applied currents of 400 and 500 A, whereas they vary slightly with time for applied currents of 600 and 800 A due to fluctuations in the electric current inside the torch (see figure 3-34). It seems that model 3 cannot completely model the arc fluctuations inside the plasma torch, especially in the radial direction, although some axial fluctuations were observed. The temperature and velocity increased with increasing applied current. The plasma core temperature is about 31,000, 34,000, 38,000, and 43,000 K at applied currents of 400, 500, 600, and 800 A, respectively. The maximum velocity inside the torch is about 1100, 1400, 1800, and 2400 m/s for applied currents of 400, 500, 600, and 800 A, respectively. The velocity varies significantly more with time than the gas temperature for applied currents of 600 and 800 A.

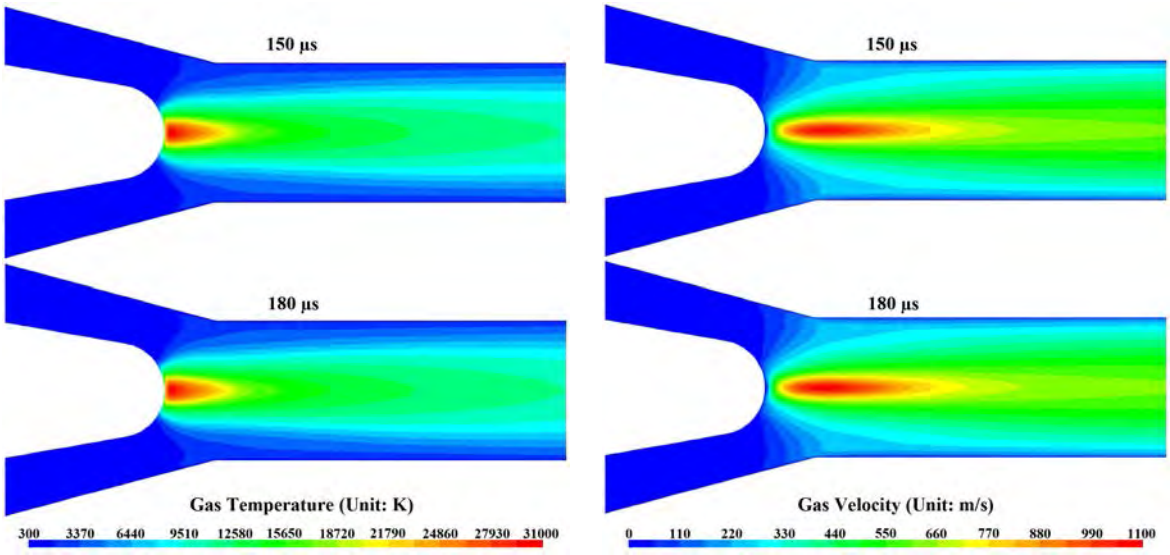


(a) (b)

Figure 3-35. (a) Instantaneous temperature and (b) velocity distributions inside the torch for an applied current of 400 A calculated by model 3.

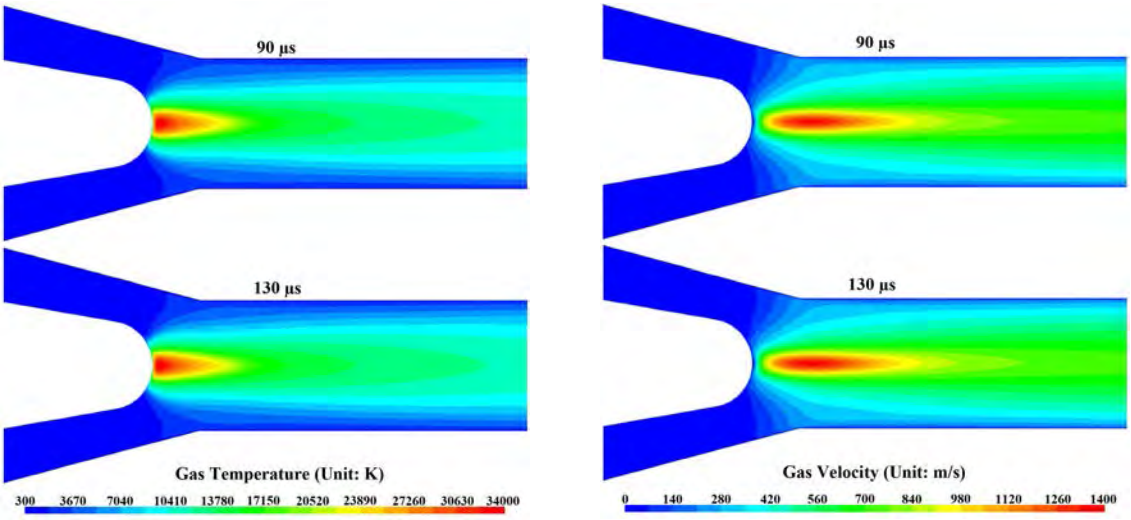


(a) (b)

Figure 3-36. (a) Instantaneous temperature and (b) velocity distributions inside the torch for an applied current of 500 A calculated by model 3.

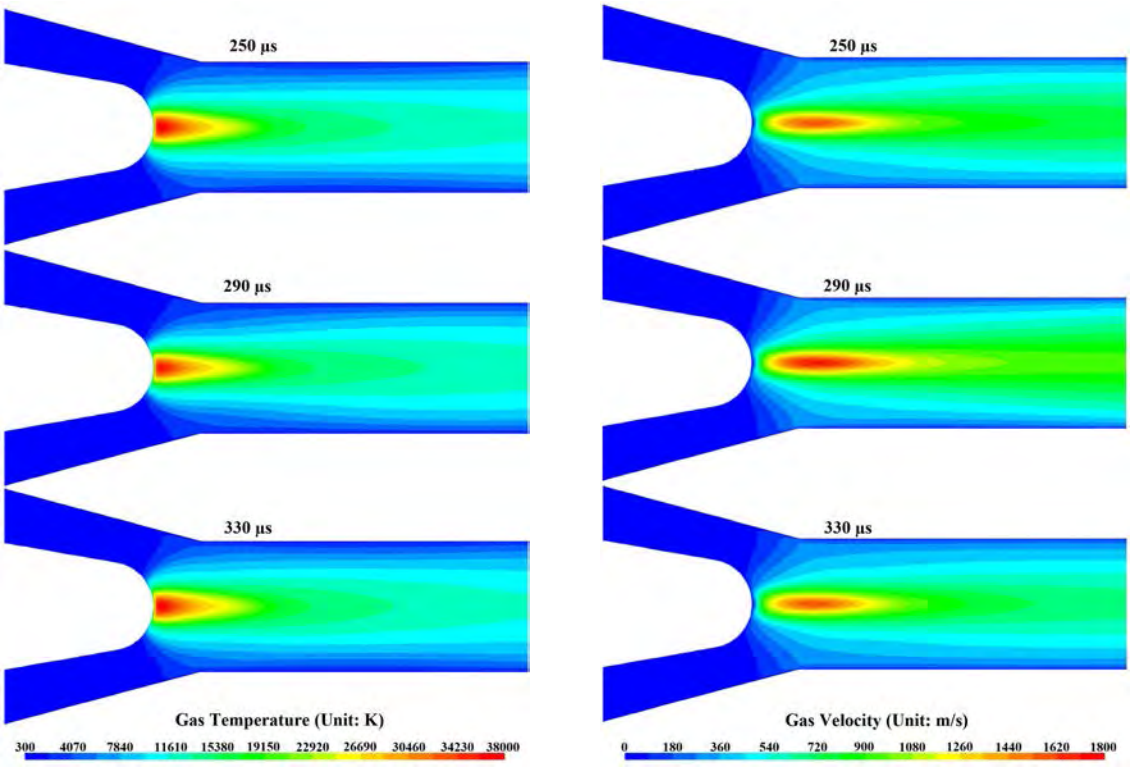


(a) (b)

Figure 3-37. (a) Instantaneous temperature and (b) velocity distributions inside the torch at the applied current of 600 A calculated by model 3.

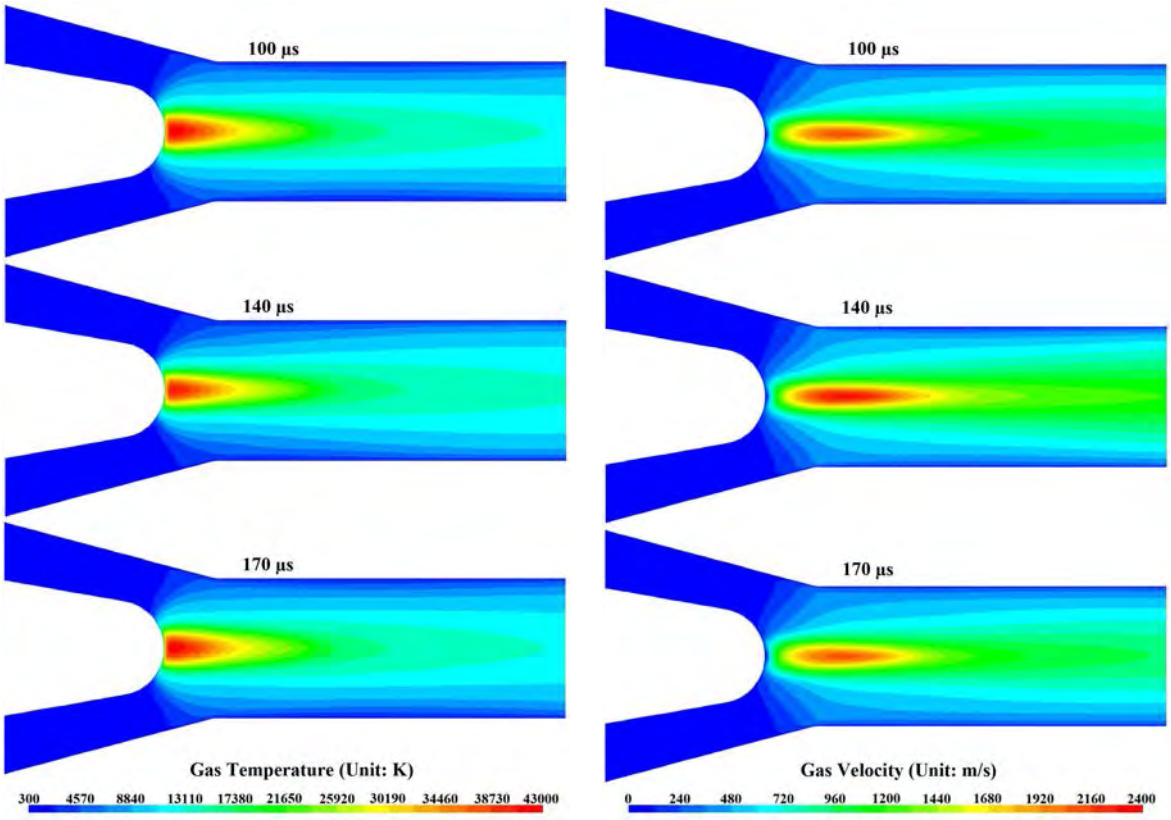


(a) (b)

Figure 3-38. (a) Instantaneous temperature and (b) velocity distributions inside the torch for an applied current of 800 A calculated by model 3.

**4) Arc voltage and electrical potential inside the torch**

Figure 3-39 shows the arc voltage calculated by model 3 for various applied currents. The arc voltage, which is determined by the electric current behavior inside the torch (see figure 3-34), remains almost constant with time for applied currents of 400 and 500 A, whereas it fluctuates periodically with time when the applied current exceeds 600 A. For a non-transferred DC plasma torch, the arc length depends on the balance between the flow drag force and the electromagnetic force. If the flow drag force greatly exceeds the electromagnetic force, the arc length will be longer and the electromagnetic force will be larger. The arc length will be shorter in the opposite case [12]. Since the arc voltage is almost proportional to the arc length, based on the arc length in figure 3-34, the arc voltage

increases with increasing applied current and arc voltage fluctuates for applied currents of 600 and 800 A (see figure 3-39). The arc voltages are about 20 and 22 V at applied currents of 400 and 500 A, respectively. The voltage amplitude is between 22.6 and 24.7 V with a fluctuation frequency of 13.9 kHz for an applied current of 600 A and it is between 25.8 and 28.4 V with a fluctuation frequency of 14.5 kHz for an applied current of 800 A.

Figure 3-40 shows the instantaneous electric potential distributions calculated by model 3 inside the torch. It reveals that the electric potential inside the torch fluctuates only for applied currents of 600 and 800 A, similar to the other parameters inside the torch. Similar to the results obtained with model 2, the electrical potential varies along the cathode interface despite the electric potential on the cathode being uniform. The plasma gas has a minimum electrical potential at the cathode tip. The electrical potential along the cathode surface is expected to decrease with increasing distance from the cathode tip due to the sheath voltage drop of the cathode, which is not considered in the present study. Therefore, the electrical potential of the gas at the cathode interface should equal the difference between the arc voltage and the sheath voltage drop. Benilov [31] and Zhou [32] found that increasing the temperature and the electric current density reduce the sheath voltage drop. Therefore, the minimum electrical potential was obtained at the cathode tip since the sheath voltage drop is a minimum there due to the current density and temperature having maximums. The electrical potential decreased along the cathode surface due to the reduction in the sheath voltage drop.

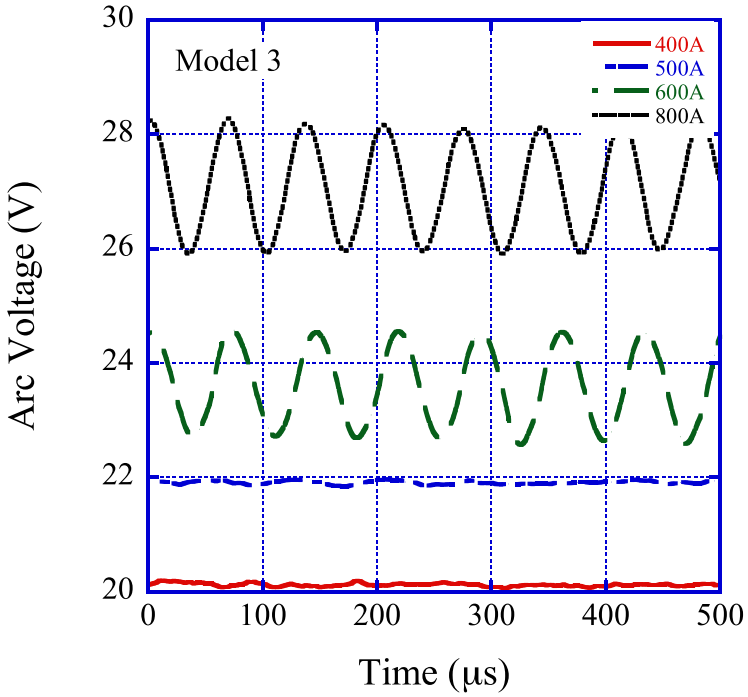


Figure 3-39. Arc voltage calculated by model 3.

**5) Gas flow at the torch exit**

Figure 3-41 shows the plasma gas temperature and velocity distributions at the torch exit for currents of 400, 500, 600, and 800 A obtained with model 3. It shows that, unlike the results obtained using models 1 and 2, all the plasma gas temperature and velocity distributions are nearly axisymmetric. The gas temperature and velocity remain almost constant with time for applied currents of 400 and 500 A, whereas they fluctuate with time for applied currents of 600 and 800 A due to variation of the parameters inside the torch. The gas temperature and velocity tend to increase with increasing applied current at the torch exit. The maximum temperature and velocity are obtained at the center of the torch exit. The maximum gas temperatures at the torch exit are about 11,500, 12,000, 12,500, and 13,500 K for applied currents of 400, 500, 600, and 800 A, respectively. The maximum gas velocities at the torch exit are about 620, 730, 920, and 1210 m/s for applied currents of 400, 500, 600, and 800 A, respectively.

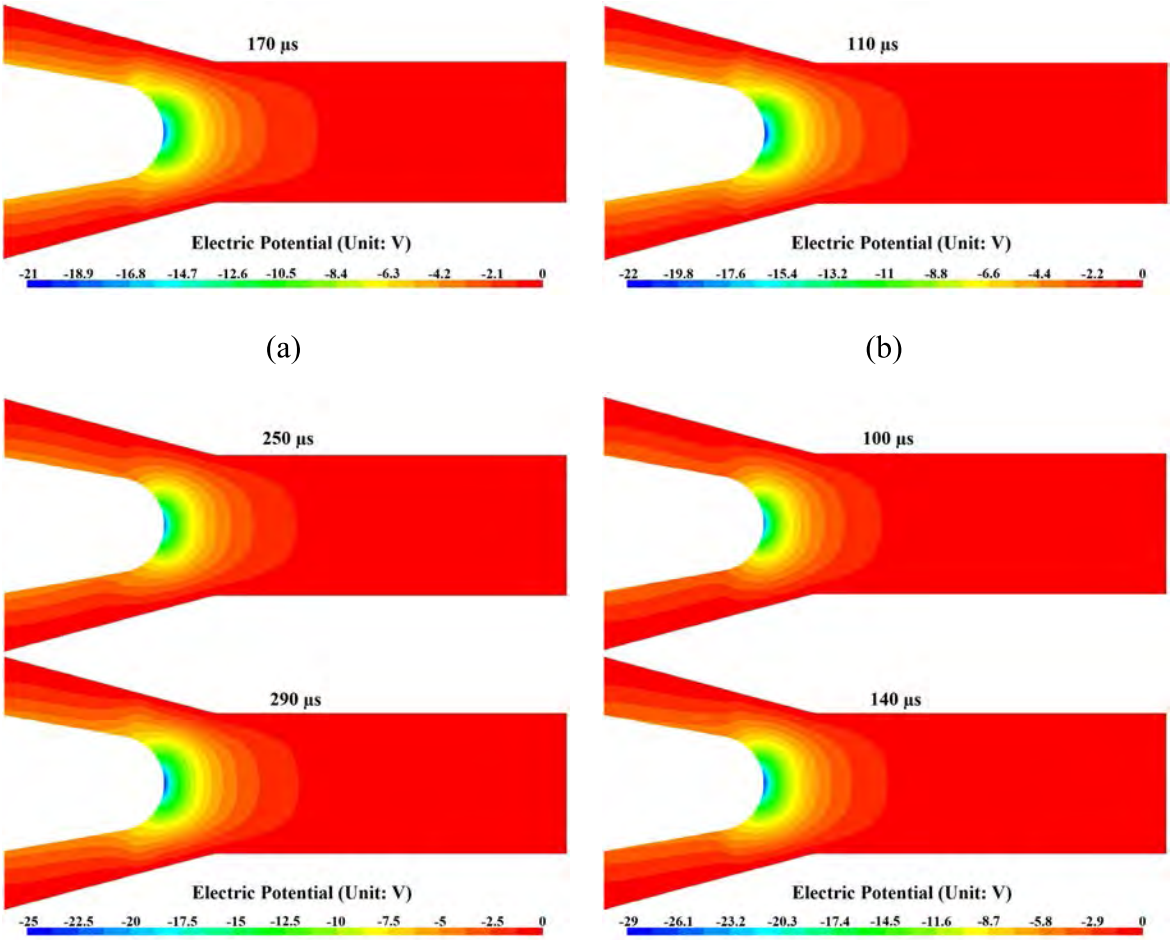


Figure 3-40. Instantaneous electric potential distributions inside the torch for applied currents of (a) 400, (b) 500, (c) 600 and (d) 800 A calculated by model 3.

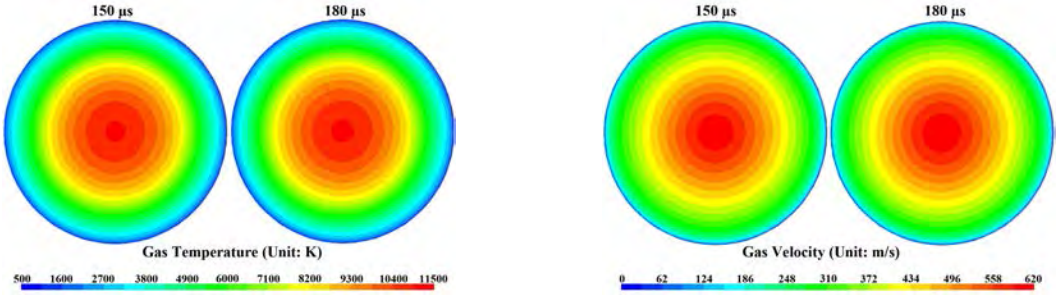


(a)

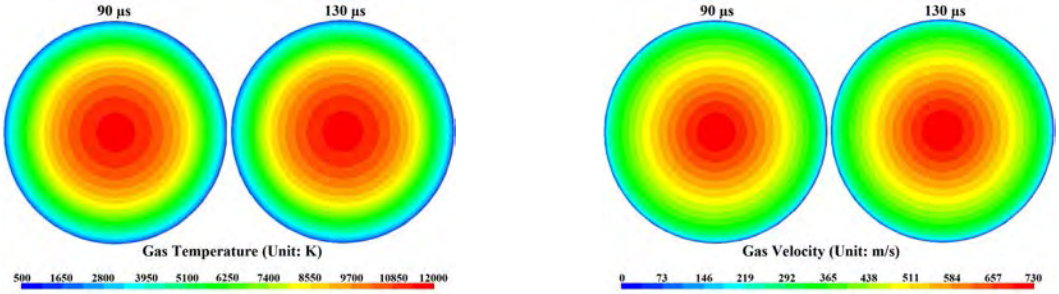


(b)

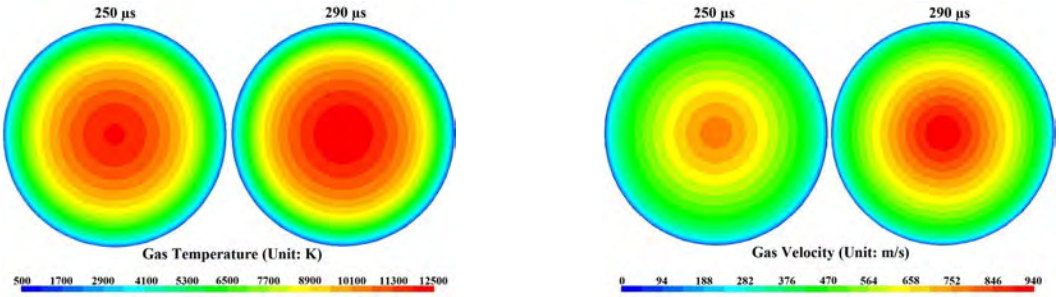


(c)

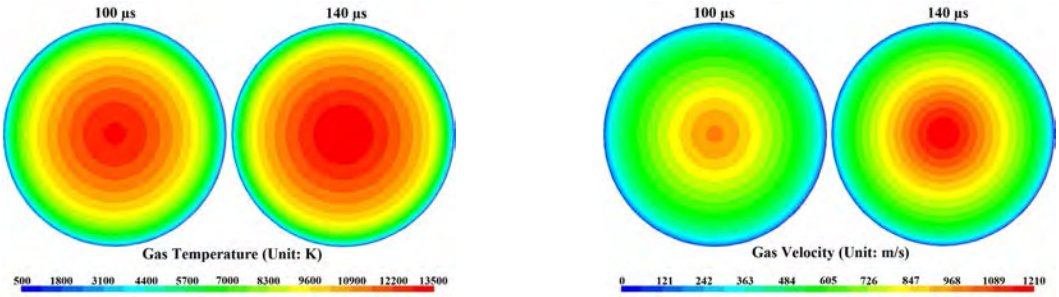


(d)

Figure 3-41. Gas temperature and velocity distributions at the torch exit for applied currents of (a) 400, (b) 500, (c) 600, and (d) 800 A calculated by model 3.

### 3.4.4 Discussions

The previous sections presented the results obtained with three LTE models for a plasma arc inside a plasma torch. The two conventional LTE models (models 1 and 2) effectively modeled the arc fluctuations inside the plasma torch. However, they gave higher arc voltages and arc lengths than those measured experimentally (see Chapter 2). The novel LTE model (model 3) cannot precisely model the arc fluctuations inside the plasma torch due to the calculated arc parameters having axisymmetric distributions. However, the arc voltages obtained with model 3 are much closer to the experimentally measured values given in Chapter 2. This section describes the characteristics of the three LTE models and compares their results with the experimental results.

**1) Gas temperature and velocity**

Sections 3.41–3.43 described the gas temperature and velocity inside the torch. The results reveal that for all three models the plasma gas temperature and velocity inside the torch fluctuate and that they increase with increasing applied current. Although the gas temperature and velocity distributions calculated by the three models differ slightly, they give similar temperatures and velocities inside the torch.

The average temperature and velocity profiles (i.e., the time-averaged values along the *x*- and *y*-axes) can be obtained from the temperature and velocity distributions at the torch exit. Figure 3-42 shows the average temperature and velocity profiles at the torch exit obtained with the three models for an applied current of 600 A. The average gas temperature and velocity at the torch exit calculated by model 1 are similar to those calculated by model 2. However, the average gas temperature and velocity at the torch exit calculated by model 3 are slightly lower than those calculated by the other two models because model 3 employed the nominal electron temperature.

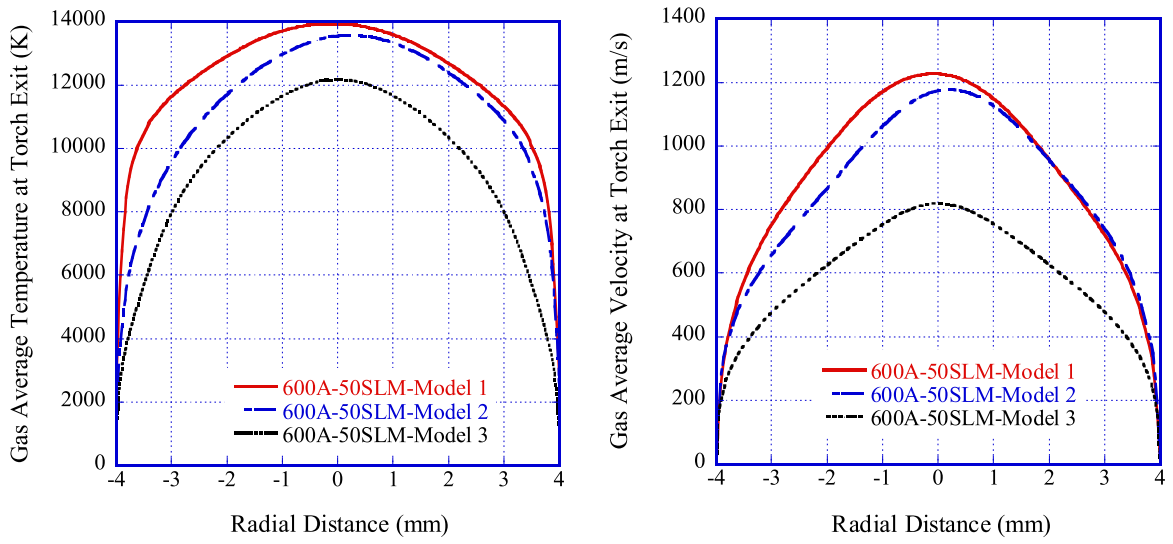


Figure 3-42. (a) Average temperature and (b) velocity of the plasma gas at the torch exit.

Figure 3-43 comparison of average temperature and velocity of the plasma gas at the torch exit obtained by model 3 for an applied current of 800 A with those reported by Trelles et al. [14]. Trelles et al. developed two models, LTE and NLTE models, to model the plasma gas flow inside a SG-100 plasma torch. The results reveal that the average gas temperature and velocity at the torch exit calculated by model 3 are intermediate between those obtained by the LTE and NLTE models developed by Trelles et al. Comparison with figure 3-42 shows that the gas temperature and velocity calculated by the conventional LTE model are higher than those obtained with the LTE model; the results obtained using the newly developed LTE model (model 3) effectively reduce the deviations of the gas temperature and velocity relative to those of the NLTE model.

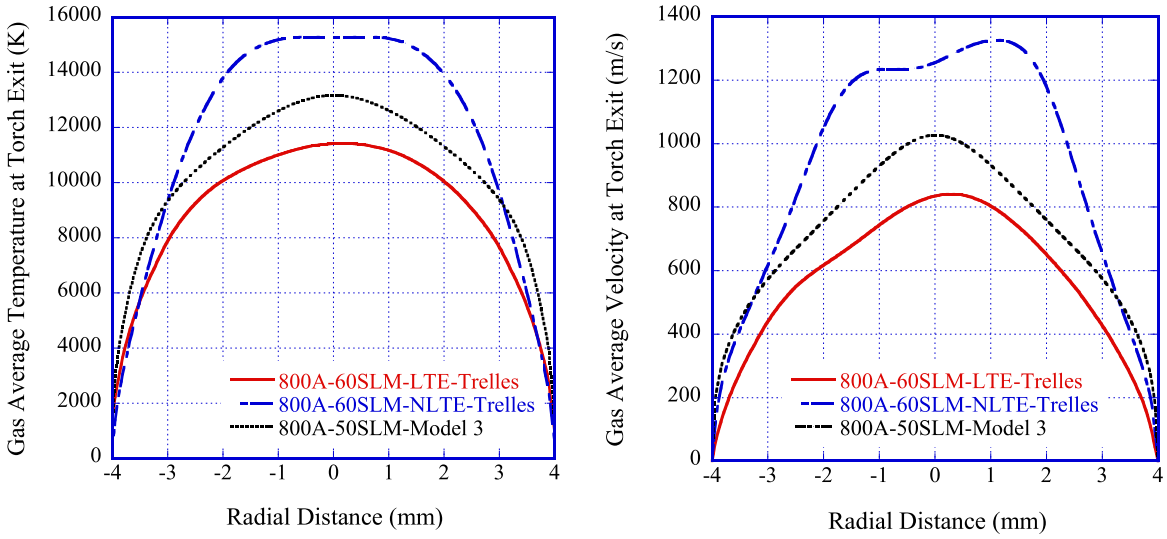


Figure 3-43. Comparison of the (a) average temperature and (b) velocity of the plasma gas at the torch exit with those reported by Trelles et al. [14].

**2) Arc voltage**

Figure 3-44 shows the time evolution of the arc voltage for an applied current of 600 A. It shows that the arc voltage obtained using model 2 has a higher fluctuation amplitude than those obtained using models 1 and 3 and that measured experimentally. The arc voltage calculated by model 1 is much higher than that measured experimentally; the value obtained with model 2 is a little closer to the experiment than that obtained with model 1, but it is still higher than that measured experimentally. The arc voltage obtained with model 3 is thought to be closer to the measured one due to the nominal electron temperature being applied in model 3. This is strongly supported by the fact that the arc behavior inside the plasma torch calculated by model 3 is close to the actual arc behavior when the electrical conductivity of the plasma gas is determined by the nominal electron temperature instead of the gas temperature.

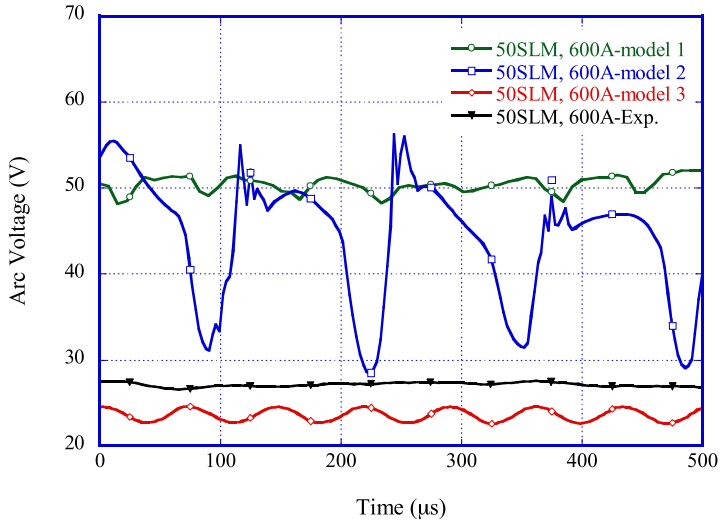


Figure 3-44. Time evolution of the arc voltage for an applied current of 600 A.

Figure 3-45 shows the time evolution of the arc voltage reported by Trelles et al. [14]. It shows that the results obtained with models 1 and 2 are similar to those obtained with the LTE model reported by Trelles et al. In addition, model 3 gives a similar arc voltage to the NLTE model reported by Trelles et al. Unlike the novel LTE model (Model 3) or the NLTE model reported by Trelles et al., the arc voltage obtained using conventional LTE model (Model 1 or 2 and the LTE model of Trelles et al) is much higher than the measured value. This is because the LTE assumption underestimates the electrical conductivity, especially near the electrodes. In contrast, the arc voltage calculated using model 3 is closer to the measured value. This is the evidence that Model 3 gives an improved estimate of the electrical conductivity when the nominal electron temperature is used instead of the gas temperature.

Figure 3-46 compares the arc voltage calculated by model 3 with the measured value. The arc voltage calculated by model 3 is very similar to the measured one. However, the measured time evolution of the arc voltage does not exhibit a constant fluctuation frequency, whereas a clear fluctuation frequency can be obtained from the calculated one. This may be due to the characteristics of the power supply used; the electric current supplied fluctuates over a large range with a frequency of 300 Hz (see figure 2-10),

whereas a constant electric current is used in the simulation. Therefore, the varying electric current is thought to be reason why the experimentally obtained arc voltage fluctuations do not exhibit a constant frequency. Figure 3-46 shows that the fluctuation amplitude of the measured arc voltage is smaller than that calculated with model 3.

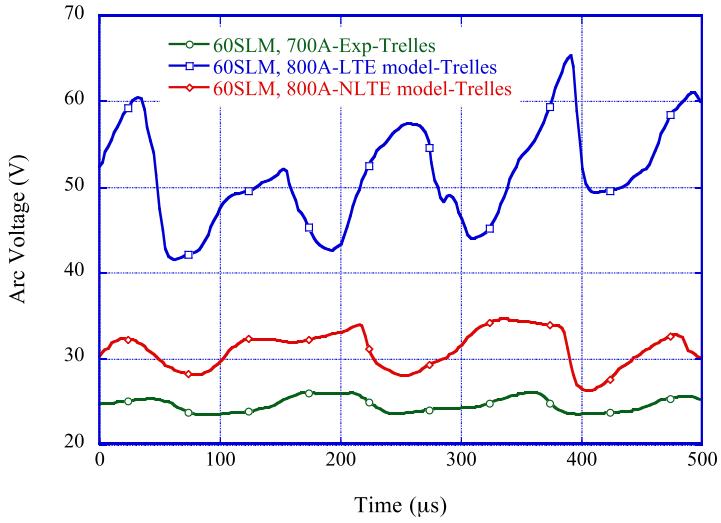


Figure 3-45. Time evolutions of arc voltage for an applied current of 800 A reported by Trelles [14].

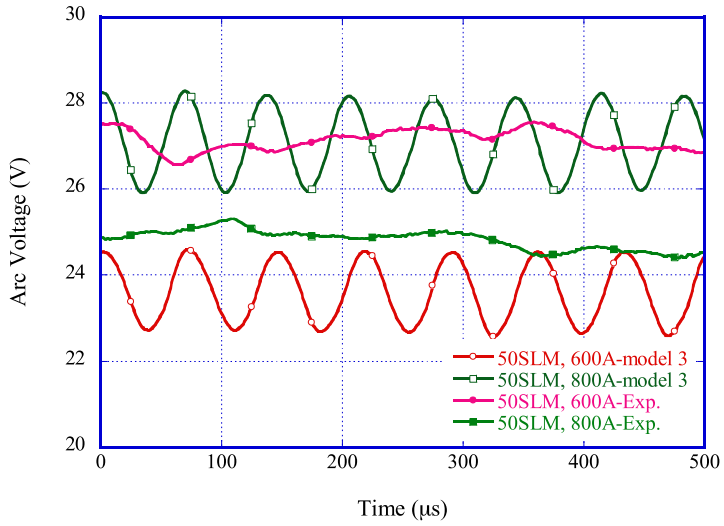


Figure 3-46. Comparison of arc voltage calculated by model 3 with those measured for applied currents of 600 and 800 A.

The average arc voltage can be determined from the obtained time evolutions of the arc voltage. Figure 3-47 shows the average arc voltage for different applied currents. It shows that the average voltages calculated by models 1 and 2 are much higher than the measured one. In contrast, the average arc voltage calculated by model 3 deviates only slightly from the measured one. As mentioned above, the deviations of the arc voltages calculated by models 1 and 2 from the measured one are mainly due to the models underestimating the electrical conductivity. The deviation of the arc voltage calculated by model 3 from the measured value is mainly caused by the sheath voltage drop of the electrodes, which was not considered in the present study. A suitable model should be developed that accounts for the sheath voltage drop, to make the calculated arc voltage closer to the actual one [31–36].

**3) Thermal energy of the plasma arc**

The amount of heat transferred to the plasma in the current simulation can be calculated by integrating the increase in the thermal energy at the surface of the torch exit. It is given by

$$Q_{plasma} = \iint c_p m_f (T - T_0) ds \qquad (Eq. 3-24)$$

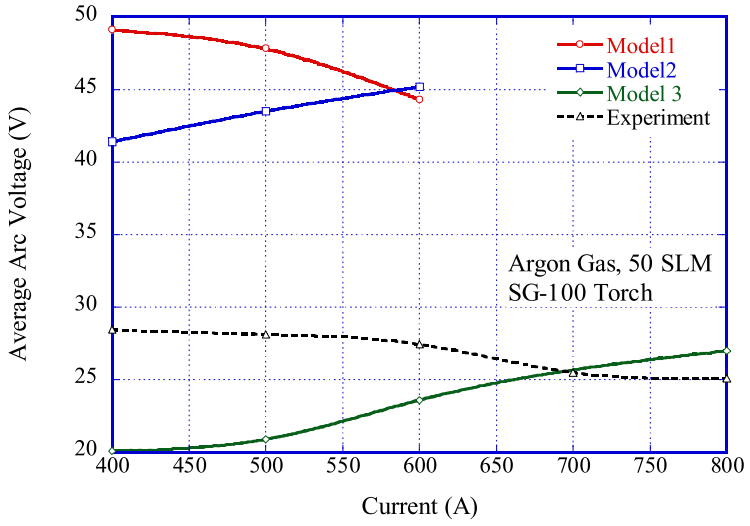


Figure 3-47. Average arc voltage

where $c_p$ is the specific heat of the gas, $m_f$ is the mass flow rate of the gas at an element at the torch exit, $T$ is the gas temperature, $T_0$ is the initial gas temperature at the nozzle inlet, and $s$ is the area of an element at the torch exit.

Figure 3-48 shows the calculated instantaneous heat transferred to the plasma for an applied current of 600 A. It shows that the heat transferred to the plasma fluctuates in a similar manner as the arc voltage. The time average of the heat energy of the plasma arc can be obtained from profiles of the instantaneous heat transferred to the plasma. Figure 3-49 shows the average thermal energy of the plasma arc. It shows that the thermal energy of the plasma arc increases with increasing applied current due to the increase in the input electrical energy. The average heat energy of the plasma arc obtained with models 1 and 2 is significantly larger than that measured experimentally. However, the average heat energy of the plasma arc obtained with model 3 is very similar to that measured experimentally. Model 3 appears to model the plasma arc inside the plasma torch more accurately than models 1 and 2.

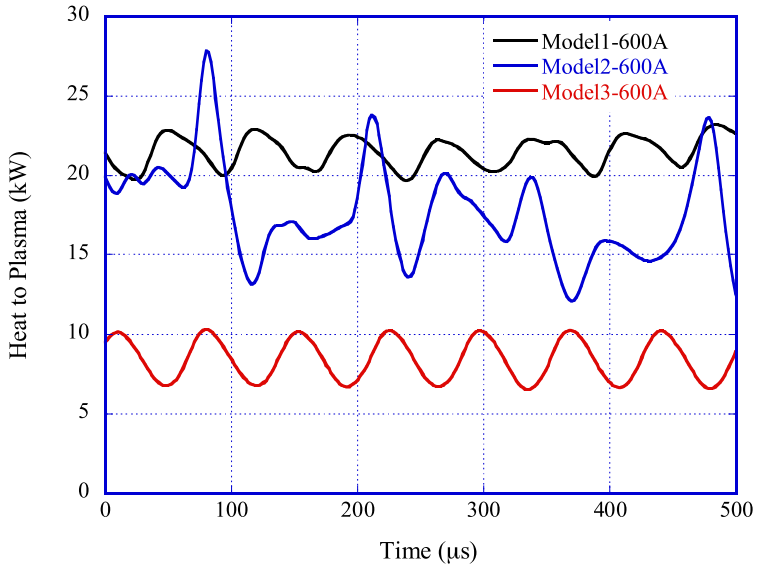


Figure 3-48. Time evolution of heat transferred to the plasma for an applied current of 600 A.

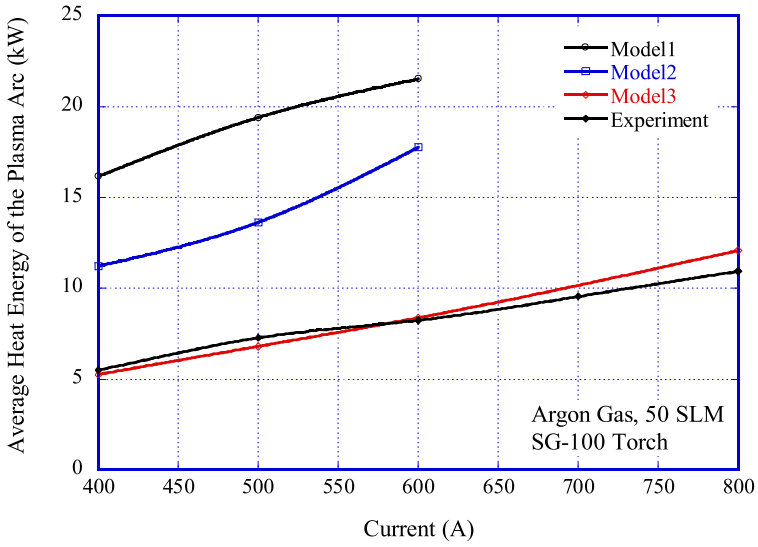


Figure 3-49. Average heat energy of the plasma arc.

**4) Electro-thermal efficiency of the plasma torch**

From the average arc voltage shown in figure 3-47, the input electrical energy can be calculated using

$$E_{input} = \overline{U}I \qquad (Eq.3-25)$$

Where $\overline{U}$ is the average arc voltage and $I$ is the applied current. From the results for the average heat energy shown in figure 3-49, the electrothermal efficiency can be obtained using

$$\eta(\%) = \frac{\overline{Q_{plasma}}}{E_{input}} \times 100\% \qquad (Eq.3-26)$$

Figure 3-50 shows the electrothermal efficiency. It shows that model 1 gave the highest efficiency, whereas the electrothermal efficiency obtained by model 2 was slightly lower, being closer to the experimental value. Model 3 gave the closest value to the experimental one. The efficiencies obtained by the numerical calculations are higher than that measured experimentally because the models in the present study did not consider the energy loss in the sheath.

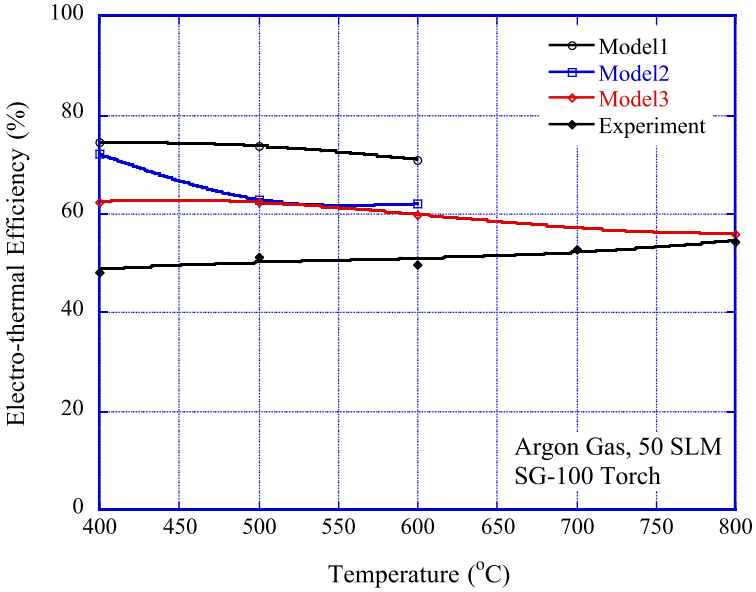


Figure 3-50. Electrothermal efficiency of the torch.

**5) Arc attachment position and anode erosion**

Based on the anode erosion shown in figure 2-14, it seems that anode erosion always occurs close to the corner of the internal surface of the anode. Therefore, the arc attachment is expected to be located in the annular area. The arc attachment obtained with model 1 is much farther downstream than that observed in experiment (see figure 3-22). Therefore, the automatically determined arc attachment position in model 1 deviates greatly from the actual location. When a breakdown electric field is applied in model 2, the arc attachment is a little closer to the actual location relative to that obtained with model 1 (see figure 3-26). It can also be seen that the arc attachment calculated by model 2 moved in a large range including the vicinity of the corner of the anode internal surface. When the nominal electron temperature is used in model 3, the position of the arc attachment is very close to that observed experimentally, even though the arc length varies with time or applied current (see figure 3-34). Comparison of the electrical current density distribution obtained with model 3 and the eroded anode reveals that anode erosion occurs in the region where the main electric current path passes (see figure 3-51). Thus, model 3 can accurately

predict the position of anode erosion by calculating the electric current density distribution.

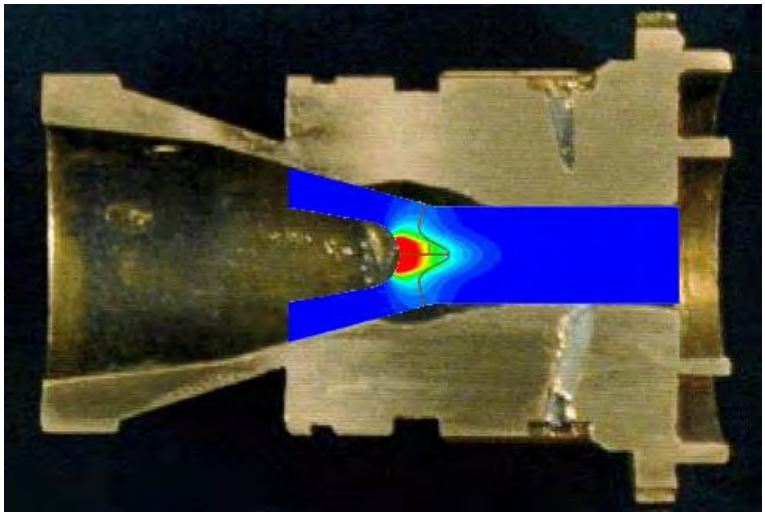

Figure 3-51. Electric current density distribution obtained with model 3 superimposed on a photograph of an eroded anode.

## References

[1]. Paik Seungho, Huang P. C., Heberlein J. and Pfender E., Determination of the Arc-Root Position in a DC Plasma Torch, Plasma Chemistry and Plasma Processing, Vol. 13, No. 3, 379-397, 1993.

[2]. Favalli R. C., Szente R. N., Physical and Mathematical Modeling of non Transferred Plasma Torches, Brazilian Journal of Physics, Vol. 28, No. 1, March, 1998.

[3]. Li He-Ping and Pfender E., Three Dimensional Modeling of the Plasma Spray Process, Journal of Thermal Spray Technology, Volume 16(2) June 2007, 245–260.

[4]. Selvan B. and Ramachandran K., Comparisons Between Two Different Three-Dimensional Arc Plasma Torch Simulations, Journal of Thermal Spray Technology, Volume 18(5-6) Mid-December 2009, 846–857.

[5]. Selvan B., Ramachandran K., Sreekumar K. P., Thiyagarajan T. K., Ananthapadmanabhan P. V., Three-Dimensional Numerical Modeling of an Ar-N2 Plasma Arc Inside a Non-Transferred Torch, Journal Plasma Science and Technology, IssueVolume 11, Number 6, 2009, 679-687.

[6]. Klinger L, Vos JB, Appert K, High-resolution CFD simulation of a plasma torch in 3 dimensions, Centre de Recherches en Physique des Plasmas – Preprint Report, LRP 763, 2003, http://crppwww.epfl.ch/.

[7]. Li He-Ping, Pfender E., Chen X., Application of Steenbeck's Minimum Principle for Three-dimensional Modelling of DC Arc Plasma Torches, J. Phys. D, V36, No.9, (2003), 1084-1096.

[8]. Baudry C., Vardelle A., Mariaux G., Delalondre F C., E. Meillot, Three-dimensional and time-dependent model of the dynamic behavior of the arc in a plasma spray torch, Thermal Spray 2004: Advances in Technology and Applications (ASM International), 717 – 723.

[9]. Moreau E., Chazelas C., Mariaux G. and Vardelle A., Modeling the Restrike Mode

Operation of a DC Plasma Spray Torch, Journal of Thermal Spray Technology, Volume 15, Number 4, 2006, 524-530.

[10]. Trelles J. P. and Heberlein J. V. R., Simulation results of Arc Behavior in Different Plasma Spray Torches, Journal of Thermal Spray Technology, Volume 15, Number 4 (2006), 563-569.

[11]. Trelles J. P., Finite Element Modeling of Flow Instabilities in Arc Plasma Torches, Ph. D. Thesis, University of Minnesota, 2007.

[12]. Trelles J. P., Pfender E. and Heberlein J. V. R., Modelling of the arc reattachment process in plasma torches, Journal of Physics D: Applied Physics, Volume 40, Number 18, 5635, 2007.

[13]. Trelles J. P., Pfender E. and Heberlein J., Multiscale Finite Element Modeling of Arc Dynamics in a DC Plasma Torch, Plasma Chem. Plasma Process (2006) V26, 557-575.

[14]. Trelles J. P., Heberlein J. and Pfender E., Non-equilibrium Modelling of Arc Plasma Torches, Journal of Physics D: Applied Physics, Volume 40, Number 19 (2007), 5937.

[15]. Porytskyy P.V., Mechanisms of the Contraction of an Arc Discharge. 1. Peculiarities of Thermal Contraction, Ukr. J. Phys., 2004. Vol. 49, No. 9.

[16]. Porytskyy P.V., Mechanisms of the Contraction of an Arc Discharge. 2. Peculiarities of the Contraction of a Low-Current Arc in the Mixture of a Noble Gas with Copper, Ukr. J. Phys., 2005. Vol. 50, No. 9.

[17]. Tan C. W., Soo N. L. ,and Bahadori M. N., Transport Properties of Non-Equilibrium Ionized Argon Gas, Zeitschrift für Angewandte Mathematik und Physik (ZAMP), Volume 16, Number 2, 255-278, 1965.

[18]. Zhukov M. F. and Zasypkin I. M., Thermal Plasma Torches: Design, Characteristics, Application, Cambridge Int Science Publishing, 2007.

[19]. Carlo Angelo Borghi, Discharges in the Inlet Region of a Noble Gas MHD Generator,

Thesis for Doctoral degree, Department of Electrical Engineering, Eindhoven University of Technology, Netherlands, 1982.

[20]. Miller Scott Alan, Viscous and diffusive effects in magnetoplasmadynamic flows, Thesis (M.S.)-Massachusetts Institute of Technology, Dept. of Aeronautics and Astronautics, 1990.

[21]. Tsuda Norio and Yamada Jun, Calculation of High-pressure Argon Plasma Parameter Produced by Excimer Laser, J. Plasma Fusion Res. SERIES, Vol.3 (2000) 605-608.

[22]. Boulos, M. I., Fauchais, P., and Pfender E., Thermal Plasmas: Fundamentals and Applications, Plenum Press, New York, 1994.

[23]. Haata Yoshisuke, gaseous discharge, Published by Kindai Kagaku sha Co. Ltd, 1968 (In Japanese).

[24]. Dean, J. A. (Edited), Lange's Chemistry Handbook Version 15th, published by McGraw-Hill, 1999.

[25]. Krascella N. L., Theoretical Investigation of the Composition and Line Emission Characteristics of Argon-tungsten and Argon-uranium Plasmas, Report of United Aircraft Corporation, 1969.

[26]. Hutten Mansfeld, On the thermal Rayleigh problem in partially ionized argon, Eindhoven, Technische Hogeschool, Doctor in de technische Wetenschappen Thesis, 1976. p 142.

[27]. Palmer T. A. and DebRoy T., Enhanced dissolution of nitrogen during gas tungsten arc welding of steels, Science and Technology of Welding & Joining, Volume 3, Number 4, August 1998 , pp. 190-203(14).

[28]. Colombo V., Ghedini E., Sanibondi P., Thermodynamic and transport properties in non-equilibrium argon, oxygen and nitrogen thermal plasmas, Progress in Nuclear Energy, V50 (2008), 921–933.

[29]. Rat V, Andre P, Aubreton J, Elchinger M F, Fauchais P and Vacher D, Transport

coefficients including diffusion in a two-temperature argon plasma, J. Phys. D: Appl. Phys, 35 (2002) , 981–991.

[30]. Rat V., Andre P., Aubreton J., Elchinger M. F., Fauchais P. and Lefort A., Transport properties in a two-temperature plasma: Theory and application, Physical Review E, Volume 64, Issue 2 (2001).

[31]. Benilov M. S., Understanding and modelling plasma-electrode interaction in high-pressure arc discharges: a review, J. Phys. D: Appl. Phys. 41 (2008), p1-30.

[32]. Zhou X. and J. Heberlein, Analysis of the arc-cathode interaction of free-burning arcs, Plasma Source Sci. Technol. 3 (1994), p564-574.

[33]. Benilov M. S. and A Marotta, A model of the cathode region of atmospheric pressure arcs, J. Phys. D: Appl. Phys. 28 (1995), p1869-1882.

[34]. Zine B., D.Saifaoui, A.Dezairi, T.Es-sabbar, A.Boumhali, M.ElMouden1, Modelling of Collision in the Plasma Sheath and the Cathode Erosion of Electrical Arc, M. J. Condensed Matter, Volume 6, Number 1, p 26-34, 2005.

[35]. Sheridan T. E. and J. Goree, Collisional plasma sheath model, Phys. Fluids B, 3(10), p 2796-2804, 1991.

[36]. Li He-Ping and M S Benilov, Effect of a near-cathode sheath on heat transfer in high-pressure arc plasmas, J. Phys. D: Appl. Phys., 40, p 2010–2017, 2007.

# Chapter 4
# Simulation of Plasma Jet outside a Plasma Spray Torch

## 4.1 Introduction

In chapter 3, the gas temperature and velocity distributions at the torch exit were obtained by numerical calculations. The two conventional LTE models can effectively model the arc fluctuation inside the plasma torch. However, the calculated arc lengths are greater than that observed experimentally and the calculated arc voltages are much higher than the measured one. The gas temperature and velocity obtained by the two conventional LTE models are considerably higher than those obtained with the NLTE model. Consequently, the calculated thermal energy of the plasma arc is much higher than the measured value. The newly developed LTE model reduces the discrepancy from the experimentally measured results. Even though it cannot completely model the arc fluctuations in a plasma torch, the calculated arc voltage, gas temperature and velocity, arc length, and heat energy of plasma arc exhibit a similar accuracy to those obtained by the NLTE model. Furthermore, the results obtained by the novel LTE model are very similar to experimentally measured plasma arc parameters. Apart from arc fluctuations inside a plasma torch, the novel LTE model is much more suitable for predicting arc behavior than the two conventional LTE models, especially for the steady state. Since the torch outlet is the origin of the plasma jet, the boundary conditions of the plasma jet are determined by the plasma arc parameters at the torch outlet. Therefore, Using the results obtained with model 3 as the boundary conditions is more suitable than that of models 1 and 2 for accurately predicting the behavior of a plasma jet outside a plasma torch in a steady state.

Plasma jets always fluctuate (see chapter 2), but it is difficult to reproduce these fluctuations by numerical analysis because they are caused not only by arc fluctuations

inside the plasma torch, but also by the injection of the powder-feeding gas or the involvement of the ambient gas. The predictions for steady-state (time-averaged) plasma jets are sufficient for guiding the plasma spray process. In this chapter, the gas temperature and velocity profiles at the plasma torch exit obtained using the novel LTE model are employed as the boundary conditions in plasma jet simulations. A steady-state 3D model are used to calculate the gas flow field of the plasma jet and the in-flight particle trajectories, temperature, and velocity are investigated with the aim of using plasma spray processing to prepare coatings with excellent properties.

## 4.2 Background to Plasma Jet Simulations

The two key parameters that determine the properties of coatings produced by plasma sprays are the particle velocity and temperature in the plasma jet. Consequently, many studies have investigated plasma jets in plasma sprays. In particular, plasma jet characteristics and the behavior of injected particles have been extensively studied numerically.

Borisov et al. [1] developed a model for simulating subsonic turbulent plasma jets generated by plasma spray torches and the behavior of sprayed particles in such jets. The calculated results showed reasonable agreement with measurements. Bolot et al. [2] modeled plasma jets using two commercial CFD packages, PHOENICS and FLUENT. They describe some differences regarding the ways in which these two codes solve this type of problem. Wang et al. [3] described the mole fractions of different species, the temperature, and the velocity in a multicomponent plasma jet using the eddy dissipation model and a realizable $k$–$\varepsilon$ turbulence mathematical representation. Their results revealed that the eddy dissipation model is useful for predicting the various chemical reactions that occur in a multicomponent plasma gas, including recombination of dissociative atoms and ions, charge exchange reactions, and nitrogen and oxygen dissociation. Ramachandran and Nishiyama [4] developed a fully coupled 3D model to clarify two-way interactions

between plasma and particles in terms of energy, momentum, and turbulence. Plasma–particle two-way interactions were modeled by adopting a Lagrangian approach for particle behavior and an Eulerian approach for plasma flow. The effects of each two-way interaction on energy and momentum transfer and turbulence modulation were investigated by numerical simulations. Particles in the plasma jet cause local deformations of the plasma jet kinetic energy and its dissipation rate fields. Kang et al. [5] developed numerical models using the CFD program FLUENT and used them to investigate the effect of a substrate on the behavior of the plasma flow fields and in-flight particles. Their results revealed that although a perpendicular or inclined substrate significantly affects plasma flow fields near the substrate, the particle behavior was relatively unaffected. The insignificant effect of the substrate on particle behavior was qualitatively verified by experimental observations using SprayWatch imaging diagnostic system. Xiong et al. [6] used a 3D computational model, LAVA-P-3D, to investigate air entrainment in plasma jets and metal particle oxidation by entrained oxygen. They obtained good agreement with experimental data. Li and Chen [7] developed a 3D model for a turbulent thermal plasma jet with a transversely injected carrier gas and metal particles at atmospheric pressure. They employed the standard $k$–$\varepsilon$ model together with momentum and energy continuity equations to numerically simulate turbulent plasma flow. An improved particle stochastic-trajectory model was used in the calculations to predict the motion of injected particles in the turbulent flow field. The heating histories of the injected particles during their movement were also calculated. The modeling results revealed it is very important to include the effect of the carrier gas on the jet and particle behaviors. Transverse injection of the carrier gas deflected the plasma jet from its geometrical axis; the particle trajectories were also appreciably altered by carrier gas injection. The particles dispersed about their average trajectories in the turbulent flow field. Furthermore, Li and Pfender [8] realized more accurate prediction of 3D temperature and flow fields inside and outside of a DC arc plasma torch for transverse particle and carrier gas injection into the plasma jet. The 3D

trajectories and heating histories of the particles were predicted from the computed plasma temperature and flow fields.

Most of the previous studies of plasma jets focused on the gas flow field of a plasma jet and the behavior of the injected particles. The boundary conditions for the plasma jet inlet are almost always derived using an empirical formula or experimental results. This chapter uses the calculation results for the plasma torch exit presented in the previous chapter to calculate the gas flow field of a plasma jet and the behavior of the injected particles. This was done to predict the behavior a plasma jet and to enable better control of plasma spraying. The results for a plasma jet confirm the validity of the results obtained for a plasma arc inside a plasma torch.

## 4.3 Mathematical Formulation of a Plasma Jet

### 4.3.1 Assumptions

After simulating a plasma torch, a plasma jet can be calculated for the results at the plasma torch exit. This study models the gas flow field of a plasma jet outside a plasma torch and the particle behavior. The main assumptions used in this study are as follows:

(1) The plasma jet flow is quasi-steady and turbulent and has temperature-dependent properties.

(2) The plasma jet is in local thermodynamic equilibrium (i.e., the temperatures of the gas atoms, ions, and electrons at a point are the same) allowing it to be characterized by a single temperature.

(3) The plasma jet flow is in an optically thin, compressible, and steady system.

(4) An argon plasma jet is injected into argon gas (rather than air) at atmospheric pressure.

(5) The effect of ionization reactions of atomic argon resulting from dissociative reactions in the gas field of the plasma jet can be ignored.

(6) The effect of the carrier gas on the plasma jet can be neglected.

(7) The particles in the plasma jet are spherical. The temperature distributions within the particles are uniform. The latent heat of the particles can be neglected.

(8) The injected particles have negligible effects on the plasma jet characteristics, and particle–particle interactions are negligible; this is reasonable for a low-particle loading rate.

(9) The effect of gravity on the particles is negligible.

### 4.3.2 Governing equations

Based on the above assumptions, the governing equations for a 3D steady gas flow of a plasma jet can be written as:

Conservation of mass:

$$\nabla \cdot \left(\rho \vec{V}\right) = 0 \qquad (Eq.4-1)$$

Conservation of momentum:

$$\rho\, \vec{V}.\nabla \vec{V} = -\nabla \left[P + \tfrac{2}{3}\mu\left(\nabla \cdot \vec{V}\right)\right] + 2\nabla \cdot (\mu \overleftrightarrow{S}) \qquad (Eq.4-2)$$

Conservation of energy:

$$\rho c_p \vec{V}.\nabla T = \nabla \cdot (\lambda \nabla T) - S_r \qquad (Eq.4-3)$$

where $\rho$ is the gas mass density, $\vec{\mathrm{V}}$ is the gas velocity, $P$ is the gas pressure,, $\mu$ is the dynamic viscosity, $\overleftrightarrow{S}$ is the strain rate tensor, $c_p$ is the specific heat at constant pressure, $T$ is the gas temperature, $S_r$ is the volumetric net radiation losses, and $\lambda$ is the thermal conductivity of the gas..

Lagrangian equations of motion and heat balance are used to simulate particle behavior in a plasma jet. The governing equations for a particle in a plasma jet can be written as follows:

Particle velocity:

$$m_p \frac{d\vec{V_p}}{dt} = \frac{1}{2} C_d \rho \left|\vec{V} - \vec{V_p}\right| \left(\vec{V} - \vec{V_p}\right) \cdot \frac{\pi}{4} d_p^2 \qquad (Eq.4-4)$$

Particle temperature:

$$m_p c_p \frac{dT_p}{dt} = h\left(T - T_p\right) \cdot \pi d_p^2 \qquad (Eq. 4-5)$$

where $m_p$ is the mass of a particle,, $\vec{V_p}$ is the particle velocity, $C_d$ is the drag coefficient, $\rho$ is the gas density, $\vec{V}$ is the gas velocity, $d_p$ is the particle diameter, $c_p$ is the specific heat of a particle, $T_p$ is the temperature of a particle, $h$ is the heat transfer coefficient, and $T$ is the gas temperature.

The drag coefficient is given by [9]:

$$C_d = \alpha_1 + \frac{\alpha_2}{Re} + \frac{\alpha_3}{Re^2} \qquad (Eq. 4-6)$$

Where *Re* is the relative Reynolds number, which is defined as:

$$Re = \frac{\rho d_p \left|\vec{V} - \vec{V_p}\right|}{\mu} \qquad (Eq. 4-7)$$

The $\alpha$ coefficients are given by:

$$\alpha_1, \alpha_2, \alpha_3 = \begin{cases} 0, 24, 0 & 0 < Re < 0.1 \\ 3.69, 22.73, 0.903 & 0.1 < Re < 1 \\ 1.222, 29.1667, -3{:}8889 & 1 < Re < 10 \\ 0.6167, 46.50, -116.67 & 10 < Re < 100 \\ 0.3644, 98.33, -2778 & 100 < Re < 1000 \\ 0.357, 148.62, -47500 & 1000 < Re < 5000 \\ 0.46, -490.546, 578700 & 5000 < Re < 10000 \\ 0.5191, -1662.5, 5416700 & Re \geq 10000 \end{cases} \qquad (Eq. 4-8)$$

The heat transfer coefficient $h$ is deduced from the Nusselt number $N_u$, which is evaluated from the well-known Ranz–Marshall correlation [10].

$$N_u = \frac{h d_p}{\lambda} = 2.0 + 0.6 Re^{0.5} Pr^{0.33} \qquad (Eq. 4-9)$$

where *Pr* is the Prandtl number of the gas.

### 4.3.3 Computational domain and boundary conditions

Figure 4-1 shows the computational domain of the plasma jet used in the study. It is discretized using structured hexahedral cells with 133,285 nodes and 129,360 cells.

To allow the boundary conditions to be specified, the computational domain is divided into four faces: gas inlet, nozzle wall, atmospheric boundary, and gas outlet.

Fluent 6.3 was used to calculate the gas flow field of the plasma jet. The temperature and velocity profiles of gas inlet boundary are obtained from the simulation results of Model 3 at the plasma torch exit presented in Chapter 3. The nozzle wall is considered to be an adiabatic boundary. The gas outlet is regarded as a free outlet to the atmosphere. In addition, the atmospheric boundary is defined as an open boundary through which gas flow can pass depending the gas pressure. The $k$–$\varepsilon$ model is utilized in the current simulation and the governing equations are solved by the SIMPLE algorithm.

The particles are fed from the edge of the plasma torch with only an initial radial velocity; the particle injection position is shown in figure 4-2. Acceleration and heating of the in-flight particles are computed using the discrete phase model (DPM) in Fluent [11].

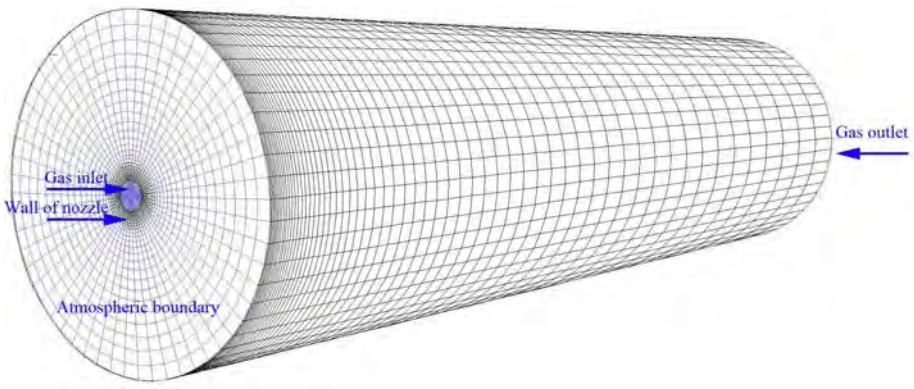


Figure 4-1. Computational domain and mesh of a plasma jet.

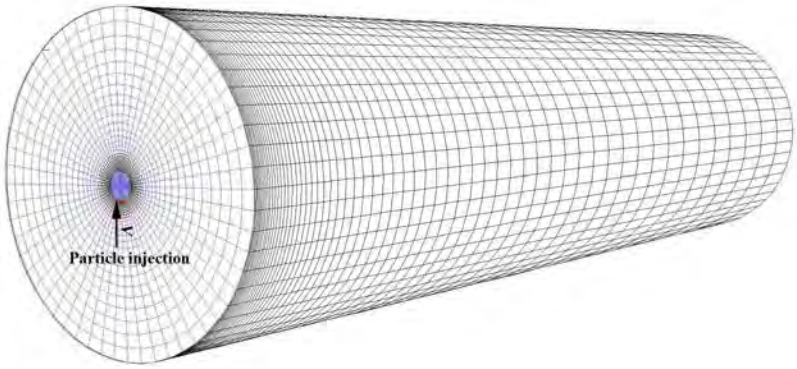


Figure 4-2. Particle injection position.

### 4.3.4 Spray conditions in simulation

In contrast with the different results given in Chapter 3 obtained for a plasma torch using the three LTE models, the results obtained using model 3 agree well with the experimental results, especially for the steady state (time-average). Therefore, the time-averaged gas temperature and velocity at the torch exit calculated by model 3 were used as the gas inlet boundary conditions for the domain shown in figure 4-1. Table 4-1 lists the spray conditions for the plasma jet simulations. Currents of 400, 500, and 600 A were applied. Figure 4-3 shows the corresponding boundary conditions of the gas inlet based on the results in Chapter 3. The same plasma gas properties were used as those described in Chapter 3 because the same gas was used in the plasma jet simulations.

Table 4-1. Spray conditions used in plasma jet simulation

| | |
|---|---|
| Plasma gas | Argon |
| Torch | SG-100 |
| Gas flow rate (SLM) | 50 |
| Applied Current (A) | 400, 500, 600 |

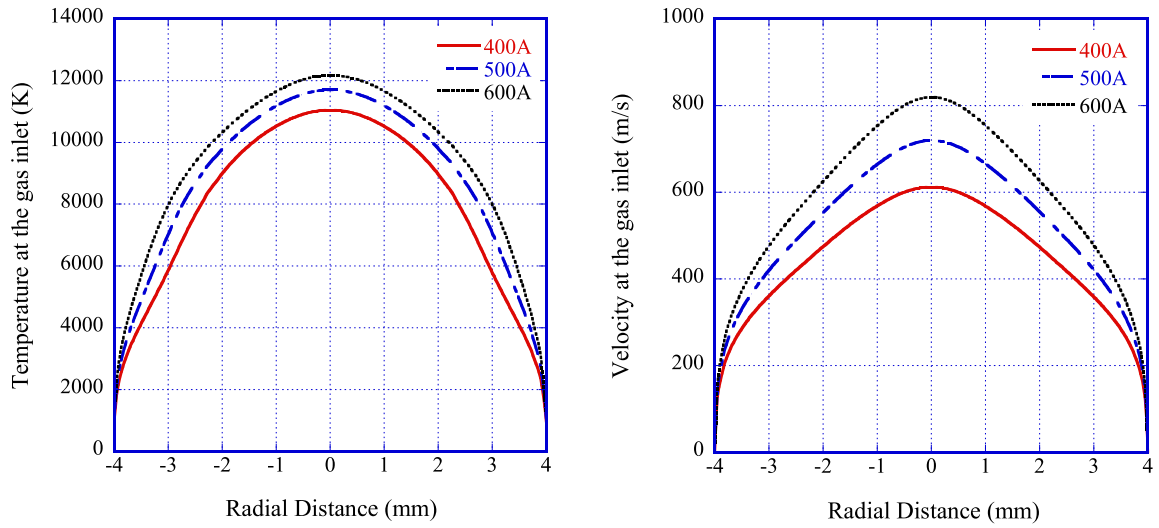


(a) (b)

Figure 4-3. Gas temperature and velocity at the gas inlet.

Alumina particles were used as the feedstock to calculate the in-flight particle temperature and velocity. Table 4-2 lists the properties of alumina. Particles with diameters in the range 20 to 40 μm are fed from the particle injection position. The initial radial velocities of particles were set to be 5, 10, and 20 m/s, while the axial velocity was set to zero.

## 4.4 Temperature and Velocity Distributions of Plasma Jet

### 4.4.1 Gas flow of plasma jet

Figure 4-4 shows the calculated gas temperature distributions of the plasma jet for the conditions described above. It shows that the plasma jet temperature and length increase with increasing applied current. The gas temperature decreases with increasing distance from the gas inlet; this is independent of the applied current due to the involvement of the surrounding gas (see figure 4-4). The gas temperature of the plasma jet tends to increase with increasing applied current due to the increase in the input electrical power.

Table 4-2. Properties of particles utilized in simulation

| Particle name | $Al_2O_3$ |
|---|---|
| Density ($kg/m^3$) | 3900 |
| Specific heat (J.kg/K) | 1340 |
| Thermal conductivity [w/(m.K)] | 6.55 |

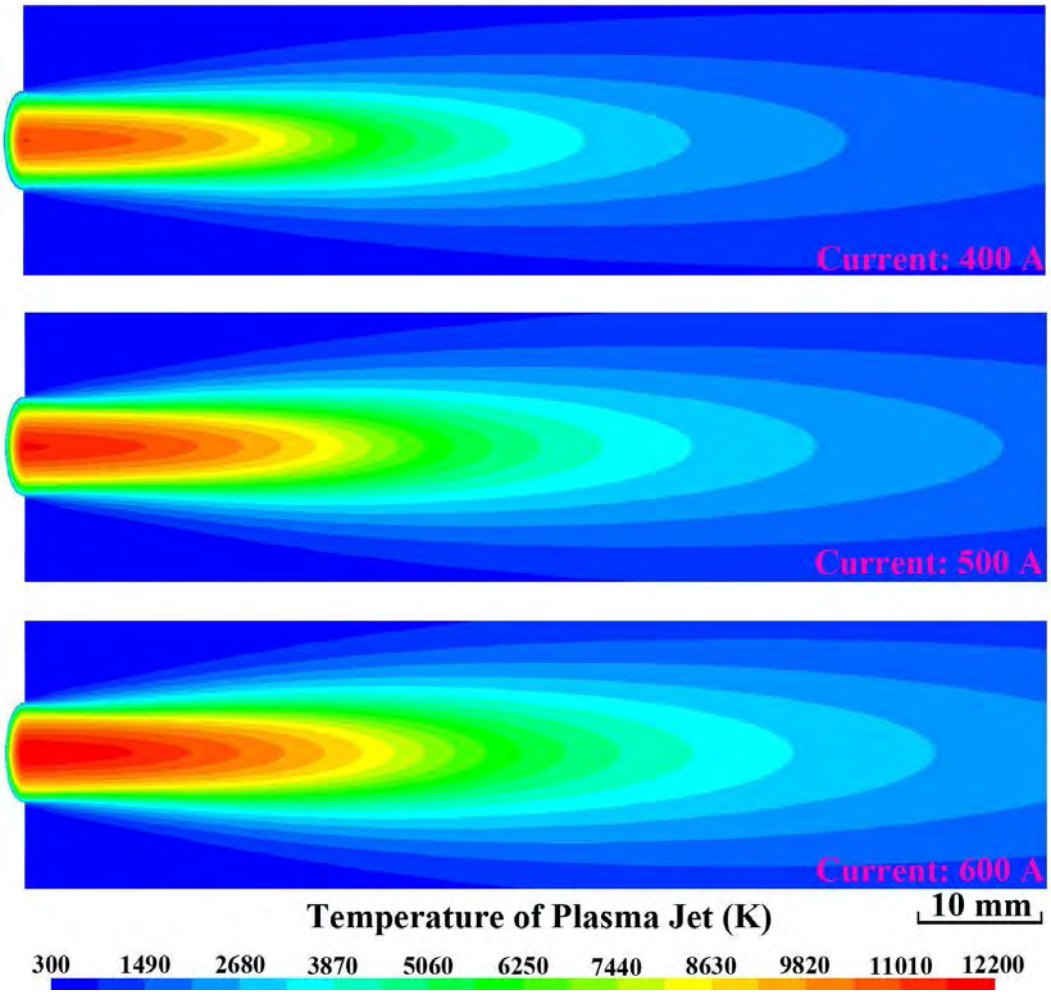


Figure 4-4. Gas temperature of the plasma jets at different applied current.

Figure 4-5 shows the calculated gas velocities of the plasma jet for different applied currents. Similar to the gas temperature, the input electrical power greatly affects the gas velocity because the gas velocity increases with increasing applied current. Comparison of

figures 4-4 and 4-5 suggests that the input electrical power affects the particle velocity more significant than that of the gas temperature. The gas velocity also decreases with increasing standoff distance due to the effect of the surrounding gas.

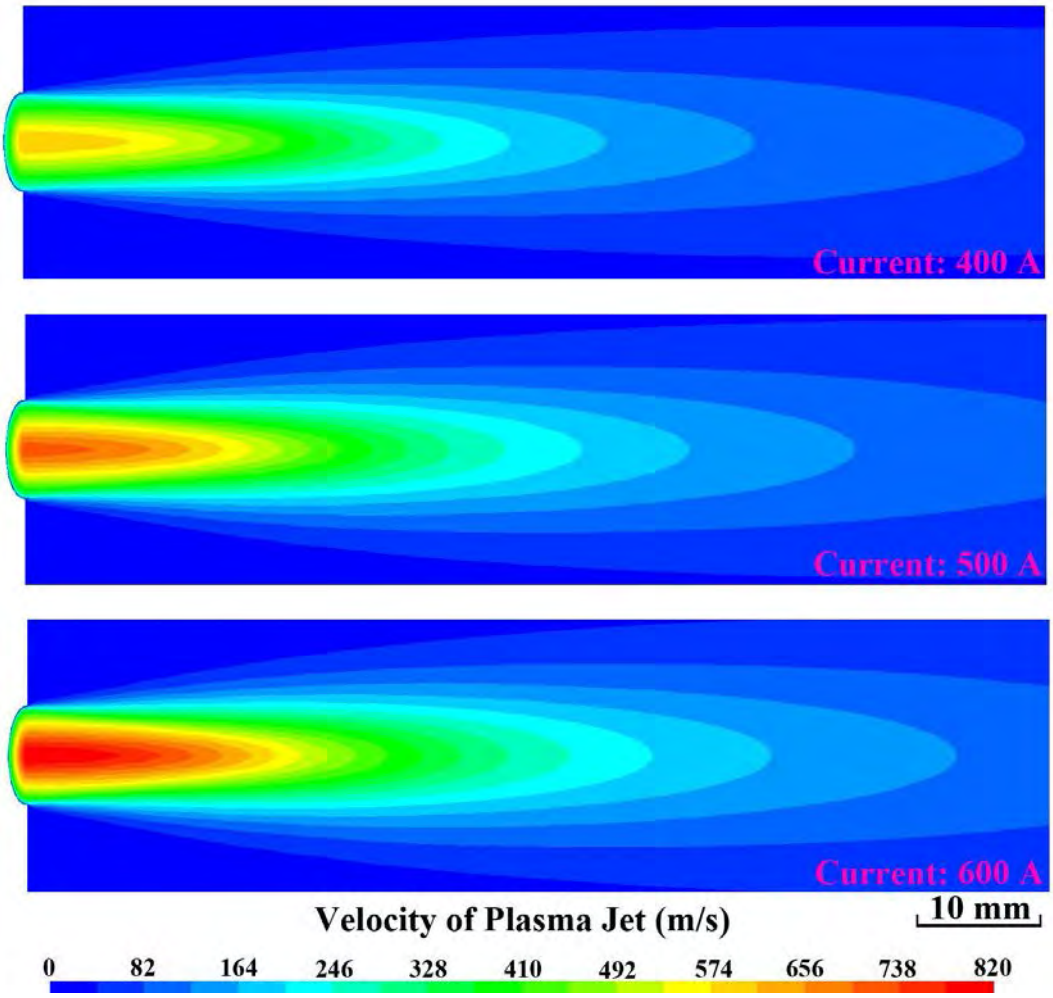


Figure 4-5. Gas velocity distribution of a plasma jet for three applied currents.

### 4.4.2 Particle temperature and velocity in plasma jet

Figure 4-6 shows the particle trajectories in the plasma jet for different particle diameters and initial velocities. It shows that the particle trajectories depend on the particle diameter and initial velocity. The particle trajectories are superimposed on the gas temperature distribution of the plasma jet in figure 4-6(b). It shows that the particles travel in different regions in the plasma jet; consequently, the particles are accelerated and heated by different amounts.

Figure 4-7 shows the in-flight particle temperature and velocity along the standoff distance for an applied current of 500 A. It shows that the particle temperature and velocity increase for standoff distances below 30 mm and decrease for standoff distances greater than 30 mm. Due to this variation in particle trajectories, higher particle temperatures and velocities were obtained at certain initial radial velocities (e.g., 20 m/s); this is attributed to particles residing longer in the gas field of high temperature and velocity at these initial radial velocities, giving them higher temperatures and velocities. During their flight in the plasma jet, larger particles are heated to higher temperatures, whereas smaller particles are accelerated to higher velocities near the torch exit and decelerated much more rapidly when the particle velocity exceeds the gas velocity due to their lower inertia.

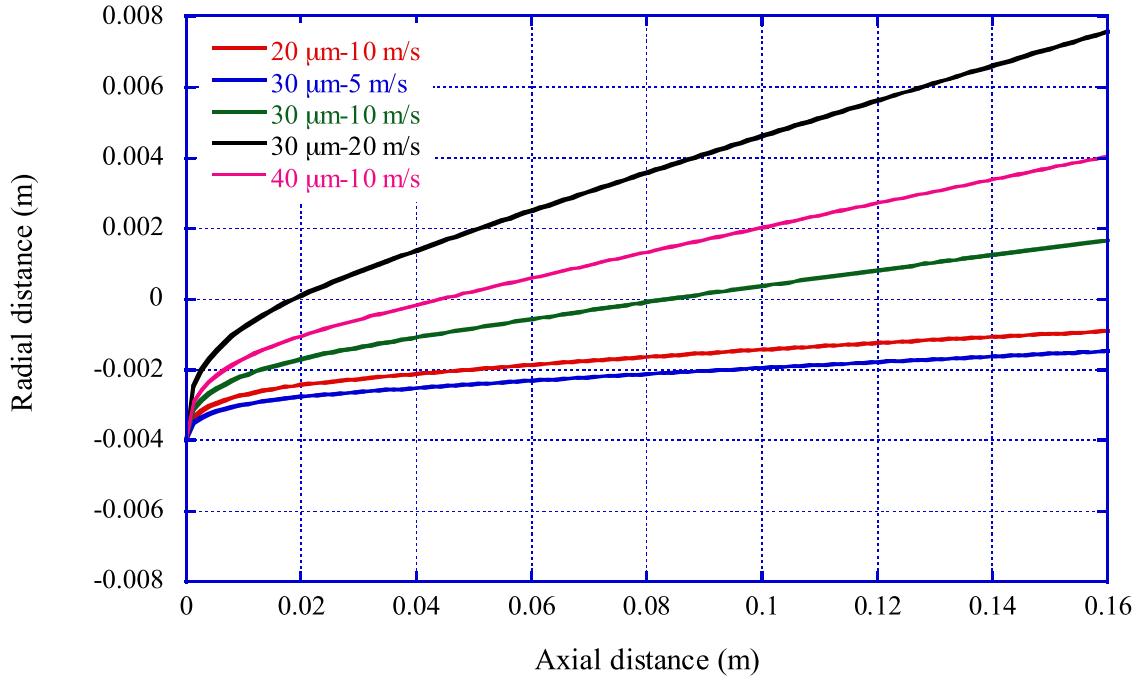


(a)

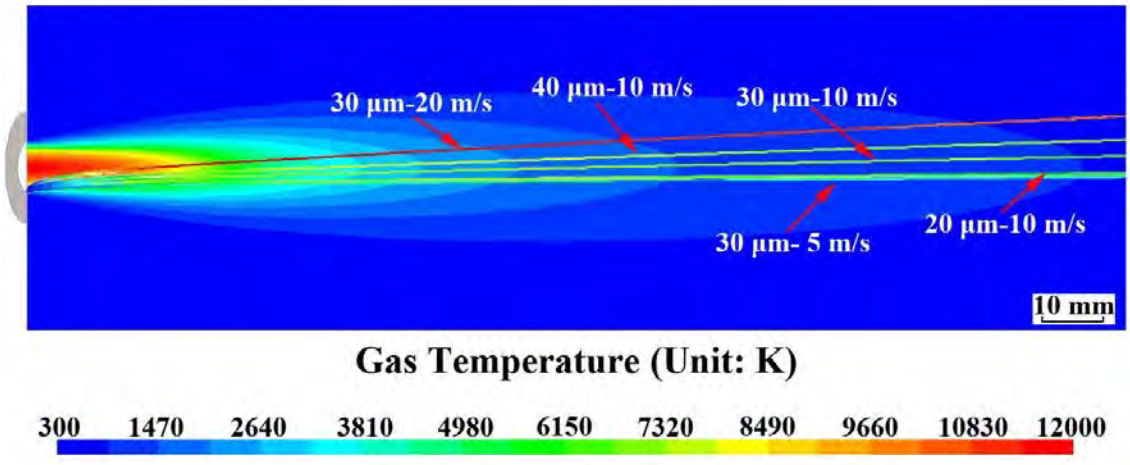


(b)

Figure 4-6. (a) Particle trajectories and (b) superimposed on the gas temperature distribution of the plasma jet calculated for an applied current of 500 A.

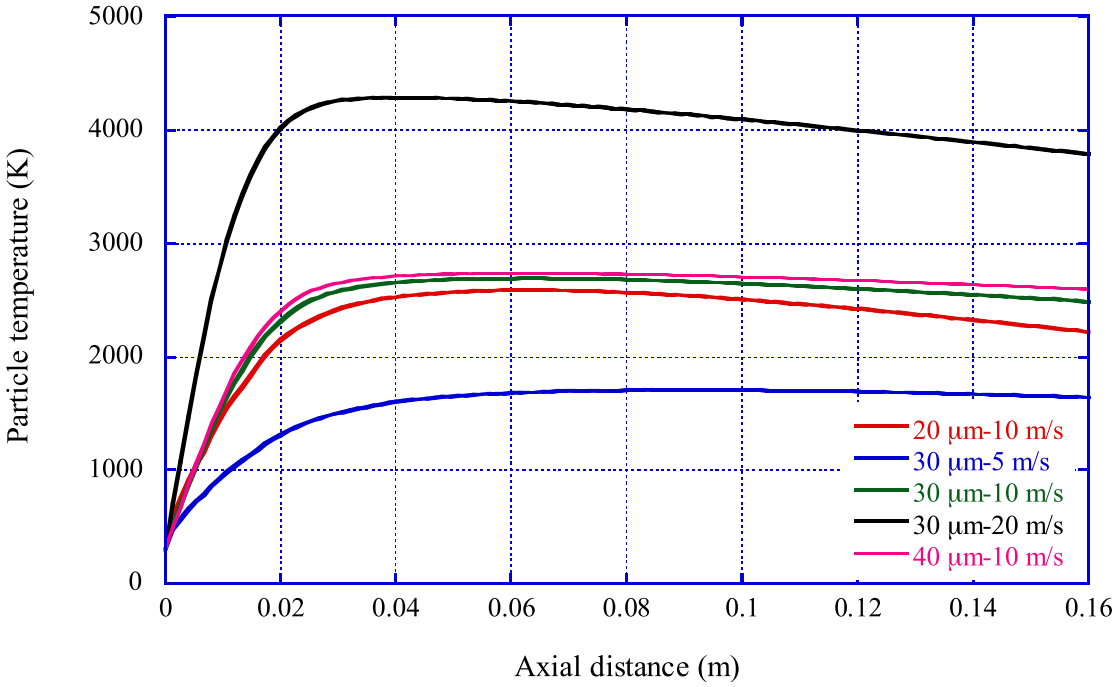


(a)

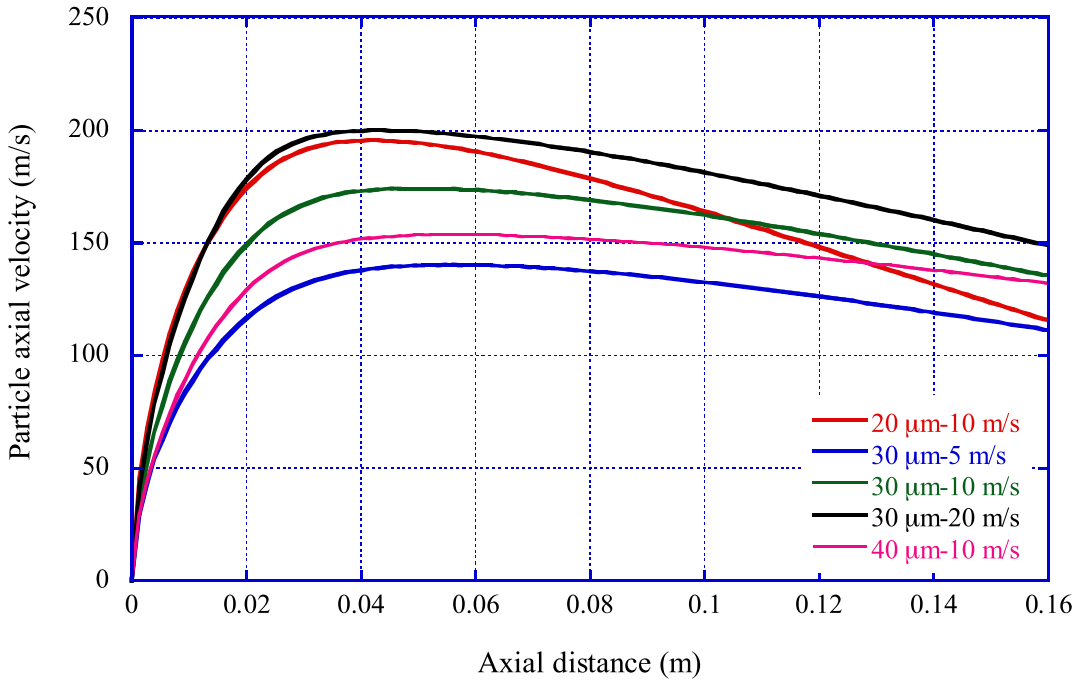


(b)

Figure 4-7. In-flight (a) particle temperature and (b) velocity calculated for an applied current of 500 A.

Figure 4-8 shows the particle temperature and velocity for particles with a diameter of 30 μm and an initial radial velocity of 10 m/s for different applied currents and a spray distance of 50 mm. It shows that both the particle temperature and velocity increase with increasing applied current due to increases in the gas temperature and velocity. Therefore, a high applied current is required to spray refractory materials such as high-melting-point metals and ceramics.

### 4.4.3 Comparison with experimental results

The particle temperature and velocity were measured by DPV-2000 and SprayWatch systems (see Chapter 2). Based on the flow rate of the powder-feeding gas and the diameter of the orifice from which the powder is injected, in the in-flight particle diagnostic experiments, the particles are estimated to have an initial radial velocity of 10 m/s. Therefore, the calculation results for an initial radial velocity of 10 m/s shown in figure 4-7(a) were compared with the experimental results. The main differences between the simulation and the experiment are the powder feeding position and the powder composition. In the experiment, the powder feeding position is located inside the plasma torch and 9 mm from the torch exit (see figure 2-2), whereas it is located at the torch exit in the simulations. In addition, the powder used in the experiment is 85% alumina and 15% titania rather than pure alumina. Figure 4-9 compares the calculated particle temperature with the measured one for an applied current of 500 A. It shows that the calculated particle temperature agrees well with the experimental one. Figure 4-10 compares the calculated particle velocity with the measured one for an applied current of 500 A. The measured particle velocity is slightly higher than the calculated one. This discrepancy may be caused by the different powder feeding positions. Because the particle is accelerated inside the plasma torch, the measured particle velocity is higher than the calculated one. There is another reason related to the discrepancy, the drag coefficient. The actual drag coefficient of solid particle at the initial phase is some higher than the one in the simulations because

the drag coefficient of spherical particle was adopted, whereas the particles are not spherical before their melt. The results imply that plasma jet simulations can effectively predict the steady-state particle temperature and velocity when the calculated results for a plasma torch are used as the boundary conditions for the gas inlet of the plasma jet.

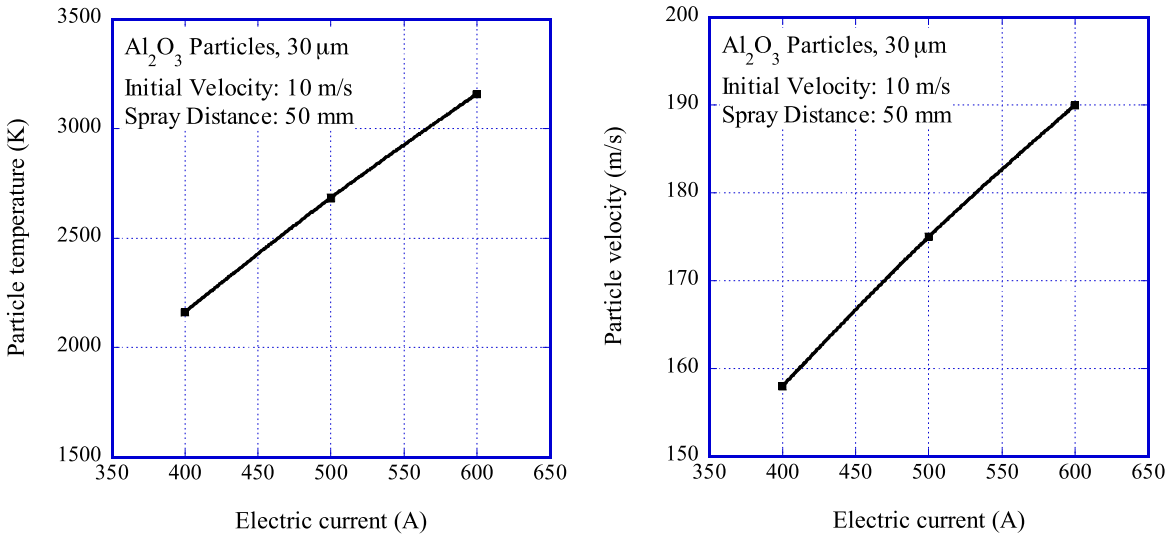


(a) (b)

Figure 4-8. Effect of applied current on in-flight (a) particle temperature and (b) velocity.

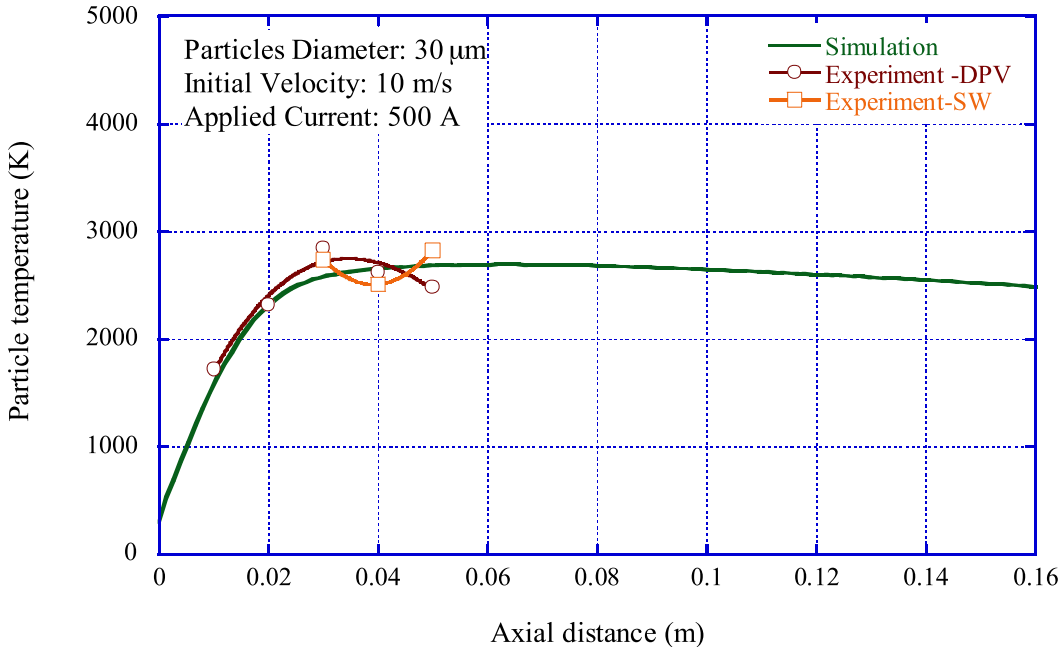


Figure 4-9. Comparison of calculated and experimentally measured particle temperatures.

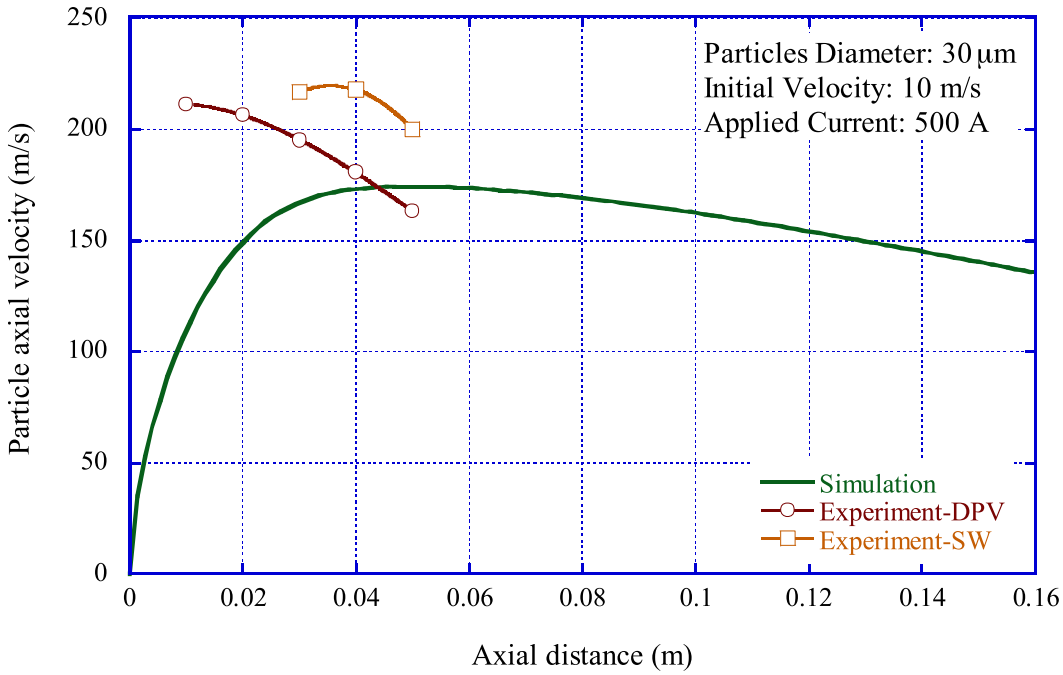


Figure 4-10. Comparison of calculated and experimentally measured particle velocities.

## References

[1]. Borisov Yu., Krivtsun I., Muzhichenko A., Computer Modelling of the Plasma Spraying Process, Thermal Spray 2003: Advancing the Science & Applying the Technology, (Ed.) C. Moreau and B. Marple, Published by ASM International, Materials Park, Ohio, USA, 2003.

[2]. Bolot R., Li J. and Coddet C., Modeling of thermal plasma jets: a comparison between PHOENICS and FLUENT, Thermal Spray 2004: Advancing in Technology and Application, ITSC, May 2004, Osaka, Japan.

[3]. Wang Fuchi, Fan Qunbo, Wang Lu and Wang Quansheng, Numerical simulation of a multi-component reacting plasma jet in plasma spraying, Thermal Spray 2004: Advancing in Technology and Application, ITSC, May 2004, Osaka, Japan.

[4]. Ramachandran Kandasamy and Nishiyama Hideya, Fully coupled 3D modeling of plasma–particle interactions in a plasma jet, Thin Solid Films, 457 (2004), 158–167.

[5]. Kang C. W., Ng H. W., Yu S. C. M., Comparative Study of Plasma Spray Flow Fields and Particle Behavior Near to Flat Inclined Substrates, Plasma Chem Plasma Process (2006) 26:149–175.

[6]. Xiong Hong-bing, Zhu Ze-fei and Lin Jiang-zhong, Three-dimensional simulation of air entrainment in plasma jet and particle oxidation, Journal of Zhejiang University (Engineering Science), Vol. 40 No. 4, Apr. 2006.

[7]. Li He-Ping, Chen Xi, Three-dimensional simulation of a plasma jet with transverse particle and carrier gas injection, Thin Solid Films, 390 (2001), 175-180.

[8]. Li He-Ping and Pfender E., Three Dimensional Modeling of the Plasma Spray Process, Journal of Thermal Spray Technology, Volume 16(2) June 2007, 245–260.

[9]. Morsi S.A. and Alexander A.J., An investigation of particle trajectories in two-phase flow systems, Journal of Fluid Mechanics 55 (1972) 193–208.

[10]. Ranz W.E. and Marshall W.R., Evaporation from drops, Part I, Chemical

Engineering Progress 48 (1952).

[11]. Ansys Inc., Fluent 6.3 User's Guider, NH, 2006.

# Chapter 5
# Summary and Recommendations for Future Work

## 5.1 Introduction

In this thesis, three LTE models have been developed to model heat transfer and flow patterns inside a non-transferred DC plasma torch. The arc voltage and anode erosion have been measured to verify the numerical calculation results. The arc fluctuation inside the torch, arc voltage, electrical current density, thermal energy of the plasma arc, gas temperature, and velocity were analyzed numerically. After analyzing the characteristics of the three LTE models, the heat transfer and flow patterns of the plasma jet outside the plasma torch were calculated by employing the most accurate results of the three models as the boundary conditions in plasma jet simulations. Based on the gas flow field of the plasma jet, the injected particle behavior in the plasma jet was calculated and compared with experimentally measured results.

## 5.2 Summary of Results

The results of this thesis are summarized below.

In chapter 2, some parameters of a plasma torch and plasma jet were measured experimentally to provide a reference for the numerical results. The arc voltage and current of a SG-100 torch were measured using a two-channel digital storage oscilloscope. The results revealed that the electric current fluctuates with a frequency of 300 Hz due to the rectification of the power supply. In addition, the arc voltage fluctuates with a small amplitude relative to the base value of the arc voltage. The average arc voltage ranges from 20 to 30 V for applied currents in the range 300 to 800 A. The electrothermal efficiency of

the plasma torch was found to be about 50% via the measurements of the thermal energy removed by cooling water. The anode erosion was observed to determine the arc attachment location on the internal surface of the anode. The anode appears always to be eroded close to the corner on the internal surface of the anode. Extended usage only extends the eroded region. The fluctuation of the plasma jet and the injected particle behavior were measured experimentally. Observations of the plasma jet revealed that the length and deviation direction of the plasma jet vary with time and that the plasma jet always fluctuate. The measured in-flight particle temperature increased as the stand-off distance increased up to the 30 mm and it subsequently decreased. The measured in-flight particle velocity decreased with increasing stand-off distance.

Chapter 3 described modeling of the arc behavior inside the plasma torch. Three LTE models were developed to model heat transfer and flow patterns inside a non-transferred DC plasma torch. Based on the LTE assumption, the electron temperature was equal to the heavy particle temperature, which is low near the electrodes, especially near the anode surface. Hence, the equilibrium electrical conductivity is extremely low (less than $10^{-2}$ S/m), which limits the electrical current that flows though the electrodes. Three methods were employed in this study to overcome this restriction on the electrical current that flows through the electrodes. Two conventional LTE models were used to model the plasma arc behavior inside a plasma torch. In model 1, the simplest conventional LTE model, the electrical conductivity was essentially determined by the gas temperature. Based on the reduced electric conductivity near the cold interface of the electrode, a high electrical conductivity of $10^4$ S/m was artificially set near the anode (within 0.1 mm), so that a new arc attachment will form if the arc is sufficiently close to the internal surface of the anode. In model 2, an improved conventional LTE model, the electrical conductivity was also essentially determined by the gas temperature and an artificial electrical current route was set by using a criterion based on a preset breakdown electric field. If the local electric field exceeds this breakdown electric field, a high electric conductivity channel forms that

passes through the maximum electric field region perpendicular to the anode surface. The electric current will then pass through the channel and a new attachment will form. In model 3, the novel LTE model developed in the current study, a nominal electron temperature was proposed that was derived from the plasma gas temperature and modified by the electrical field strength, to correct the underestimation of the electrical conductivity of the plasma gas due to the LTE assumption. No additional assumptions were required to ensure the formation of an electrical current path between the cathode and the anode if the electrical conductivity of the plasma gas is determined by the nominal electron temperature rather than the gas temperature.

Using these three LTE models, the gas temperature and velocity inside the plasma were calculated and the electrical current density, potential, and field were also estimated. Almost all the calculation results revealed that the arc inside the plasma torch fluctuated for all three models, although the fluctuations were especially large for the two conventional LTE models. While the novel LTE model (model 3) can partially reproduce the arc fluctuations inside the plasma torch, it cannot model the fluctuations in the radial direction because the arc parameters have axisymmetrical distributions. The gas temperature and velocity inside the plasma torch increased with increasing applied current for all three models. Although the distributions of gas temperature and velocity inside the plasma torch calculated by the three models differed somewhat, similar temperatures and velocities were obtained. Model 1 gave the highest arc voltage that was much higher than the measured value; this is due to the LTE assumption and the underestimation of the gaseous electrical conductivity. The arc voltage obtained with model 2 is closer to the measured one, although it is still higher than the measured value for the same reasons as model 1. The arc voltage calculated by model 3 agrees much better with the experimental results than those calculated by the two conventional LTE models; this is because it employs the nominal electron temperature. As the arc voltage determines the input electrical energy to the arc plasma, model l gives the highest gas temperature and velocity

at the torch exit, and the gas temperature and velocity obtained using model 2 are higher than those calculated by model 3 for the same spray conditions. The thermal energy of the plasma arc calculated by the three models exhibits the same tendency as the arc voltage. The thermal energies of the plasma arc calculated by models 1 and 2 are much higher than the measured value because they overestimate the arc voltage. In contrast, the thermal energy of the plasma arc calculated by model 3 agrees well with the experimental value. Even though the electrothermal efficiency of the plasma torch calculated by model 3 is much closer to the experimental one than those calculated by the two conventional LTE models, it differs slightly from the measured value due to the effect of the sheath voltage drop, which was not considered in the present study. Comparison of the anode erosion position with the electrical current density distributions inside the plasma torch reveals that model 3 can effectively predict the location of anode erosion. Even though the two conventional LTE models effectively model arc fluctuations inside the plasma torch, the newly developed LTE model generally calculates the arc parameters inside the plasma torch more accurately than those of the other two conventional LTE models. However, the newly developed LTE model cannot model arc fluctuations in the radial direction inside the plasma torch.

Chapter 4 gives an example of modeling the behavior of a plasma jet outside a plasma torch. In addition, the in-flight particle temperature and velocity in a plasma jet were predicted using a 3D steady-state model based on the arc behavior presented in Chapter 3. Based on the accuracy of the plasma arc parameters calculated in the steady state in Chapter 3, the flow conditions at the torch exit for the newly developed model were selected as the boundary conditions for plasma jet simulations. Gas flow fields for the plasma jets outside the plasma torch in the steady state were obtained using the flow conditions at the plasma torch exit calculated using model 3. The particle trajectory, temperature, and velocity were determined from the gas temperature and velocity fields of plasma jets. The numerical calculation results revealed that the gas temperature and

velocity increase with increasing applied current due to the increase in the input electrical energy. The in-flight particle trajectory was influenced by the initial particle velocity and diameter. Different trajectories cause particles to experience different heating rates and accelerations. The calculated in-flight particle temperature and velocity generally increased as the standoff distance increased to about 30 mm and they subsequently decreased. Similar to the gas temperature and velocity, the in-flight particle temperature and velocity also increased with increasing applied current. The in-flight particle temperature and velocity obtained using the results of the newly developed LTE model as the boundary conditions are very similar to the measured ones. This demonstrates that the improved accuracy of the newly developed LTE model for modeling plasma arcs inside plasma torches.

## 5.3 Recommendations for Future Work

In this thesis, the results obtained using the newly developed LTE model (model 3) agree well with the experimental ones, especially the anode attachment position, the thermal energy of the plasma arc, and the in-flight particle conditions. However, the calculated arc voltage differs slightly from the measured one; this gives rise to some discrepancy between with the calculated and experimental electrothermal efficiencies of the plasma torch. These discrepancies are caused by the sheath voltage drop, which was not considered in the present study. Therefore, to make the calculated voltage closer to the actual one, a suitable model should be developed that considers the sheath voltage drop [1–6]. Another reason about the discrepancy of the arc voltage is the effects of the electrodes evaporation that was not considered in the current study. The evaporation effect of the electrodes should be considered in the future work.

To reduce the computational cost, the plasma torch and jet were calculated separately in the current study. If necessary, these two components can be combined in a single domain so that the plasma torch and jet can be simultaneously calculated to reduce the

calculation error and to model fluctuations of plasma jets outside plasma torches more accurately.

In the plasma torch calculations, the applied current was kept constant. However, the actual current fluctuates with a frequency of 300 Hz. Consequently, the calculated arc voltage differed slightly from the measured one. In future studies, a varying electric current could be used to model heat transfer and flow patterns inside non-transferred DC plasma torches.

## References

[1]. Zhou X. and J. Heberlein, Analysis of the arc-cathode interaction of free-burning arcs, Plasma Source Sci. Technol. 3 (1994), p564-574.

[2]. Benilov M. S., Understanding and modelling plasma-electrode interaction in high-pressure arc discharges: a review, J. Phys. D: Appl. Phys. 41 (2008), p1-30.

[3]. Benilov M. S. and A Marotta, A model of the cathode region of atmospheric pressure arcs, J. Phys. D: Appl. Phys. 28 (1995), p1869-1882.

[4]. Zine B., D.Saifaoui, A.Dezairi, T.Es-sabbar, A.Boumhali, M.ElMouden1, Modelling of Collision in the Plasma Sheath and the Cathode Erosion of Electrical Arc, M. J. Condensed Matter, Volume 6, Number 1, p 26-34, 2005.

[5]. Sheridan T. E. and J. Goree, Collisional plasma sheath model, Phys. Fluids B, 3(10), p 2796-2804, 1991.

[6]. Li He-Ping and M S Benilov, Effect of a near-cathode sheath on heat transfer in high-pressure arc plasmas, J. Phys. D: Appl. Phys., 40, p 2010–2017, 2007.

# Appendix
# UDM, UDS and UDF of FLUENT

## A.1 Introduction

FLUENT is a state-of-the-art computer program for modeling fluid flow and heat transfer in complex geometries. The FLUENT solver has the basic capabilities to solve the equations that govern continuity, momentum, and energy. The default parameters in the FLUENT solver include the gas pressure (density), velocity vector, temperature, and other turbulence parameters. In the present study, some additional parameters (e.g., the electric potential, the magnetic vector potential, the electric field, the magnetic induction vector, and the electric current density vector) must be solved to model fluid flow, heat transfer, and the electromagnetic behavior of the plasma gas. FLUENT has an add-on interface that can be used with user-written programs; this enables other transport equations to be subsequently solved sequentially.

In this thesis, user-defined memory (UDM), user-defined scalar (UDS), and user-defined functions (UDFs) were employed in Eqs. 3-8 to 3-15 to solve the electromagnetic flow in the DC plasma spray torch.

## A.2 UDM, UDS, and UDF

The UDM (User-Defined Memory) is the memory previously allocated to store additional variables (e.g., the electric current density in the present study). These additional variables stored in the UDMs are very convenient to use like the default variables in FLUENT solver, such as the gas pressure. The FLUENT solver uses these variables to solve the parameters of the plasma gas flow including the additional parameters, such as

the electrical potential.

The UDS (User-Defined Scalar) provides a solver to arbitrarily solve additional transport equations such as electromagnetic equations, like the solutions of the default equations for mass, momentum, and energy conservation. Additional scalar transport equations may be required such as for solving certain combustion applications or modeling plasma-enhanced surface reactions. FLUENT allows additional scalar transport equations to be defined in the UDS panel for your models; for example, it can be used to solve the Maxwell equations for a plasma gas.

UDFs (User-Defined Functions) are functions that can be programed by the user. They can be dynamically loaded with the FLUENT solver to enhance the standard features of the code. For example, a UDF can be used to define boundary conditions, material properties, and source terms for a specific flow regime, as well as specify customized model parameters, initialize a solution, or enhance post-processing.

## A.3 Details for Solving an Arc Plasma in a Plasma Torch

Figure A-1 shows the FLUENT solver procedure used to model a plasma arc in a plasma spray torch in the current research. The steps given in red contain some UDFs. Nine UDMs were allocated to store the variables of the electromagnetic parameters. Table A-1 gives the UDM parameters. At the same time, four UDSs were defined to solve some electromagnetic equations; their parameters are listed in Table A-2.

First, in the initiation step, a UDF was employed to initialize the UDMs. The key codes of this function are given below:

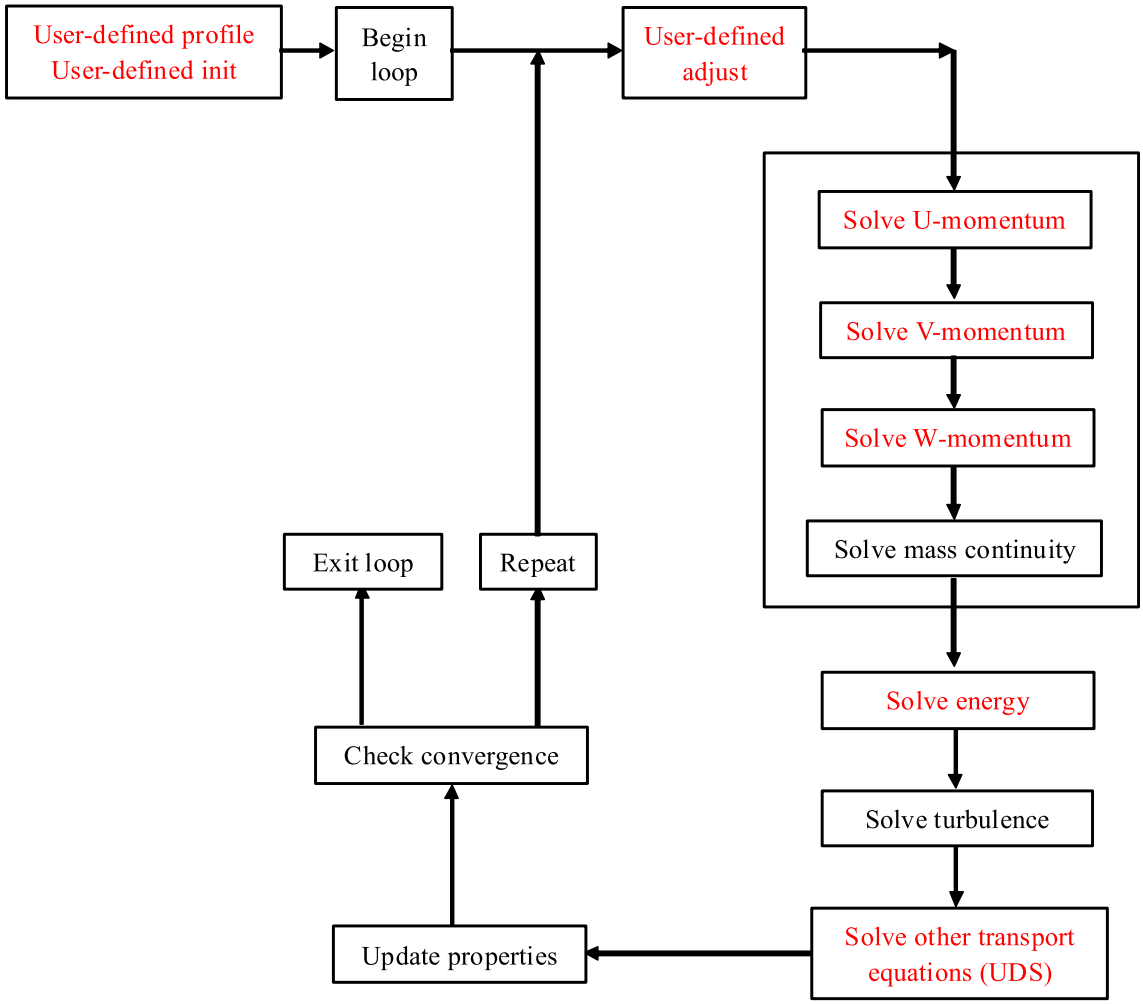


Figure A-1. Procedure for determining the solution in the current solver

```
DEFINE_INIT(init_UDMI,d)
{
    ......
    C_UDMI(c, t, 0)=0.0; //initialize E_x
    ......
    C_UDMI(c, t, 8)=0.0; //initialize B_z
    ......
}
```

Second, two simple electromagnetic equations and Ohm's law were calculated using

the user-defined adjust function. The key codes of this function are:

```
DEFINE_ADJUST(dynamic_contect, d)
{
    ......
    //E⃗ = −∇∅
    C_UDMI(c,t,0) = 0.0- C_UDSI_G(c,t,0)[0];
    C_UDMI(c,t,1) = 0.0- C_UDSI_G(c,t,0)[1];
    C_UDMI(c,t,2) = 0.0- C_UDSI_G(c,t,0)[2];
    ......
    //B⃗ = ∇×A⃗
    C_UDMI(c,t,6)=C_UDSI_G(c,t,3)[1]-C_UDSI_G(c,t,2)[2];
    C_UDMI(c,t,7)=C_UDSI_G(c,t,1)[2]-C_UDSI_G(c,t,3)[0];
    C_UDMI(c,t,8)=C_UDSI_G(c,t,2)[0]-C_UDSI_G(c,t,1)[1];
    ......
    //j⃗ = σE⃗
    C_UDMI(c,t,3) = C_UDSI_DIFF(c,t,0)*C_UDMI(c,t,0);
    C_UDMI(c,t,4) = C_UDSI_DIFF(c,t,0)*C_UDMI(c,t,1);
    C_UDMI(c,t,5) = C_UDSI_DIFF(c,t,0)*C_UDMI(c,t,2);
    ......
}
```

In the step that solves the momentum conservation equations, the source term of $\vec{j}\times\vec{B}$ must be considered compared to the default momentum conservation equations. Therefore, UDFs were employed to define additional source terms of the momentum conservation equations. The key codes of the functions are:

```
DEFINE_SOURCE(Xmom_source,c,t,dS,eqn)
{
```

```
    ......
    Return ND_CROSS_X(jx,jy,jz,Bx, By, Bz);//( j⃗×B⃗)x
}
DEFINE_SOURCE(Ymom_source,c,t,dS,eqn)
{
    ......
    Return ND_CROSS_Y(jx,jy,jz,Bx, By, Bz);// ( j⃗×B⃗)y
}
DEFINE_SOURCE(Zmom_source,c,t,dS,eqn)
{
    ......
    Return ND_CROSS_Z(jx,jy,jz,Bx, By, Bz);// ( j⃗×B⃗)z
}
```

Table A-1. The definition of UDMs

| No. | Description | UDM |
|---|---|---|
| 1 | x-Electric field ($E_x$) | C_UDMI(c, t, 0) |
| 2 | y-Electric field ($E_y$) | C_UDMI(c, t, 1) |
| 3 | z-Electric field ($E_z$) | C_UDMI(c, t, 2) |
| 4 | x-Electric current density ($j_x$) | C_UDMI(c, t, 3) |
| 5 | y-Electric current density ($j_y$) | C_UDMI(c, t, 4) |
| 6 | z-Electric current density ($j_z$) | C_UDMI(c, t, 5) |
| 7 | x-Magnetic induction ($B_x$) | C_UDMI(c, t, 6) |
| 8 | y-Magnetic induction ($B_y$) | C_UDMI(c, t, 7) |
| 9 | z-Magnetic induction ($B_z$) | C_UDMI(c, t, 8) |

Table A-2. The definition of UDSs

| No. | Description | UDS |
|---|---|---|
| 1 | Electric potential ($\Phi$) | Scalar-0 |
| 2 | x-Magnetic vector potential ($A_x$) | Scalar-1 |
| 3 | y-Magnetic vector potential ($A_y$) | Scalar-2 |
| 4 | z-Magnetic vector potential ($A_z$) | Scalar-3 |

In the step that solves the energy conservation equations, the source terms of $\vec{j}.\vec{E}$ and $S_r$ must be considered relative to the default energy conservation equations.. Therefore, UDFs were employed to define additional source terms in the energy conservation equations. The key codes of the function are:

```
DEFINE_SOURCE(energy_source,c,t,dS,eqn)
{
    ......
    Return C_UDMI(c,t,3)*C_UDMI(c,t,0)+C_UDMI(c,t,4)*C_UDMI(c,t,1)+
            C_UDMI(c,t,5)*C_UDMI(c,t,2)-Radition(T);// j.E-Sr
}
```

The two remaining Maxwell equations (Eqs. 3-11 and 3-13) were solved using the defined UDSs given by the UDFs.

For the equation of $\nabla \cdot (-\sigma \nabla \emptyset) = 0$, only the diffusion coefficient needs to be defined for Scalar-0. Based on this equation, the diffusion coefficient represents the electric conductivity. Once the diffusion coefficient had been defined in the FLUENT solver, the equation could be discretized and the electric potential could be solved.

For the equation $\Delta \vec{A} = -\mu_0 \vec{j}$, only the source terms need to be defined for Scalar-1 to 3. Based on this equation, the source terms should be defined as $\mu_0 \vec{j}$. The UDFs used to define the source terms are similar to the above-mentioned codes. Once the source terms

had been defined in the FLUENT solver, the equations could be discretized and the magnetic vector potential could be obtained.

Using the UDMs, UDSs, and UDFs of FLUENT, Eqs. 3-8 to 3-15 were solved, enabling the electromagnetic gas flow in the plasma torch to be obtained by commercial CFD software.

# Published Papers

[1] **R. Huang**, H. Fukanuma, Y. Uesugi, Y. Tanaka; An Improved Local Thermal Equilibrium Model of DC Arc Plasma Torch; IEEE Transactions on Plasma Science; Volume: 39, Issue: 10, p 1974 – 1982 (2011. 10).

[2] **R. Huang,** H. Fukanuma, Y. Uesugi, Y. Tanaka; Simulation of Arc Root Fluctuation in a DC Non-transferred Plasma Torch with Three Dimensional Modeling; Journal of Thermal Spray Technology, Vol. 21, Issue. 3-4 (2012).

[3] **R. Huang**, H. Fukanuma, Y. Uesugi, Y. Tanaka; Simulation of Arc Root Fluctuation in a DC Non-transferred Plasma Torch with Three Dimensional Modeling; International Thermal Spray Conference and Exposition (ITSC 2011); September 27 – 29, 2011; CCH - Congress Center Hamburg/Germany; p1256-1261, on CD-ROM (2011).

[4] H. Fukanuma, **R. Huang**, Y. Tanaka, and Y. Uesugi; Mathematical Modeling and Numerical Simulation of Splat Cooling in Plasma Spray Coatings; Journal of Thermal Spray Technology, vol. 18, issue 5-6, p965-974 (2009).

[5] **R. Huang**, H. Fukanuma; Study of the Influence of Particle Velocity on Adhesive Strength of Cold Spray Deposits; Journal of Thermal Spray Technology, Vol. 21, Issue. 3-4 (2012).

[6] **R. Huang**, H. Fukanuma; Study of the Influence of Particle Velocity on Adhesive Strength of Cold Spray Deposits; International Thermal Spray Conference and Exposition (ITSC 2011); September 27 – 29, 2011; CCH - Congress Center Hamburg/Germany; p1085-1090, on CD-ROM (2011).

[7] **R.Z. Huang**, H. Fukanuma; The Influence of Spray Conditions on Deposition Characteristics of Aluminum Coatings in Cold Spraying; International Thermal Spray Conference and Exposition 2009: Expanding Thermal Spray Performance to New Markets and Applications (ASM International); 4-7 May 2009, Las Vegas, U.S.A.; p279-284 (2009).

[8] **R.Z. Huang**, B. Sun, N. Ohno, H. Fukanuma; Study on the Influences of DPV-2000 Software Parameters on the Measured Results in Cold Spray; International Thermal Spray Conference and Exposition 2006: Science, Innovation, and Application (ASM International); 15-18 May, 2006; Seattle, WA, U.S.A.; ASM-Int.; p999-1004 (2006).

[9] **Renzhong Huang**, Bo Sun, Naoyuki Ohno, Hirotaka Fukanuma; Study on the Influences of DPV-2000 Software Parameters on the Measured Results in Cold Spray; 1st Asian Thermal Spray Conference (ATSC-2005), 2005-11 (Nagoya), p107-108.

[10] **Huang Renzhong**, Wang Yuyue, Yang Guanjun, Li Changjiu, Li Qilian; Effect of Pressure During Hot-pressing on Microstructure and Mechanical Properties of B/ Al Composite (in

Chinese); Aerospace Materials & Technology; Vol. 3, 2004, p51-55.

[11] H. Fuknuma, N. Ohno, B. Son, **R. Huang**; The Influence of particle Morphology on In-Fright Particle Velocity in Cold Spray; International Thermal Spray Conference and Exposition 2006: Science, Innovation, and Application (ASM International); 15-18 May, 2006; Seattle, WA, U.S.A.; p97-101 (2006).

[12] Hirotaka Fukanuma, Naoyuki Ohno, Bo Sun, **Renzhong Huang**; In-flight particle velocity measurements with DPV-2000 in cold spray; Surface and Coatings Technology; Volume: 201, Issue: 5, p1935-1941 (2006).

[13] H. Fukanuma, **R. Huang**; The Development of High Temperature Gas Heater in the Cold Spray Coating System; International Thermal Spray Conference and Exposition 2009: Expanding Thermal Spray Performance to New Markets and Applications (ASM International); 4-7 May 2009, Las Vegas, U.S.A.; p267-272 (2009).

[14] K.H. Kim, S. Kuroda, M. Watanabe, **R. Huang**, H. Fukanuma, H. Katanoda; Comparison of oxidation and microstructures of warm-sprayed and cold-sprayed titanium coatings; Journal of Thermal Spray Technology, Vol. 21, Issue. 3-4 (2012).